

Copyright
by
Masayuki Wada
2013

The Dissertation Committee for Masayuki Wada
certifies that this is the approved version of the following dissertation:

Resonance Particles in Heavy-Ion Collisions

Committee:

Christina Markert, Supervisor

Gerald Hoffmann

Karol Lang

Sacha Kopp

Milos Milosavljevic

Resonance Particles in Heavy-Ion Collisions

by

Masayuki Wada, B.S.

DISSERTATION

Presented to the Faculty of the Graduate School of

The University of Texas at Austin

in Partial Fulfillment

of the Requirements

for the Degree of

DOCTOR OF PHILOSOPHY

The University of Texas at Austin

May 2013

Dedicated to my wife Maki and daughter Fuka.

Acknowledgments

This research would not have been possible without the support of many people. First and foremost, I would like to thank my advisor Christina Markert for giving me an engaging research opportunity, and for providing great guidance and support throughout my Ph.D. study. I consider it an honor to work with the past and present members of the Relativistic Heavy Ion Physics group at the University of Texas at Austin, who gave me many cheerful encouragements and discussions: Professor Gerald Hoffmann, Lanny Ray, Joachim Schambach, Dylan Thein, Kohei Kajimoto, Andrew Oldag, Liang Li, Alan Davila, Elizabeth W. Oldag, Prabhat Bhattarai, Martin Cordrington, and Alexander Jentsch. I would also like to thank my committee members: Karol Lang, Sacha Kopp, Milos Milosavljevic, Gerald Hoffmann, and Christina Markert. I am indebted to my colleagues who advised and supported me in the TOF and Light Flavor Physics Working group in the STAR collaboration: Geary Eppley, William J. Llope, Frank Geurts, Xin Dong, Lijuan Ruan, Zhangbu Xu, Zebo Tang, Bingchu Huang, Kefeng Xin, Joey Buwerworth, Xi-angli Cui, Lokesh Kumar, Xiaoping Zhang, Patrick Huck and many other friends. Special thanks also to Elizabeth, Alex, and Martin for careful corrections of this dissertation. Finally, I wish to express my love and gratitude to my family Maki and Fuka for their understanding and support throughout my academic career.

Resonance Particles in Heavy-Ion Collisions

Masayuki Wada, Ph.D.

The University of Texas at Austin, 2013

Supervisor: Christina Markert

Heavy ions are collided at the Relativistic Heavy Ion Collider (RHIC) at Brookhaven National Laboratory (BNL) in an effort to create a unique state of nuclear matter, where quarks and gluons can freely move over volumes larger than the typical size of a nucleon (typical scale of Quantum Chromodynamics, QCD). In this state, called a *Quark Gluon Plasma* (QGP), it is proposed Chiral symmetry is restored. The fact that Chiral symmetry is a symmetry of the Standard model and is broken at low energy (current energy scale of universe) makes the study of its possible very interesting.

The analysis in this dissertation searches for signatures of chiral symmetry restoration at the phase transition between the QGP and the hadronic gas phase by using resonance particles as probes. Resonances may decay inside of hot dense matter due to their short lifetimes, and therefore their decay daughters carry away dynamical information such as the mass and decay width. Mass shift and width broadening are predicted signatures of chiral symmetry restoration. The $\phi(1020)$ resonances reconstructed from the dielectron decay

channel are investigated in this dissertation. This decay channel does not suffer scattering from the late hadronic medium due to the relatively small interaction cross section of leptons with hadrons. The disadvantage of this channel comes from the small branching ratio. Therefore, large statistics and clean Particle IDentification (PID) are necessary for this analysis. Those requirements were fulfilled with high luminosity beams at RHIC and the newly developed and installed Time Of Flight (TOF) detectors, which provide clear particle identification up to momentum of 2-3 GeV/ c , as well as the large acceptance of the Solenoidal Tracker At RHIC (STAR) detector.

In this dissertation, measurements of mass, width, transverse momentum spectrum, and yields of $\phi \rightarrow e^+e^-$ at mid-rapidity ($|y| < 1$) from the STAR experiment in Au+Au collisions at $\sqrt{s_{NN}} = 200$ GeV are presented and compared to a previously measured ϕ meson result from a hadronic decay channel. The possibility of medium modification which implies Chiral symmetry restoration is discussed.

Table of Contents

Acknowledgments	v
Abstract	vi
List of Tables	xii
List of Figures	xiii
Chapter 1. Introduction	1
1.1 QCD and Chiral Symmetry	3
1.1.1 Asymptotic Freedom	3
1.1.2 Chiral Symmetry	4
1.1.3 Explicit Breaking of Chiral Symmetry	6
1.1.4 Spontaneous Breaking of Chiral Symmetry (Hidden sym- metry)	8
1.1.5 Restoration of Chiral Symmetry	12
1.2 Hadronic Resonances	13
1.2.1 Breit-Wigner Formula	13
1.2.2 Mass, Width, and Medium Effects	14
1.2.3 Hadronic Resonances in Heavy Ion Collisions	15
1.2.4 Decay Channels	16
1.3 Outline	17
Chapter 2. Experimental Set Up	19
2.1 Introduction	19
2.2 Relativistic Heavy Ion Collider (RHIC)	19
2.3 STAR Experiment	23
2.3.1 Overview	23
2.3.2 Time Projection Chamber (TPC)	24

2.3.3	Time Of Flight System (TOF)	30
2.3.4	Trigger and Data Acquisition (DAQ)	40
Chapter 3.	Particle Identification	43
3.1	Introduction	43
3.1.1	PID by difference of interaction with detectors	43
3.1.2	PID by determining mass	45
3.2	Choice of PID Methods	48
3.2.1	Separation Power	49
3.2.2	Separation Method	50
3.2.2.1	$n\sigma$ Method	51
3.2.2.2	Probability Method	52
3.3	Choice of Distributions	53
3.3.1	PID with dE/dx	53
3.3.2	PID with TOF	55
3.3.2.1	Statistic (form of observable)	56
3.3.2.2	Fit Function (Distribution)	61
3.4	Combined PID	64
3.5	Obtain Distributions by Fit	65
3.5.1	Constraint with pure samples	65
3.5.2	Constraint by parameter behavior	66
3.6	Efficiency Correction	67
3.7	TOF Resolution	68
3.8	$n\sigma_{dE/dx}$ Resolution	70
Chapter 4.	$\phi \rightarrow e^+ + e^-$ Analysis	73
4.1	Data Set	73
4.1.1	Event Distributions	74
4.2	Event & Track Selection	76
4.2.1	Event Cut	76
4.2.2	Track Cut	78
4.2.3	Pair Cut	79
4.3	Electron Identification	80

4.3.1	Contaminations	82
4.3.2	Pure Electron Sample	83
4.3.3	Fit with All Relevant Particles	90
4.3.4	2D $n\sigma$ and Probability cuts	94
4.4	Signal Extraction (reconstruction)	96
4.4.1	Invariant Mass Reconstruction	96
4.4.2	Mixed-event Technique (background subtraction)	96
4.4.3	Signal Counting and Breit-Wigner Function Fit	97
4.4.4	dN/dy and Mean Transverse Momentum Estimation	100
4.5	Efficiency Correction	101
4.5.1	TOF Matching Efficiency	101
4.5.2	PID Cut Efficiency (acceptance)	102
4.5.3	TPC Acceptance & Track Quality Cut Efficiency	106
4.6	Systematic Error Estimation	107
Chapter 5.	Results	113
5.1	Signals	113
5.2	Mass and Width	117
5.3	Corrected $\phi(1520)$ Transverse Momentum Spectrum	120
5.4	Comparison to Hadronic Decay Channel	123
5.5	Model Comparison	124
Chapter 6.	Conclusion	128
Appendices		130
Appendix A.	Students' T Distribution	131
A.1	Physical meaning of Students' T Distribution	131
A.2	Integration of Students' T Distribution	132
A.2.1	Integration from 0 to a	133
Appendix B.	TOF Resolution	136
B.1	Relation Between L_T and p_T	136
B.2	Resolution of $\frac{\Delta\beta^{-1}}{\beta^{-1}}$	138

Appendix C. Spontaneous Symmetry Breaking	142
C.1 Spontaneous Symmetry Breaking	142
Bibliography	144
Vita	149

List of Tables

1.1	Hadronic resonances measured at STAR	17
3.1	Continuity of statistic	57
4.1	Event and track cuts	80
4.2	Track cuts for pure electron sample	86
4.3	Condition changes in systematic error study	109
4.4	Systematic errors averaged over p_T bins in percentage	110
5.1	$\phi \rightarrow e^+e^-$ corrected yield	123

List of Figures

1.1	Schematic picture of QCD phase diagram	2
1.2	Various measurements on the strong coupling constant, α_S , vs. energy scale, Q	4
1.3	Schematic picture of a quark anti-quark pair	10
1.4	Schematic picture of QCD dynamical mass generation	11
2.1	The Relativistic Heavy Ion Collider complex	20
	(a) The RHIC complex	20
	(b) Location of the experiments	20
2.2	RHIC integrated luminosity	22
	(a) RHIC integrated luminosity for heavy ion runs	22
	(b) RHIC integrated luminosity for proton runs	22
2.3	The STAR detector	24
2.4	Cutaway view of the TPC	25
2.5	The gating grid at the readout pads	27
2.6	The TOF system	31
2.7	Pictures of the upVPD	33

(a)	The upVPD assemblies	33
(b)	The installed upVPD	33
2.8	TOF tray construction	34
(a)	TOF tray with modules	34
(b)	Readout pads	34
2.9	Ionization in the MRPC	35
2.10	MRPC design	38
2.11	Recorded events at STAR	42
3.1	Particle penetration power in detectors	44
3.2	Muon stopping power	45
3.3	dE/dx vs. $\exp(\beta)$	47
3.4	2D separation power	50
(a)	Schematic diagram of separation power	50
(b)	Separation power in Kaon fit	50
3.5	dE/dx vs p	55
3.6	$1/\beta$ v.s. momentum	56
3.7	m^2 distributions (p+p 200 GeV Run8)	58
(a)	m^2 vs. p	58
(b)	m^2 distribution	58

3.8	$\Delta\beta^{-1}/\beta^{-1}$ distributions (p+p 200 GeV Run 8)	59
	(a) $\Delta\beta^{-1}/\beta^{-1}$ vs. p	59
	(b) $\Delta\beta^{-1}/\beta^{-1}$ distribution	59
3.9	$\Delta\beta^{-2}$ distributions (p+p 200 GeV Run9)	60
	(a) $\Delta\beta^{-2}$ vs. p^{-2}	60
	(b) $\Delta\beta^{-2}$ distribution	60
3.10	Gauss and Student's T distributions	62
3.11	Expected m^2 distribution at $1.0 > p > 1.5$ GeV/ c	63
	(a) Expected m^2 distribution	63
	(b) Fit with expected m^2 distribution	63
3.12	Electron identification in 2D at p=1-1.1 GeV/ c	64
	(a) 2D $n\sigma$ cut	64
	(b) 2D $n\sigma$ and probability cuts	64
3.13	Pion fit example	66
3.14	$\Delta\beta_p^{-1}/\beta^{-1}$ resolution vs. momentum	69
3.15	$\Delta\beta_p^{-1}/\beta^{-1}$ resolution for π , K, and p	70
3.16	$n\sigma_{dE/dx}$ resolution for all particles (Au+Au 200 GeV Run10)	71
	(a) $n\sigma_{dE/dx}$ resolution vs. p	71
	(b) $n\sigma_{dE/dx}$ resolution vs. $\gamma\beta$	71

4.1	Reference multiplicity and upVPD	75
	(a) Reference multiplicity distribution	75
	(b) Number of lit upVPDs	75
4.2	Primary vertex position on z axis	76
	(a) V_Z distribution	76
	(b) $V_{Z_{TPC}} - V_{Z_{upVPD}}$	76
4.3	Primary vertex position	77
	(a) V_X vs. V_Y before event cuts	77
	(b) V_X vs. V_Y after event cuts	77
	(c) V_X vs. V_Z distribution	77
	(d) V_Y vs. V_Z distribution	77
4.4	e^\pm opening angle from ϕ from simulation	79
4.5	Combined electron identification	81
4.6	Particle distributions around electrons	83
4.7	Schematic picture of a conversion pair	86
4.8	Reconstructed conversion points	86
	(a) In x-y plane	86
	(b) In y-z plane	86
4.9	QA histograms for the pure electron sample	87

(a)	Invariant mass of conversion pair candidates	87
(b)	$n\sigma_{dE/dx}^e$ distribution for primary tracks	87
4.10	2D fit of the pure electron sample at $p = 0.3 - 0.32$ [GeV/ c], $ \eta = 0.2 - 0.4$	89
4.11	Summary of the 2D fit parameters in the pure electron sample fit	90
4.12	2D fit example at $p = 0.48 - 0.5$ GeV/ c , $ \eta = 0 - 0.2$	92
4.13	Separation power between electrons and other particles	93
4.14	Distribution of real and MC data after the 2D $n\sigma$ and proba- bility cuts	94
4.15	e^+e^- invariant mass distribution at $p_T = 0.1 - 2.5$ GeV/ c	98
(a)	Invariant mass distribution of the e^+e^- pairs	98
(b)	p_T integrated $\phi \rightarrow e^+e^-$ signals	98
4.16	TOF matching efficiency	103
(a)	TOF matching efficiency vs p_T	103
(b)	$n\sigma_{dE/dx}^e$ vs. p of the pure electron sample	103
4.17	TOF matching efficiency in 2D	103
(a)	ϕ vs. p_T	103
(b)	η vs. p_T	103
4.18	PID efficiency and purity calculation	105
4.19	PID efficiency and contamination yields	106

(a)	PID efficiency and purity	106
(b)	Accepted yields and contamination yields	106
4.20	ϕ reconstruction efficiency	108
4.21	Systematical uncertainty on p_T spectrum	111
4.22	Systematical uncertainty of fit mass and width	112
(a)	Fit mass	112
(b)	Fit width	112
5.1	e^+e^- invariant mass distribution in Au+Au collisions at $\sqrt{s_{NN}} =$ 200 GeV/ c at $p_T = 0.1 - 2.5$ GeV/ c	114
(a)	Invariant mass distribution of the e^+e^- pairs	114
(b)	p_T integrated $\phi \rightarrow e^+e^-$ signals	114
5.2	e^+e^- invariant mass distributions and $\phi \rightarrow e^+e^-$ signals . . .	115
(a)	e^+e^- invariant mass distribution at $p_T = 0.1 - 0.4$ GeV/ c . . .	115
(b)	$\phi \rightarrow e^+e^-$ signal at $p_T = 0.1 - 0.4$ GeV/ c	115
(c)	e^+e^- invariant mass distribution at $p_T = 0.4 - 0.7$ GeV/ c . . .	115
(d)	$\phi \rightarrow e^+e^-$ signal at $p_T = 0.4 - 0.7$ GeV/ c	115
5.3	e^+e^- invariant mass distributions and $\phi \rightarrow e^+e^-$ signals . . .	116
(a)	e^+e^- invariant mass distribution at $p_T = 0.7 - 0.9$ GeV/ c . . .	116
(b)	$\phi \rightarrow e^+e^-$ signal at $p_T = 0.7 - 0.9$ GeV/ c	116

(c)	e^+e^- invariant mass distribution at $p_T = 0.9 - 1.2$ GeV/ c	116
(d)	$\phi \rightarrow e^+e^-$ signal at $p_T = 0.9 - 1.2$ GeV/ c	116
(e)	e^+e^- invariant mass distribution at $p_T = 1.2 - 1.6$ GeV/ c	116
(f)	$\phi \rightarrow e^+e^-$ signal at $p_T = 1.2 - 1.6$ GeV/ c	116
5.4	e^+e^- invariant mass distributions and $\phi \rightarrow e^+e^-$ signals . . .	117
(a)	e^+e^- invariant mass distribution at $p_T = 1.6 - 2.0$ GeV/ c	117
(b)	$\phi \rightarrow e^+e^-$ signal at $p_T = 1.6 - 2.0$ GeV/ c	117
(c)	e^+e^- invariant mass distribution at $p_T = 2.0 - 2.5$ GeV/ c	117
(d)	$\phi \rightarrow e^+e^-$ signal at $p_T = 2.0 - 2.5$ GeV/ c	117
5.5	Mass and Width from the p_T integrated signal at $p_T = 0.1 - 2.5$ GeV/ c	118
(a)	Invariant mass distribution comparison between the real data and simulation	118
(b)	Fit contour of the fit to the real data	118
5.6	Fit mass and width vs. p_T	121
(a)	Mass vs. p_T of $\phi(1020)$	121
(b)	Width vs. p_T of $\phi(1020)$	121
5.7	Corrected $\phi \rightarrow e^+e^-$ yields	122
5.8	Comparison to $\phi \rightarrow K^+K^-$ spectrum	124
5.9	Schematic picture of the model calculation	125

5.10	Components fit of the model calculation to the real $\phi \rightarrow e^+e^-$	
	data	126
	(a) Theoretical model fit to real ϕ signal with fixed ratio . .	126
	(b) Theoretical model fit to real ϕ signal	126
B.1	Relation between p_T and L_T	136
B.2	Relation between D_T and track length	140

Chapter 1

Introduction

Currently there is a considerable amount of evidence that the universe started as a fireball of extremely high temperature and high energy density, known as the *Big Bang*. In the first few micro seconds after the Big Bang, the temperature so high ($T > 100 \text{ GeV}$) that all of the particles were extremely relativistic[1]. Due to the asymptotic freedom [2][3] even strongly interacting particles such as quarks and gluons would have interacted weakly. Thus the early universe was a system of hot, weakly interacting color charged particles also known as a Quark Gluon Plasma (QGP).

Relativistic heavy ion collision experiments [4] were promoted in order to investigate such a phase by distributing high energy over a relatively large volume compared to smaller systems like $e + e$ and $p + p$ collisions. The QGP was expected to be a weakly coupled system, however, relativistic heavy ion collision experiments show evidences of a strongly coupled system [5]. The strongly coupled QGP is often called sQGP to be distinguished from the original QGP. A schematic picture of the QCD phase diagram is presented in Figure 1.1. As you can see from the figure, the relativistic heavy ion collisions provide us a unique environment to explore the QCD phase at high temperature and

low baryon chemical potential. There are two main possible phase transitions that a system created in relativistic heavy ion collisions might experience as it cools. They are *color confinement* and *chiral symmetry breaking*. Although color confinement, which is a phenomenon that color charged particles can not be found individually over the scale of strong interaction, is a popular and interesting topic, the focus of this dissertation is on chiral symmetry.

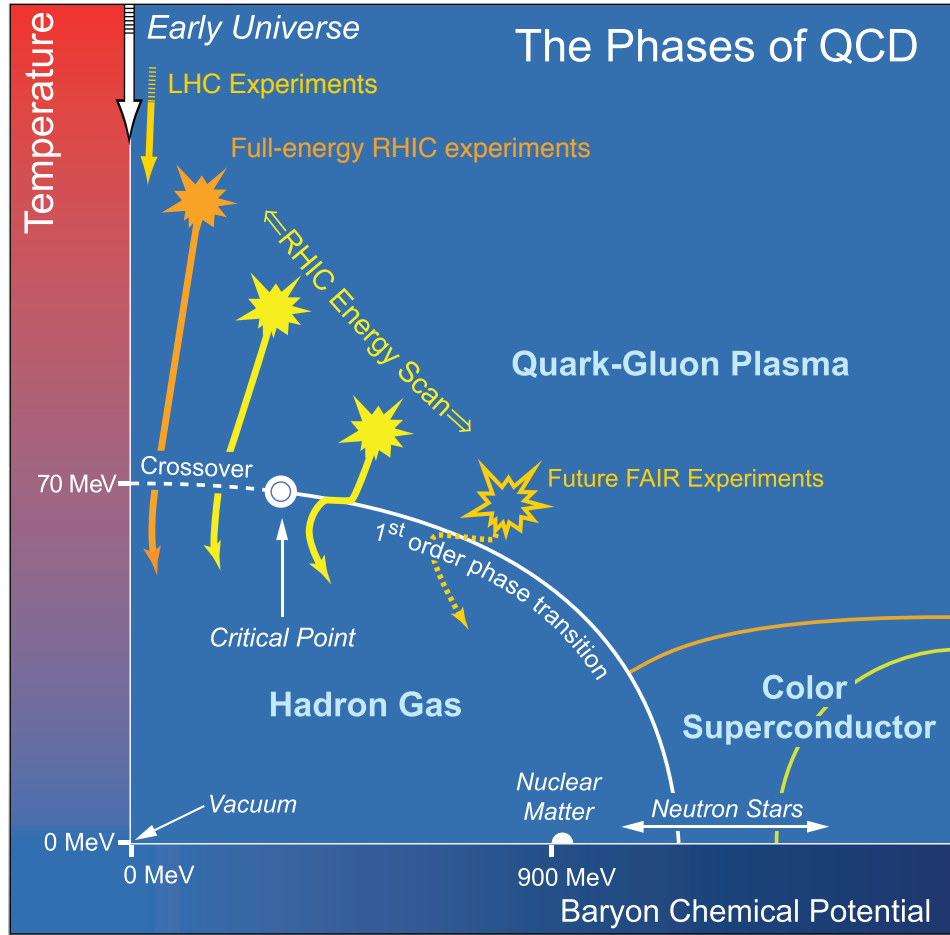


Figure 1.1: Schematic picture of QCD phase diagram [6]

1.1 QCD and Chiral Symmetry

In this section we follow discussion in articles [7] [8].

1.1.1 Asymptotic Freedom

In the SLAC-MIT e^-p deep inelastic scattering experiments, the resulting cross sections, which show Bjorken scaling [9], implied that the strong interaction has a phenomenon known as asymptotic freedom. A set of non-Abelian gauge theories that have the asymptotic freedom behavior were discovered in 1973 by David Gross and Frank Wilczek [2], and by David Politzer [3]. In the theories, asymptotic freedom appears as a consequence of running coupling constants (α_S for QCD), which depend on the renormalization scale (energy scale Q) as shown in Figure 1.2.

The accepted theory of the strong interaction is Quantum Chromodynamics (QCD), a non-Abelian gauge field theory with gauge group $SU(3)_{color}$ with gauge bosons (gluons) coupled to fermions (quarks), which constitutes one part of the $SU(3) \times SU(2) \times U(1)$ standard model. If quark masses are zero, QCD has a chiral symmetry (see Section 1.1.2). In reality, quarks have small masses (smallest for u and d , $m_{u,d} \approx 5$ MeV) originating from the Higgs field compared to the relevant scales of QCD ($\Lambda_{QCD} \approx 200$ MeV). Therefore chiral symmetry is considered to be approximate (Section 1.1.3). However, even this approximate symmetry is spontaneously broken at low temperature due to $q\bar{q}$ condensation in the vacuum and the symmetry breaking emerges as mass differences of chiral partners (Section 1.1.4). At high temperature this

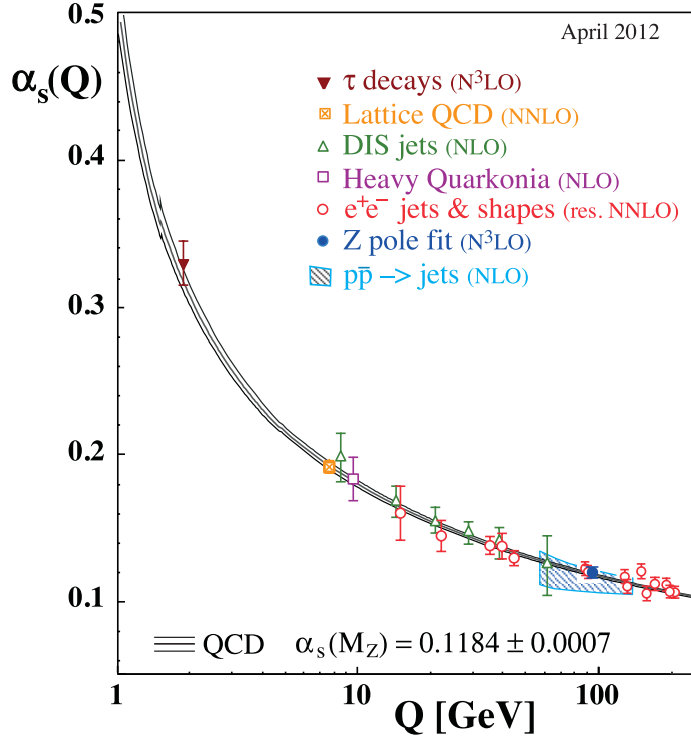


Figure 1.2: Various measurements on the strong coupling constant, α_S , vs. energy scale Q [10]. The degree of loop calculations in QCD perturbation theory used in the extraction of α_S are indicated in brackets.

condensation is evaporated and chiral symmetry is restored (Section 1.1.5). This transition has to be confirmed in order for QCD to be a viable theory of the strong interaction.

1.1.2 Chiral Symmetry

In QCD, a Lagrangian density is given by

$$\mathcal{L}_{QCD} = \bar{q}(i\gamma^\mu D_\mu - M_q)q - \frac{1}{4}G_{\mu\nu}^a G_a^{\mu\nu}, \quad D_\mu = \partial_\mu + ig_s \frac{\lambda_a}{2} A_\mu^a, \quad (1.1)$$

where q and A_μ^a denote quark and gluon fields, respectively. The g_s is a strong coupling constant and γ^μ and λ_a are Dirac and Gell-Mann matrices, respectively. $M_q = \text{diag}(m_u, m_d, \dots)$ is the current quark mass matrix. \mathcal{L}_{QCD} has several global symmetries as well as the local $SU(3)$ color gauge symmetry. The relevant symmetry here is chirality, which can be manifested by rewriting \mathcal{L}_{QCD} in terms of left- and right-handed quark fields. The handed-ness is defined as

$$q_L \equiv \left(\frac{1 - \gamma^5}{2} \right) q \quad \text{and} \quad q_R \equiv \left(\frac{1 + \gamma^5}{2} \right) q, \quad (1.2)$$

so that L and R correspond to helicity -1 and +1 in the limit of masses equal to zero. Since γ^5 anticommutes with γ^μ , $(\gamma^\mu \gamma^5 = -\gamma^5 \gamma^\mu)$,

$$\bar{q}_L \equiv q_L^\dagger \gamma^0 = \bar{q} \left(\frac{1 + \gamma^5}{2} \right) \quad \text{and} \quad \bar{q}_R \equiv \bar{q} \left(\frac{1 - \gamma^5}{2} \right). \quad (1.3)$$

Using those definitions and the fact that γ^5 is Hermitian ($\gamma^{5\dagger} = \gamma^5$ or $(\gamma^5)^2 = 1$),

$$\mathcal{L}_{QCD} = \bar{q}_L i \gamma^\mu D_\mu q_L + \bar{q}_R i \gamma^\mu D_\mu q_R - (\bar{q}_L M_q q_R + \bar{q}_R M_q q_L) - \frac{1}{4} G_{\mu\nu}^a G_a^{\mu\nu}. \quad (1.4)$$

For small quark masses compared to the QCD scale ($\Lambda_{QCD} \approx 200$ MeV), we can ignore the mass terms and \mathcal{L}_{QCD} is invariant under the separate transformations

$$q_L \rightarrow e^{-i\vec{\alpha}_L \cdot \vec{\tau}} q_L \quad \text{and} \quad q_R \rightarrow e^{-i\vec{\alpha}_R \cdot \vec{\tau}} q_R, \quad (1.5)$$

where $\tau^a = \sigma^a/2$ are operators in $(u - d)$ isospin space and $\vec{\alpha}_{L,R}$ are three real angles. The currents associated with this symmetries are respectively

$$\vec{j}_L^\mu = \bar{q}_L \gamma^\mu \vec{\tau} q_L \quad \text{and} \quad \vec{j}_R^\mu = \bar{q}_R \gamma^\mu \vec{\tau} q_R. \quad (1.6)$$

These symmetries are called chiral symmetries because they conserve quark handedness (chirality). Under the symmetry left-handed and right-handed fermions (Weyl fermions) are two different particles. In normal nuclear matter, they are the same particle. In fact, the left and right handed components together form a fermion (Dirac fermion).

1.1.3 Explicit Breaking of Chiral Symmetry

To reveal which symmetries are broken when mass terms are included, we rewrite this symmetry in an alternative way. The sum of the left- and right-handed currents gives the isospin current

$$\vec{j}^\mu = \bar{q}\gamma^\mu\vec{\tau}q. \quad (1.7)$$

While the difference gives the axial vector current

$$\vec{j}^{\mu 5} = \vec{j}_R^\mu - \vec{j}_L^\mu = \bar{q}\gamma^\mu\gamma^5\vec{\tau}q. \quad (1.8)$$

The corresponding transformations are respectively

$$q \rightarrow e^{-i\vec{\alpha}_V \cdot \vec{\tau}} q \quad \text{and} \quad q \rightarrow e^{-i\gamma^5 \vec{\alpha}_A \cdot \vec{\tau}} q. \quad (1.9)$$

Consider each transformation with the assumption that $\vec{\alpha}_V$ is small so that we can write the expression above as

$$\Lambda_V : q \rightarrow e^{-i\vec{\alpha}_V \cdot \vec{\tau}} q \simeq (1 - i\vec{\alpha}_V \cdot \vec{\tau}) q. \quad (1.10)$$

Remembering $\bar{q} = q^\dagger \gamma^0$, the kinetic term in \mathcal{L}_{QCD} transforms under Λ_V as

$$\begin{aligned}
\bar{q} (i\gamma^\mu D_\mu) q &\rightarrow \bar{q} (1 + i\vec{\alpha}_V \cdot \vec{\tau}) (i\gamma^\mu D_\mu) (1 - i\vec{\alpha}_V \cdot \vec{\tau}) q \\
&\simeq \bar{q} (i\gamma^\mu D_\mu) q - i\vec{\alpha}_V \cdot (\bar{q} i\gamma^\mu D_\mu \vec{\tau} q - \bar{q} i\gamma^\mu D_\mu \vec{\tau} q) \\
&= \bar{q} (i\gamma^\mu D_\mu) q.
\end{aligned} \tag{1.11}$$

The mass term in \mathcal{L}_{QCD} transforms under Λ_V as

$$\begin{aligned}
\bar{q} M_q q &\rightarrow \bar{q} (1 + i\vec{\alpha}_V \cdot \vec{\tau}) M_q (1 - i\vec{\alpha}_V \cdot \vec{\tau}) q \\
&\simeq \bar{q} M_q q.
\end{aligned} \tag{1.12}$$

On the other hand, under the axial vector transformation

$$\Lambda_A : q \rightarrow e^{-i\gamma^5 \vec{\alpha}_A \cdot \vec{\tau}} q \simeq (1 - i\gamma^5 \vec{\alpha}_A \cdot \vec{\tau}) q, \tag{1.13}$$

the kinetic term in \mathcal{L}_{QCD} transforms as

$$\begin{aligned}
\bar{q} (i\gamma^\mu D_\mu) q &\rightarrow q^\dagger (1 + i\gamma^5 \vec{\alpha}_A \cdot \vec{\tau}) \gamma^0 (i\gamma^\mu D_\mu) (1 - i\gamma^5 \vec{\alpha}_A \cdot \vec{\tau}) q \\
&\simeq \bar{q} (i\gamma^\mu D_\mu) q - i\vec{\alpha}_A \cdot (\bar{q} i\{\gamma^5, \gamma^\mu\} D_\mu \vec{\tau} q) \\
&= \bar{q} (i\gamma^\mu D_\mu) q.
\end{aligned} \tag{1.14}$$

However, the mass term transforma under Λ_A as

$$\begin{aligned}
\bar{q} M_q q &\rightarrow \bar{q} (1 - i\gamma^5 \vec{\alpha}_A \cdot \vec{\tau}) M_q (1 - i\gamma^5 \vec{\alpha}_A \cdot \vec{\tau}) q \\
&\simeq \bar{q} M_q q - 2i\vec{\alpha}_A \cdot (\bar{q} \gamma^5 \vec{\tau} q).
\end{aligned} \tag{1.15}$$

Thus, the mass term breaks chiral symmetry and the axial vector current is no longer conserved. However, if the masses are small compared to the relevant energy scale of QCD (≈ 200 MeV), the symmetry can be considered approximate.

1.1.4 Spontaneous Breaking of Chiral Symmetry (Hidden symmetry)

Let us check how mesons transform under Λ_V and Λ_A . We can form combinations of quark fields so that they carry the quantum numbers of mesons as follows,

pion-like state	sigma-like state	rho-like state	a_1 -like state
$\vec{\pi} \equiv i\bar{q}\vec{\tau}\gamma_5 q$	$\sigma \equiv i\bar{q}q$	$\vec{\rho}_\mu \equiv \bar{q}\vec{\tau}\gamma_\mu q$	$\vec{a}_{1\mu} \equiv \bar{q}\vec{\tau}\gamma_\mu\gamma_5 q$

Under the vector transformations Λ_V ,

$$\begin{aligned}
\pi_i : i\bar{q}\tau_i\gamma_5 q &\rightarrow i\bar{q}(1 + i\vec{\alpha}_V \cdot \vec{\tau})\tau_i\gamma_5(1 - i\vec{\alpha}_V \cdot \vec{\tau})q \\
&\simeq i\bar{q}\tau_i\gamma_5 q + \alpha_V^j \bar{q}\gamma_5[\tau_i, \tau_j]q \\
&= i\bar{q}\tau_i\gamma_5 q + i\epsilon_{ijk}\alpha_V^j \bar{q}\gamma_5\tau_k q
\end{aligned} \tag{1.16}$$

where the commutation relation $[\tau_i, \tau_j] = i\epsilon_{ijk}\tau_k$ is used in the last line. In terms of our definition of pion-like fields, Equation 1.16 can be written as

$$\vec{\pi} \rightarrow \vec{\pi} + \vec{\alpha}_V \times \vec{\pi}. \tag{1.17}$$

The isospin direction of the pion is effectively rotated by α_V . Replacing γ_5 with γ_μ , we obtain a similar result for a ρ meson under the Λ_V ,

$$\vec{\rho}_\mu \rightarrow \vec{\rho}_\mu + \vec{\alpha}_V \times \vec{\rho}_\mu. \tag{1.18}$$

Therefore, we can consider the vector transformation Λ_V as a rotation in isospin space and the corresponding conserved vector current as an isospin current, which is conserved in strong interactions.

Under the axial vector transformations Λ_A , the pion transforms as

$$\begin{aligned}
\pi_i : i\bar{q}\tau_i\gamma_5q &\rightarrow i\bar{q}\left(1 - i\gamma^5\vec{\alpha}_A \cdot \vec{\tau}\right)\tau_i\gamma_5\left(1 - i\gamma^5\vec{\alpha}_A \cdot \vec{\tau}\right)q \\
&\simeq i\bar{q}\tau_i\gamma_5q + \alpha_A^j\bar{q}\{\tau_i, \tau_j\}q \\
&= i\bar{q}\tau_i\gamma_5q + \frac{1}{2}\alpha_{Ai}\bar{q}q,
\end{aligned} \tag{1.19}$$

where the anti-commutation relation $\{\tau_i, \tau_j\} = \frac{1}{2}\delta_{ij}$ and $\gamma_5\gamma_5 = 1$ are used. In terms of the meson fields, Equation 1.19 reads

$$\vec{\pi} \rightarrow \vec{\pi} + \vec{\alpha}_A\sigma. \tag{1.20}$$

The transformation Λ_A rotates the pion and sigma meson into each other. Similarly the rho rotates into the a_1 ,

$$\vec{\rho}_\mu \rightarrow \vec{\rho}_\mu + \vec{\alpha}_A \times \vec{a}_{1\mu}, \tag{1.21}$$

where again the commutation relation $[\tau_i, \tau_j] = i\epsilon_{ijk}\tau_k$ and the anti-commutation relation $\{\gamma_5, \gamma_\mu\} = 0$ are used. If Λ_A is a symmetry of the QCD Lagrangian, these relations (Equations 1.20 and 1.21) imply that those mesons rotated into each other have to have the same eigenvalues, like masses. However this is not the case, since $m_\rho = 770$ MeV and $m_{a_1} = 1260$ MeV [11]. The chiral symmetry is broken at our energy scale. In 1961 Nambu and Jona-Lasinio suggested this is because of a nonzero vacuum expectation value (VEV) of $q\bar{q}$ condensation [12] Although they did not know that the condensed pair of fermions were quarks.

$q\bar{q}$ condensation The idea of $q\bar{q}$ condensation came from the analogy of a superconductor [13][14]. In a super conductor, an attractive force between two electrons via electron-phonon interaction (Cooper pair) lowers the energy of system and causes instability in vacuum of the system. In this case, there is an attractive color-singlet channel between q and \bar{q} . The attraction between a quark and antiquark causes an instability in the QCD vacuum. If the energy required for $q\bar{q}$ pair production is small, or more specifically, the quark mass and kinematic energy are small compared to its binding energy, the vacuum prefers to produce $q\bar{q}$ pairs until the production energy becomes comparable to the binding energy. As discussed below, the $\langle q\bar{q} \rangle$ serves as a mass term of quarks. This means as $q\bar{q}$ density increases, more energy is necessary to produce a $q\bar{q}$ pair. The $q\bar{q}$ has to have the vacuum quantum numbers, that is, angular momentum and total momentum are zero like a Cooper pair [15]. The pair has to be $q\bar{q}$, instead of qq or $\bar{q}\bar{q}$ so that they can form the color singlet. Such a pair, opposite momentum and spin, and particle-antiparticle pair, must have chirality ± 2 as shown in Figure 1.3. This nonzero VEV of chirality spontaneously breaks the chiral symmetry in QCD vacuum. Spontaneously

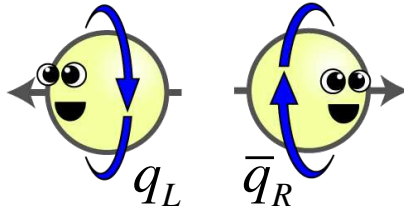


Figure 1.3: Schematic picture of a quark anti-quark pair. Credit goes to [Flip Tanedo](#).

broken symmetry means that while the Lagrangian of the system contains some symmetry, the symmetry is not realized in the ground state¹.

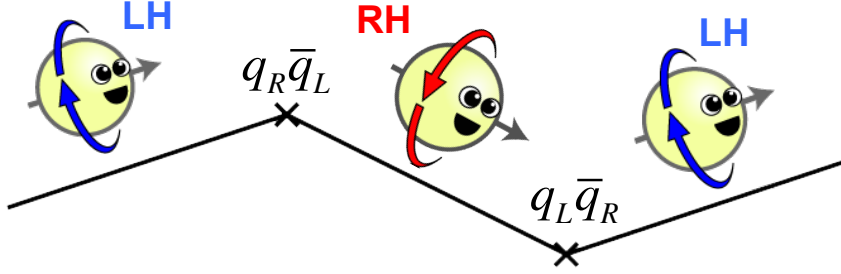


Figure 1.4: Schematic picture of QCD dynamical mass generation. Credit goes to [Flip Tanedo](#).

QCD dynamical mass generation Imagine a traveling q_L , which is an eigenstate of a chiral transformation, collides with a $q_R \bar{q}_L$ and annihilates the \bar{q}_L in the pair, freeing q_R which continues to propagate. The q_R carries the same momentum (so the line should be straight in practice) and quantum numbers as the incoming quark except for chirality as pictured in Figure 1.4. This process can be interpreted as $\langle q_R \bar{q}_L \rangle$ mixing right and left chirality. This interaction could be written in the Lagrangian as $\langle \bar{q} q \rangle \bar{q} q$ in a mean field approximation framework (many-body theory) and serves as a mass term for quarks. Since this term does not explicitly break chiral symmetry if you take into account chirality of those $\langle q_R \bar{q}_L \rangle$, it is referred to as spontaneous symmetry breaking. This is similar to the Higgs mechanism except the mass generating field is the $q \bar{q}$ field instead of the Higgs field.

¹See Appendix C.1 for Spontaneous symmetry breaking.

1.1.5 Restoration of Chiral Symmetry

According to thermal quantum field theory, the spontaneously broken chiral symmetry can be restored at high temperature [16]. At high temperatures, due to kinematical energy, the pair production energy increases. If it exceeds the binding energy of $q\bar{q}$ pairs, there is no more condensation. Roughly speaking, $q\bar{q}$ pairs evaporate and chiral symmetry is restored. In other words, the $q\bar{q}$ pairs can not feel the symmetry-breaking potential at the vacuum. All they can feel is high order terms such as pair-pair interaction (density effects) in the potential, which has unbroken symmetry. High density effects are also considered in a similar manner. In this case, what prevents the condensation is a chemical potential of the $q\bar{q}$'s. As energy density becomes higher, due to the pair-pair interaction, the chemical potential, the energy to produce a $q\bar{q}$ in the system increases, and then the condensation of $q\bar{q}$ disappear.

Since spontaneous chiral symmetry breaking is a natural outcome of QCD, there has to be chiral symmetry restoration in a strongly interacting system if QCD is the theory of the strong interaction. Therefore, an observation of chiral symmetry is a necessary check for QCD as a theory of the strong interaction. Since vacuum can not be observed directly, its excitations (i.e. resonances) are observed instead to search for this phase transition.

1.2 Hadronic Resonances

Hadronic resonances are unstable particles which strongly decay into stable particles shortly after they are produced. Due to their short lifetimes, resonances are not directly observed. The properties of resonance particles are obtained indirectly via reconstruction. Reconstruction is the process of forming a resonance from the daughter particles after decay. The dynamical information of the resonance decaying in the medium, such as their masses and widths, is converted into kinematic information of the daughter particles. Therefore, the dynamical information of the resonance in medium can be restored from the kinematic information of the daughters in vacuum, which is measured in experiments. This makes resonance particles ideal probes to study medium effects.

A resonance particle is usually characterized by the Breit-Wigner formula, in which the mass is related to the real part of the self-energy of the resonance (pole position of the propagator) and the width is related to the imaginary part of the self-energy, or more concisely, attenuation of resonance during propagating through medium. The propagator includes interactions between resonance and medium, so called radiative corrections, and thus, the medium effects the mass and width.

1.2.1 Breit-Wigner Formula

Near the resonance mass M_0 , the invariant mass distribution, which is obtained from daughter particles' momentum and energy, is given by the

Breit-Wigner formula,

$$f(E) \propto \frac{1}{(E - M_0)^2 + \Gamma^2/4}, \quad (1.22)$$

where Γ is the decay rate of the resonance, defined as

$$\Gamma \equiv \frac{\text{Number of decays per unit time}}{\text{Number of particles present}}. \quad (1.23)$$

The Breit-Wigner distribution is also known as the Cauchy distribution and is a well-known statistical distribution. If the resonance is broad, Γ has some E dependence, and the invariant mass distribution may deviate from the Breit-Wigner distribution.

1.2.2 Mass, Width, and Medium Effects

By applying the optical theorem, which is related to the unitarity of a S-matrix, the Breit-Wigner formula is derived from a resonance particle's propagator [17], which has a self-energy term, $M^2(p^2)$, in its denominator,

$$\frac{1}{p^2 - m_0^2 - M^2(p^2)}, \quad (1.24)$$

where m_0 is the bare mass of the resonance. The resonance mass is defined as a pole position,

$$m^2 \equiv m_0^2 + \text{Re}M^2(m^2). \quad (1.25)$$

The imaginary part of the self-energy, $\text{Im}M^2(p^2)$, is connected to attenuation (decay) of the resonance via the optical theorem. Because the self-energy includes all interactions with the medium, the mass and width also include medium effects. The restoration of chiral symmetry at high temperature predicts a mass shift and width broadening [18] [19].

1.2.3 Hadronic Resonances in Heavy Ion Collisions

System evolution In a thermal statistical description of heavy ion collisions the state of matter is expected to go through two characteristic stages, chemical freeze-out and kinetic freeze-out. After two high energy ions collide, nuclear matter with a high temperature and high density is created. As the system expands, it cools and reaches a hadronization point, where partons form hadrons. The produced hadrons still can change flavors via inelastic collisions. Then, after a period of time the particles in the system do not change particle species further, i.e., the diversity of particles is fixed. This point is referred to as chemical freeze-out (vanishing inelastic collisions) from the analogy of chemical reactions. After that point, as the system expands further, particles interact increasingly less often because they are separated more than their interaction range. At some point, the particles stop interacting and the momenta are fixed, known as kinetic freeze-out (vanishing elastic collisions). Since experimentally observed particles experience these stages after their hadronization, it is important to understand how and when these two transitions happen.

Rescattering and Regeneration One way to study these two transitions is by investigating rescattering and regeneration effects on resonance productions. The hadronic decay daughters from resonances which decay between chemical and kinetic freeze-out rescatter with other hadrons, mostly pions. This results in loss of reconstructable resonance signals. On the other hand, in

the presence of an abundance of hadrons in heavy ion collisions, these hadrons may form (regenerate) resonance states, and thus contribute to the final measured yield. The interaction cross sections between particles can determine the time difference between the chemical and kinetic freeze-out [20].

1.2.4 Decay Channels

There are two main types of decay channels. A hadronic decay, where daughter particles are hadrons or a leptonic (non-hadronic) decay, in which daughter particles are leptons or γ 's.

Hadronic decays are the dominant decay channels. However, in hadronic decay channels the daughter hadrons interact strongly with medium and the resonance signals from the early stage of evolution might be washed out during the later hadron gas phase. Conversely, it means these channels are sensitive to the hadronic gas phase as explained above.

In leptonic decay channels, daughter leptons do not strongly interact with the hadronic medium and the resonance signals can be extracted from the entire stage of evolution without the rescattering effects. These channels are often called clean probes. However, due to the smaller coupling constant of the electromagnetic interaction, the branching ratios are about $10^{-4} - 10^{-5}$ times smaller than the branching ratios from hadronic decay channels, where the strong interaction is relevant.

The hadronic resonances measured by the STAR experiment are listed in Table 1.1 along with the specific decay channels. By comparing the two

particle	Mass (MeV/c ²)	Width (MeV/c ²)	Lifetime (fm/c)	Decay channel
$\rho^0(770)$	775.49 ± 0.34	149.1 ± 0.8	1.32	$\pi + \pi$
$\omega(782)$	782.65 ± 0.12	8.49 ± 0.08	23.2	$e^+ + e^-$
$K^{*0}(892)$	895.94 ± 0.22	48.7 ± 0.8	4.05	$K + \pi$
$\phi(1020)$	1019.46 ± 0.020	4.26 ± 0.04	46.3	$K + K, e^+ + e^-$
$\Sigma^{*+}(1385)$	1382.80 ± 0.35	36.0 ± 0.7	5.48	$\Lambda(\rightarrow p + \pi) + \pi^+$
$\Sigma^{*-}(1385)$	1387.2 ± 0.5	39.4 ± 2.1	5.01	$\Lambda(\rightarrow p + \pi) + \pi^-$
$\Lambda^*(1520)$	1519.5 ± 1.0	15.6 ± 1.0	12.6	$K + p$

Table 1.1: Hadronic resonances measured at STAR with their properties reported in PDG [21].

decay modes it might be possible to investigate the early stage of the system where we expect QGP formation and chiral symmetry restoration. Vector mesons can decay through the hadronic decay channels and the leptonic decay channels via a virtual photon state. The ϕ meson is one of the few resonance particles in which measurements from both leptonic and hadronic decay channels are possible.

However, due to the large number of tracks in heavy ion collisions, resonances signals must be separated from a background. Particle identification is crucial to suppressing the background and enhancing the signal over background ratio of the measurement.

1.3 Outline

In this dissertation the possible signatures of chiral symmetry restoration are investigated by measuring $\phi(1020)$ mesons from the di-electron channel. Chapter 2 describes the STAR experiment at the Relativistic Heavy Ion Collider at Brookhaven National Laboratory on Long Island, New York. Chap-

ter 3 is devoted to an overview of particle identification methods. In Chapter 4 the details of $\phi \rightarrow e^+e^-$ analysis are described. In Chapter 5 the results of $\phi \rightarrow e^+e^-$ analysis are reported and compared to a theoretical model. This dissertation is concluded in Chapter 6.

Chapter 2

Experimental Set Up

2.1 Introduction

The data analyzed in this work was taken with the STAR detector on the Relativistic Heavy Ion Collider at Brookhaven National Laboratory (BNL), located on Long Island, New York. The RHIC project began in the late 1980s followed by 10 years of development and construction. The first Au+Au collisions at a center of momentum energy per nucleon $\sqrt{s_{NN}} = 130$ GeV took place in the summer of 2000. The primary physics goals of RHIC are to produce and investigate properties of the QGP with heavy ion collisions and to investigate the spin structure of nucleons with polarized proton collisions. In this chapter the RHIC experimental facility and the STAR detector are described in detail.

2.2 Relativistic Heavy Ion Collider (RHIC)

The RHIC experimental facility consists of accelerators, transfer lines, detectors, and computational facilities for data storage and analysis. The main facility is the Relativistic Heavy Ion Collider. RHIC has the capability to accelerate and collide a large variety of particle configurations such as d+Au,

Cu+Cu, Au+Au, and U+U at energies from $\sqrt{s_{NN}} = 7$ to 200 GeV for heavy-ions and polarized and unpolarized p+p at $\sqrt{s_{NN}} = 62.4$ to 500 GeV. The schematic diagram of the RHIC accelerator complex is shown in Figure 2.1a.

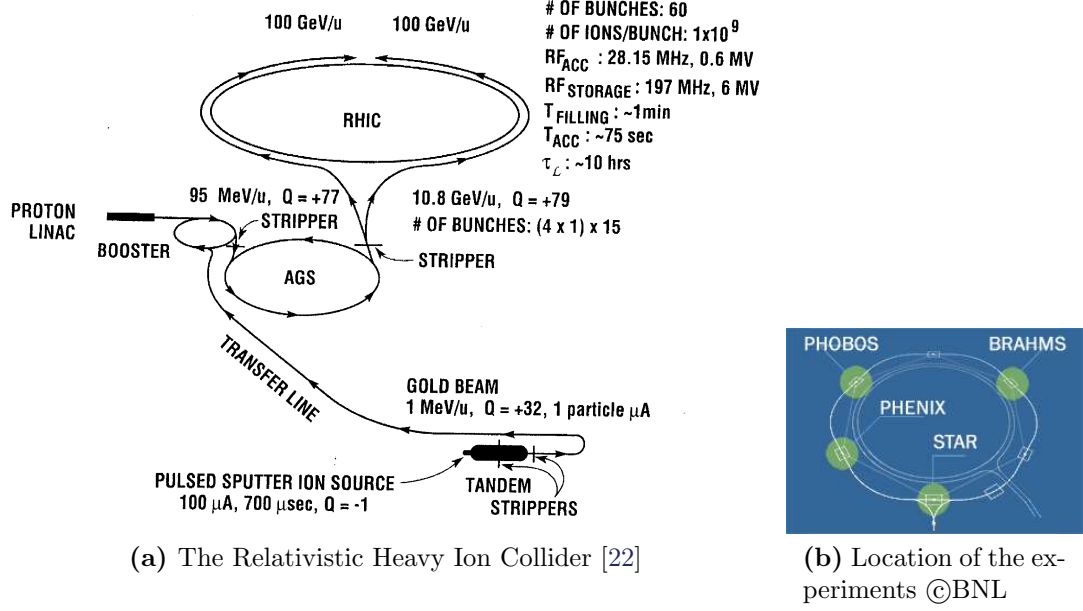


Figure 2.1: The Relativistic Heavy Ion Collider complex

The collider has two concentric rings: a “Blue” ring for clock-wise ion revolution and a “Yellow” ring for counter clock-wise ion revolution. As shown in Figure 2.1b, the rings are not circular, but have six straight sections and six arc sections, and total 3.8 km in circumference. There are six intersection points at the center of each straight section and four of them are occupied by the STAR, PHENIX, BRAHMS, and PHOBOS experiments [23] as shown in Figure 2.1b. As of 2013, The BRAHMS and PHOBOS had already completed their physics programs, while STAR and PHENIX continue to take data.

Figure 2.1b also shows the operational steps of accelerating the beams and a brief description of the operations is as follows [22]. For Au ion beams, negatively charged ions are produced from a pulsed sputter ion source at the Tandem Van de Graaff, which accelerates the ions to an energy of 1MeV/nucleon(A) and partially strips their electrons. After passing through another stripping foil and charge selection magnets, the ions with a charge of +32 are delivered to the Booster synchrotron where they are accelerated to the injection energy, 95MeV/A, of the Alternating Gradient Synchrotron (AGS). For proton beams, polarized protons are sourced at the Linear Accelerator (LINAC) where they are accelerated to the injection energy of AGS. At the entrance and exit of AGS, the ions are fully stripped and reach a charge state of +79. The ions or protons are bunched and accelerated to RHIC injection energy of 10.8 GeV/A before being injected into RHIC via the AGS-to-RHIC Beam Transfer Line (ATR). In RHIC, two counter revolving beams can be accelerated up to the maximum design energy of 100 GeV/A for heavy ions and 250 GeV/A for protons.

For more than 10 years after the first run, the RHIC collider experts have been successfully improving not only luminosities but also the range of the colliding energy and particle species as shown in Figure 2.2

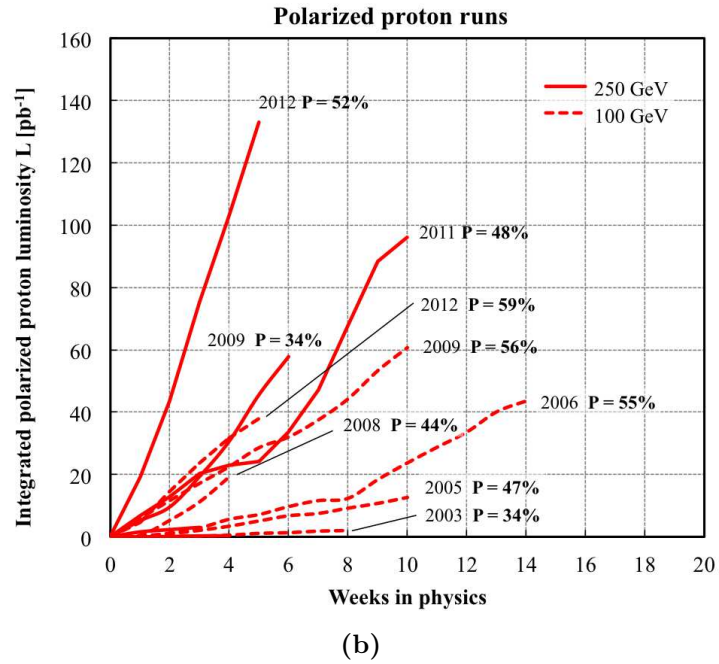
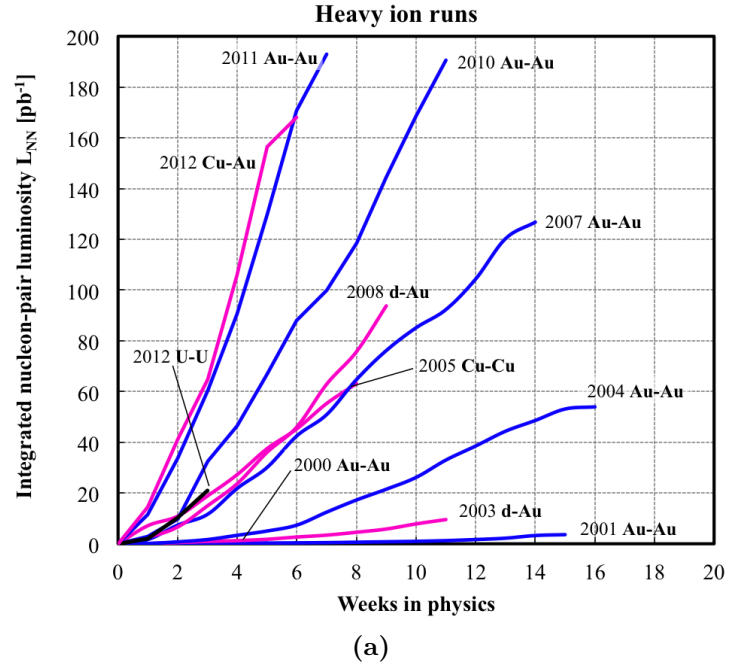


Figure 2.2: RHIC integrated luminosity (credit goes to [W. Fischer](#))

2.3 STAR Experiment

2.3.1 Overview

The Solenoidal Tracker at RHIC (STAR) is a detector which has been developed for tracking thousands of particles produced in heavy-ion collisions at RHIC. The STAR detector and its data acquisition (DAQ) system are located at the 6 o'clock intersection position of RHIC. One of the main physics goals of STAR is to investigate the behavior of strongly interacting matter at a high energy density and high temperature. This is done via measurements of out-coming particles with multiple observables such as high p_T jets and particle correlations. In particular, the large acceptance ($-1 \leq \eta \leq 1$ and full azimuthal angle) and high efficiency of the STAR detector make it an ideal detector to study non-perturbative aspects (low p_T) of the heavy ion collisions as well as perturbative aspects (high p_T). Due to this ability to simultaneously measure perturbative and non-perturbative observables, correlation studies, like jet quenching, is possible [24].

The STAR detector (Figure 2.3) is a collection of many detectors, which are categorized into two types. One type is the tracking and particle identification detectors, which include the Time Projection Chamber (TPC), Electro-Magnetic Calorimeters (EMC), and Time Of Flight (TOF). The other type is the event triggering detectors: Zero Degree Calorimeter (ZDC), Beam-beam Counters, and upgraded Primary Vertex Position Detector (upVPD). A nice overview of the STAR detector can be found in Reference [24] but we will focus on the TPC and TOF, which are the detectors necessary for this analysis

along with some of the trigger detectors.

Solenoidal Tracker At RHIC : $-1 < \eta < 1, 0 < \phi < 2\pi$

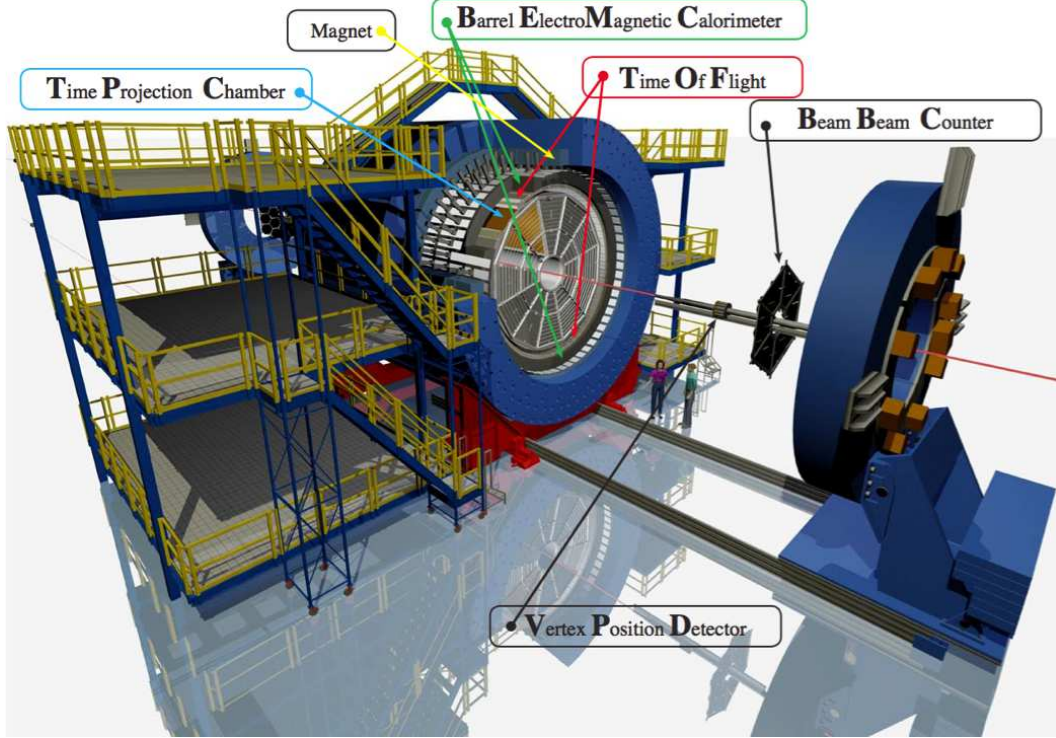


Figure 2.3: The STAR detector (credit goes to [A. Schmah](#))

2.3.2 Time Projection Chamber (TPC)

The TPC [25] is the main tracking detector of the STAR experiment and it is designed to provide information on momentum and energy loss of charged particles in heavy ion collisions over a large solid angle in high precision. This large acceptance is very important to study, for example, particle correlations in an event-by-event basis and it also helps to increase statistics for rare processes such as resonances with decay channels with small branching

ratios. A schematic picture of the TPC is given in Figure 2.4.

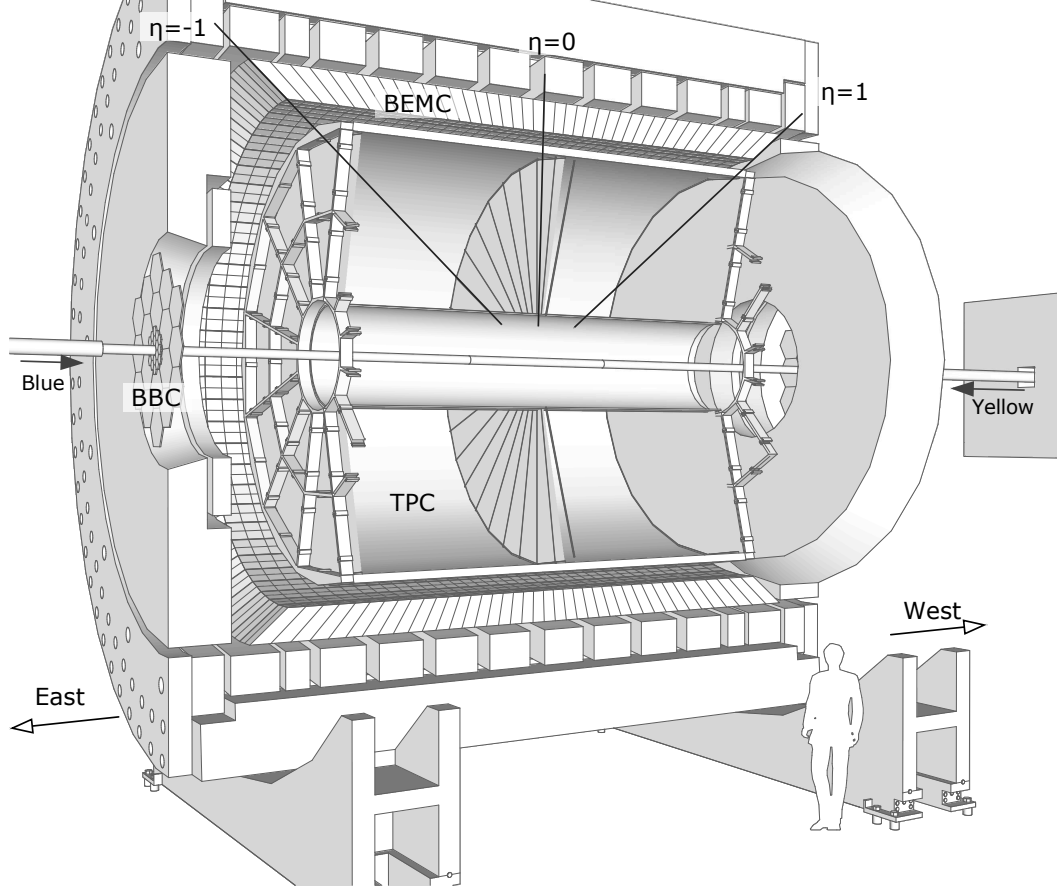


Figure 2.4: Cutaway view of the TPC (credit goes to [T. Sakuma](#))

The description of the STAR TPC will be divided into four parts: **geometry**; **gas**, which is essential to produce ionization signals in the TPC; **electric field**, in which electrons drift towards anode wires; and **readout system**.

Geometry: The TPC sits in a large solenoidal magnet that produces a maximum of ± 0.5 T magnetic field and it is 4.2 m long and 4 m in diameter.

It covers pseudo-rapidity $|\eta| \leq 1$ and 2π in azimuthal angle. **Gas:** The TPC is filled with a P10 gas mixture, that is a mixture of 90% Argon and 10% Methane. Argon (a noble gas) is chosen because it requires low electric field intensities for avalanche formation and has a fast drift velocity. Methane is added to suppress high energy photons caused by excited Argon atoms. The Argon atoms are excited, instead of being ionized, by particles passing by [26]. The pressure of the gas is 2 mbar higher than the atmospheric pressure to prevent contamination by electronegative gas such as H_2O and O_2 , which capture the drifting electrons, reduce drift time, and reduce the efficiency of creating avalanches at read out pads. **Electric field:** A well-defined, uniform, electric field of 135 V/cm along beam axis is applied so that ionized gas particles (electrons) drift into the readout channels on both sides of the TPC. The uniform electric field is created by a thin conductive cathode membrane at the center, concentric inner and outer field-cage cylinders (which are respectively 0.5 m and 2 m from beam axis), and anode wires at the readout end cap. **Read-out system:** The readout system is mounted on aluminum support wheels at both end caps of the TPC. It consists of Multi-Wire Proportional Chambers (MWPC) and readout pads (cathode plane in the Figure 2.5). The drifting electrons avalanche in high electric fields between the shielding grid at ground potential and anode wires. Positive ions created in the avalanche induce image charges on the readout pads. The gating grid prevents the slow positive ions from entering the drift region by closing the gates after electrons have drifted through.

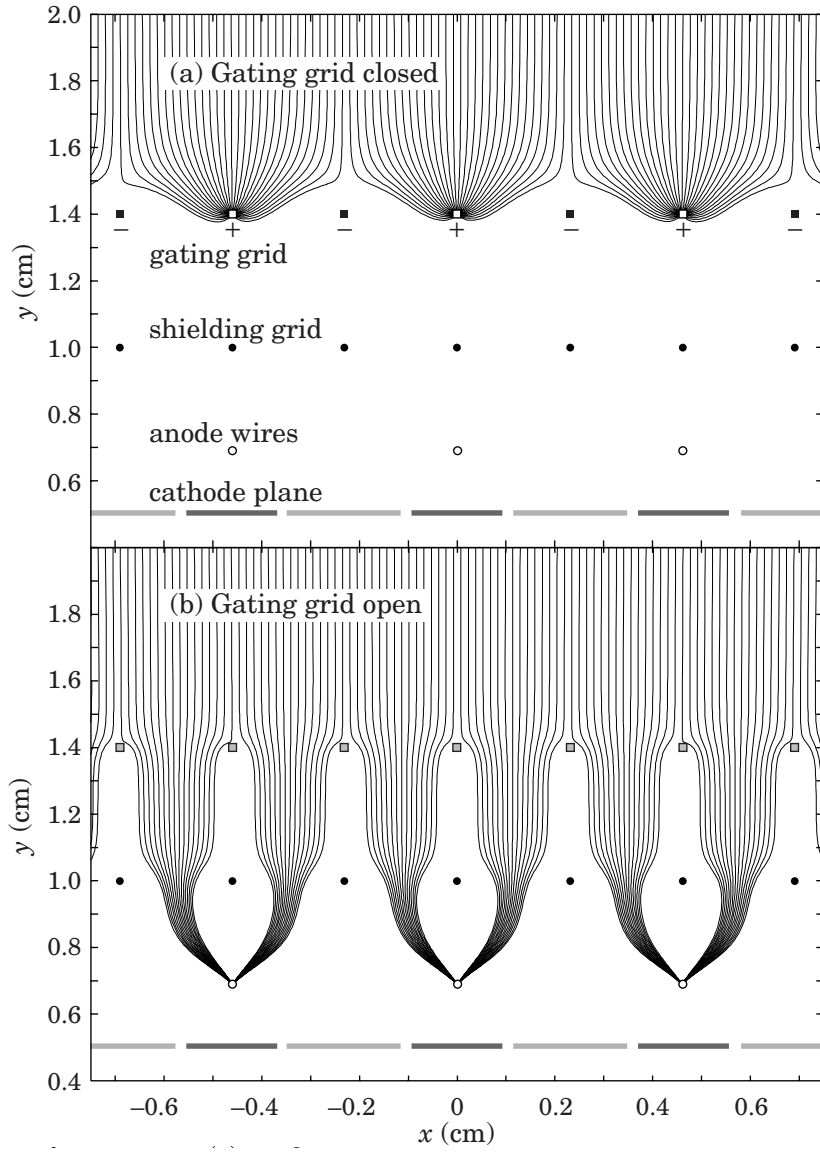


Figure 2.5: The gating grid at the readout pads [27] section 28.10.

Basic Mechanism

The most important function of the TPC is to reconstruct the paths of particles. When a charged particle passes through the gas, it ionizes the gas molecules and creates electrons and ions. Due to a sufficiently strong electric field, the electrons separate from the ions and drift to the ends of the TPC. The electrons drift with an average velocity of $5.45 \text{ cm}/\mu\text{s}$ to the readout channels (end caps). Different drift distances result in different readout times. With this timing information and the 2D position on the read out pads, 3D tracks can be reconstructed. For this reason, it is called the “Time Projection” Chamber. Since magnetic fields curve a charged particle’s path according to its momentum, the momentum can be calculated from the curvature of the path according to following equation,

$$p_T = \frac{e}{c}BR = 0.3BR, \quad (2.1)$$

where B is the strength of a constant magnetic field and R is the radius of curvature. Since particles continuously lose their energy and momentum as they travel through the gas in the TPC, measured momenta are corrected using expected energy loss values, which are functions of a particle’s velocity. By default, a pion mass is assumed for all particles to estimate velocity. This is a good approximation at high momentum for other species of particles. However, at low momentum the pion mass assumption causes the momentum away from the true value for other species of particles. Fortunately, after particle identification this problem can be corrected using simulation.

Track Reconstruction

During track reconstruction, ionization clusters are connected to form a 3D trajectory of a charged particle. The trajectory is fit with a 3D helix model, including the energy loss as a second order effect. The resulting helix is called a ***global track***, which is used to reconstruct the primary collision vertex. The vertex resolution increases as the number of tracks in the reconstruction increases and can reach several hundreds of nm in Au+Au collisions. Global tracks with a distance to the primary vertex, *Distance of Closest Approach (DCA)*, smaller than 3 cm are fitted again with the primary vertex as an additional point. The number of clusters used in the fit is called ***Number of Fit Points*** and used later in this analysis for track quality assurance. These tracks with a DCA less than 3 cm are categorized as ***primary tracks***.

dE/dx Measurement

The ionization energy loss per unit length dE/dx of charged particles provide another important piece of information. The intensity of the readout signal is related to the energy loss of the passing particle. Using the Bichsel function, an extension of the Bethe-Bloch formula, which shows expected dE/dx as a function of velocity, the velocity of the particle is calculated. Finally, the mass of the particle is obtained from the velocity and the momentum. Therefore, dE/dx is used for PID.

Calibration

Several calibrations have to be done to achieve precise momentum measurement. The main sources of error in the momentum measurement are from changes in the drift velocity and electric and magnetic field distortions [28]. The drift velocity is calibrated using a narrow specific wavelength ($\lambda = 266$ nm) laser which can produce ionization in the TPC equivalent to relativistic particles [29]. Laser events are taken for this purpose in every beam fill. The potential sources of field distortions are field misalignment which arises from slightly unparallel E and B fields, space charge distortion caused by a buildup of positive charged ions in the TPC gas, and grid leak of ionic charge into the main TPC volume from the high gain anode region. Calibrations can be done for those distortions by applying a residual space charge model with parameters. The parameters are determined by minimizing χ^2 values of the helix fit of good quality tracks.

2.3.3 Time Of Flight System (TOF)

Introduction

The TOF system was built to improve the PID capability of the STAR experiment and was designed to provide a time resolution less than 100 pico (10^{-9}) seconds to achieve this goal. The heart of this detector is the Multi-gap Resistive Plate Chamber (MRPC) which has been developed at CERN for the ALICE detector at the LHC [30]. The MRPC is based on relatively inexpensive technologies and materials, which enabled the building of the TOF

system over a large area within a reasonable budget. After dedicated R&D and remote construction of the TOF detectors [31], about 75% of trays were installed in 2009. The full 120 trays have been installed and taking data since 2010. Since then almost all of the analyses in the STAR collaboration have exploited TOF information and the TOF system has become an indispensable part of the STAR experiment.

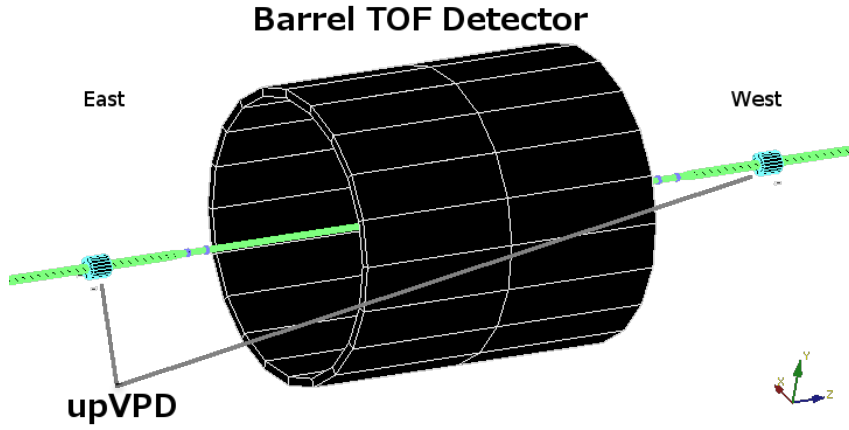


Figure 2.6: Schematics of the TOF system: Barrel TOF trays (60 trays on each east and west side of the TPC) and upVPDs on the beam pipe on the east and west sides

A TOF system measures the time span that particles spend to fly from one point to another. In the STAR experiment the first point is assumed to be the collision vertex. So the TOF information is calculated for only primary tracks, not for global tracks, which might contain secondary tracks, like weakly decaying daughter particles. The collision time (start time) is determined by upgraded Vertex Position Detector (upVPD). The second time measurement

is at the stop-side-detectors, barrel TOF trays, which measures the time at which a particle reaches the detector. The TOF is not enough information to provide PID, which will ultimately depend on the particle velocity. Therefore, path length (flight distance) is also required. The path length is estimated by extrapolating the track helix from the TPC onto a channel on the TOF trays, that matched the TOF hit.

In the rest of this section, the start side and stop side detectors are explained in detail as well as the software projects such as calibration and track matching.

upVPD (start side detector)

The upVPD detector is designed to measure the collision time of an event with a resolution of 10 to 20 ps. The upVPD consists of two identical assemblies (Figure 2.7a) mounted on the west and east side of the beam pipe at $z \pm 5.7$ m covering $4.24 < |\eta| < 5.1$ (see Figure 2.3 and 2.7b). Each assembly is composed of 19 cylindrically shaped channels. Each channel has three layers: a lead layer that enhances signals by showering, a scintillator that converts the shower into light, and a photo multiplier tube (PMT) which collects the light. They mostly detect spectators, nucleons not directly involved in the collisions, moving forward at a velocity near the speed of light. In principle, if given the collision location (the primary vertex position) from the TPC, the collision time can be calculated from a single upVPD channel. However, to improve the timing resolution, at least one lit channel on each side is required

to calculate the start time. The coincident hits on both sides are also used as an event trigger. Additionally, the upVPD provides independent measurements of collision points along the beam axis. This detector has been developed at Rice University.

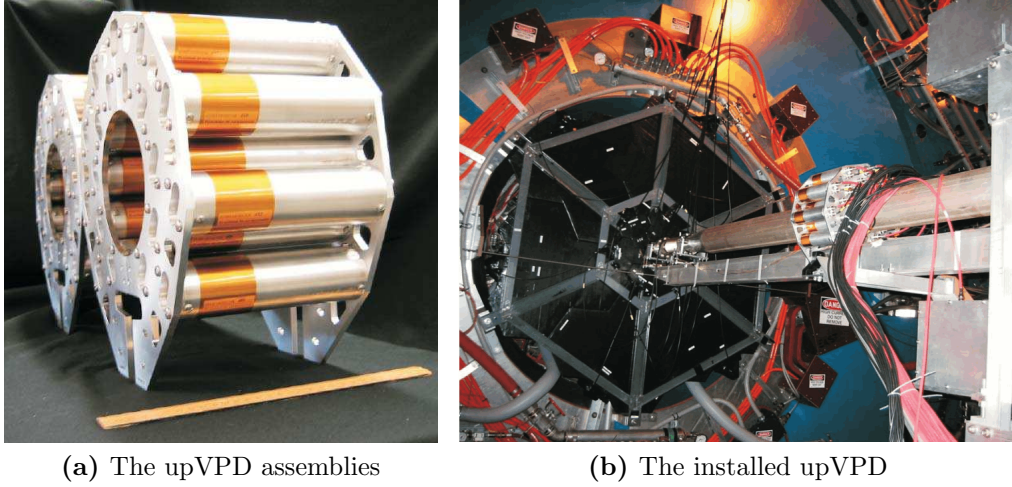


Figure 2.7: The upVPD (credit goes to [W. Lope](#))

TOF trays (stop side detector)

All 120 TOF trays cover $-1 \leq \eta \leq +1$ and 2π in azimuth, located just outside of the TPC [32][33]. Each tray has 32 Multi-gap Resistive Plate Chambers (MRPC) each with 6 readout channels. Therefore one tray has 192 readout channels and the total TOF system has 23,040 channels. The trays are filled with gas that is 90 to 95% Freon R-134a, and a smaller amount of isobutane, which is a quencher to obtain less noise and stable performance. The gas continuously flows during operation to suppress noise rates. Freon is

used because it improves timing resolution and enables the MRPC to operate at a high rate. A disadvantage of freon is that it increases power consumption again due to the high electronegativity, because only a small fraction of electrons produced in avalanche can contribute to the signal before being captured by the freon molecules. The trays also have a cooling system to prevent overheating. All trays were constructed at the University of Texas at Austin. Before installation at STAR they were checked carefully for gas leaks and also tested for acceptable noise rates . During actual data taking at BNL, the noise rate measurements are occasionally performed to check gas quality and electronics.



(a) TOF tray with modules



(b) Readout pads

Figure 2.8: TOF tray construction

Multi-Gap Resistive Plate Chamber (MRPC)

The MRPC is the most essential part of the TOF system. The MRPC is comprised of alternating layers of resistive plates (0.54 mm thick glass) and ionization gas gaps (220 μ m) between two graphite layers on which high voltages (± 7 kV) are applied to generate an electric field across the gaps. Readout electrodes attached on the outermost sides of the MRPC. In order to readout signals via capacitive coupling, the readout electrodes are separated from the high voltage coating by thin insulating sheets. The MRPC measures a signal when a charged particle travels through and interacts with the gas molecules and ionizes them. If the applied voltage is high enough, the positive ion and electron are pulled apart before they can be combined together again. As the electron is accelerated by the high electric field, it ionizes other molecules and causes an avalanche. The gas gaps in an MRPC provide both sources of the primary ionization and gas gain (amplification) through the avalanche process.

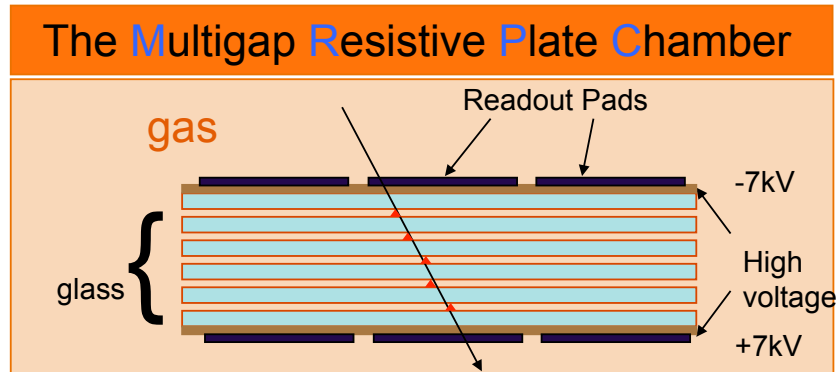


Figure 2.9: Ionization in the MRPC

By changing the applied high voltage, an MRPC could be operated in “streamer” (a spark discharge) mode or “avalanche” mode. When operating in streamer mode, in general, the charge generated by a streamer discharge is a factor of 10 to 20 times larger than that in an avalanche. It does not require signal amplifiers and sophisticated readout electronics. The operation in streamer mode, however, has many problems: low rate limits, time shift with rate, etc.. In STAR, the MRPCs are operated in avalanche mode.

There are several features characterizing performance of an MRPC [34][35][36]: operating rate, required high voltage, time resolution, and spatial resolution. The first two characteristics are related to how low the average avalanche charge is for a given threshold in the readout electronics. If the average avalanche charge is big, the efficiency and rate decrease because the surface of the resistive plates becomes charged and reduces the electric field across the gas gaps until it is restored by charge flowing through the resistive plates. The average avalanche charge is determined by the difference between the minimum charge that the readout electronics can detect and the maximum charge that can be created in the gas gaps. A low average avalanche charge is achieved by using a heavy gas which has a short mean free path compared to the size of a gas gap. In the heavy dense gas, most of the incoming particles initiate an avalanche within a small distance in a gas gap which leaves enough distance to develop enough charge (gas gain) to be readout. This short mean free path also improves the timing resolution since the timing resolution at the MRPC level is determined by variation of the primary ionization positions [34].

Multi-gap RPCs are less noisy than mono-gap RPCs because, in MRPCs, the avalanches in different layers are independent, so a noise can cause a small avalanche in one layer only, while in a mono-gap RPC noise can cause a large avalanche and negatively affect time resolution. Also, spacial resolution in a multi-gap is better than that in a mono-gap because in smaller gaps, the avalanche cannot grow in the transverse direction as much. This feature is important to improve the matching efficiency of TOF hits to TPC tracks.

All MRPCs have been produced by the University of Science and Technology of China (USTC) and the Tsinghua University, China.

Calibration

To accomplish the desired high resolution timing measurement ≈ 100 ps, several calibrations [37] are applied to both the start and stop sides. These calibrations include the Integral Nonlinearity (INL) correction, slewing correction, hit position correction, and T_0 correction. The INL correction is necessary to address the unequal time spans of time steps (25 ps) in clocks generated in digitizing chips. This correction is unique but fixed for each digitizer board. A slewing correction is applied to correct time shifts due to signal size (time over threshold) difference. A hit position correction is used to adjust the difference in transition time from a hit position to a readout end in a single channel. T_0 correction is due to electronics delays such as different cable length and signal transition times in different readout channels.

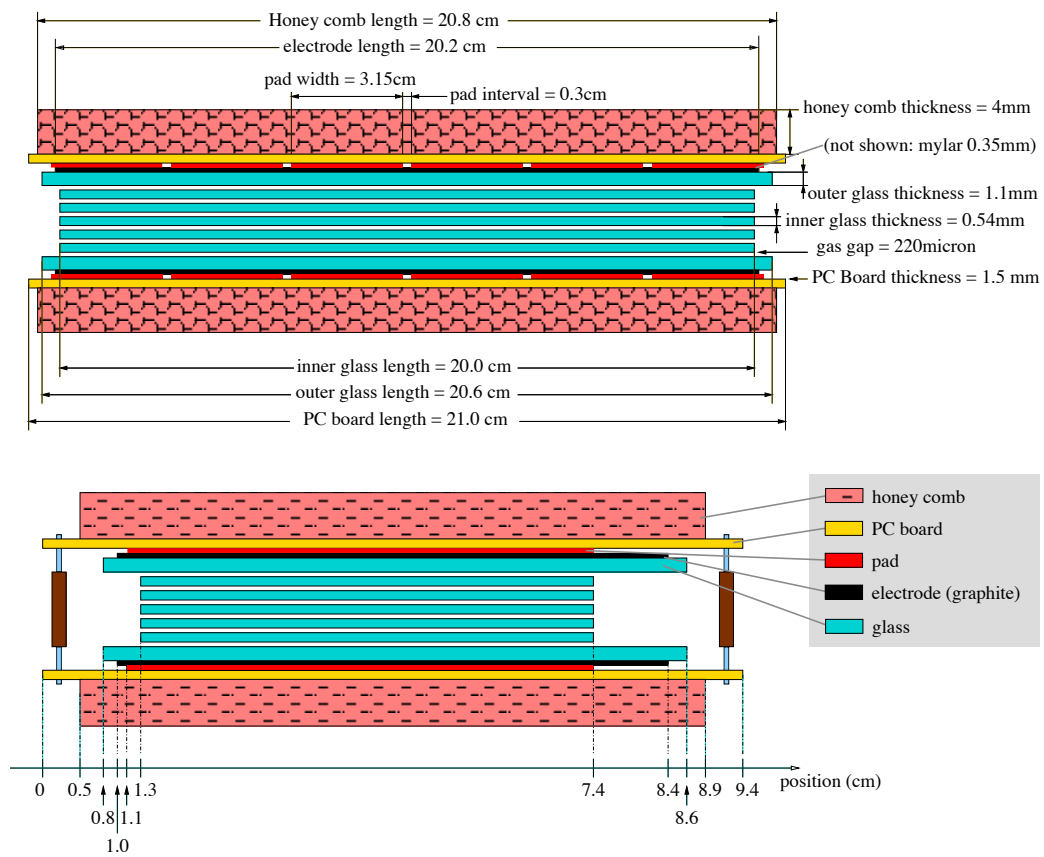


Figure 2.10: MRPC design

Matching

Matching the signals in TOF trays with the tracks from the TPC is an important step in the calculation of the velocity β of the tracks. If a track is mis-matched, the track length would be incorrect and $\beta = v/c = L/ct$, where L is the track length and t is the TOF value, would be wrong. In this section, the matching procedure is reviewed and summarized in order to serve as a reference for others who want a basic understanding of the procedure including cuts or criteria without investigating the actual code (StBTofMatchMaker).

The matching is done on an event-by-event basis and starts with analyzing all TOF hits and global tracks in an event.

1. The global tracks are projected onto the STAR geometry, and extrapolated to the location of the TOF modules and channels, and linked with all possible cells (channels) that the tracks would pass through. To proceed to the next step the tracks are required to pass minimum track quality cuts, $0 < flag < 1000$, $nFitPoints \geq 15$, and $nFitPoints/nHitsPoss \geq 0.52$ where *flag* indicates the fit quality of the track, *nFitPoints* is the number of points used in the track fit, and *nHitsPoss* is the number of possible points in the TPC for the track.
2. TOF hits are then associated with the cells from the previous step, but only if the TOF hit is in a cell that is ± 1 away in the same module. One TOF hit can be associated with multiple tracks, however, in the current scheme those TOF hits are discarded and only TOF hits associated with

a single track are kept. This method could be improved in the future. The possible situation where one track is associated with multiple TOF hits is described in the next section.

3. If one track is associated with only one TOF hit, the TOF information is stored in `StMuBTofPidTraits` of the track with *MatchingFlag* = 1. If one track is associated with multiple TOF hits, the TOF hit with the largest time over threshold (ToT) is selected and stored with *MatchingFlag* = 2. If the two ToTs are the same value, the TOF hit in the nearest cell from the track projection point is stored and set *MatchingFlag* = 3.

This current matching procedure is relatively simple and the matching efficiency (including acceptance) is about 60 – 70% at $p > 0.5$ GeV/ c . If a more sophisticated method is necessary to reduce background and increase matching efficiency, re-matching is recommended using PID information from other measurements, for instance, dE/dx and momentum.

2.3.4 Trigger and Data Acquisition (DAQ)

Triggering systems are very important in high energy particle and nuclear physics experiments like the LHC and RHIC to efficiently find small cross section signals from a huge number of events. The main STAR trigger detectors for heavy ion collisions were the Zero Degree Calorimeters (ZDC) [38] and the Central Trigger Barrel (CTB), which was removed in 2008 to yield space

to the TOF trays. The two ZDCs are located at $z = \pm 18.25$ meters away from the intersection point along the beam axis. Right before each ZDC, there are dipole magnets which bend incoming and outgoing beams for collision. The ZDCs measure the energy of spectator (dissociated) neutrons from collisions. The CTB measured charged particle multiplicity within $\eta = \pm 1$ with full azimuthal coverage. It consisted of 240 scintillators coupled to PMTs and was located at the same place the TOF trays occupy currently. Since 2009 the upVPD was used to trigger the minimum-bias (MB) events that is defined as a coincidence signal in the east and west upVPD detectors.

The data acquisition system (DAQ) has been upgraded to take data at rates up to 1000 Hz since 2008. This is ten times faster than previous rates. Owing to this upgrade and the impressive RHIC luminosity increase, as presented in Figure 2.11, the STAR experiment successfully collected large amounts of data that is necessary for statistically eager analysis like the resonance analysis in this dissertaion.

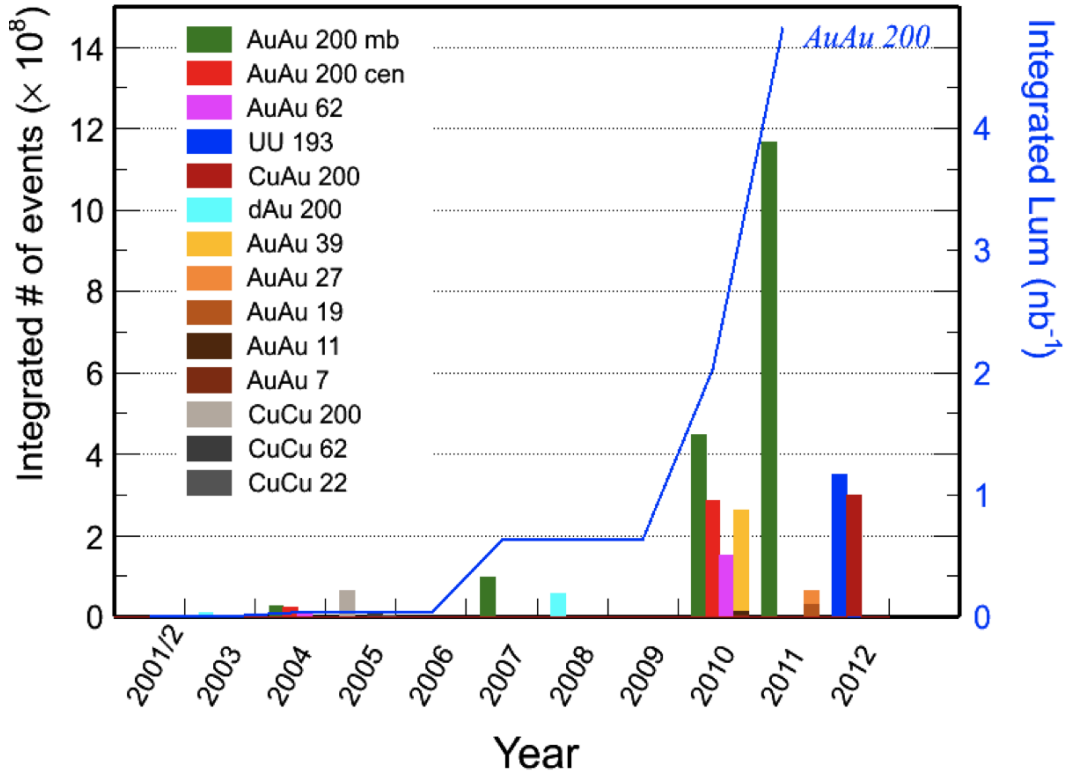


Figure 2.11: Recorded events at STAR

Chapter 3

Particle Identification

3.1 Introduction

Particle Identification (PID) is a procedure through which observed particle species are determined in high-energy physics experiments. PID provides important information, such as spin, mass, and quark contents. The identification of stable particles is performed by exploiting differences of their interactions with detectors or by determining their mass, or a combination of both. In this chapter general PID concepts and methods are discussed. The actual PID method implemented in this analysis is explained in Section 4.3 in detail using concepts explained in this chapter.

3.1.1 PID by difference of interaction with detectors

Different types of particles feel different forces because of their charge difference. For example, particles with an electric charge can interact via electromagnetic force. Therefore the interaction difference can be used as a particle identification method. Figure 3.1 shows typical layers of detectors in high energy physics experiments and how particles interact differently depending mostly on their particle classification, i.e., photon, leptons, and hadrons. As the distance increases from the collision point, the detectors usually be-

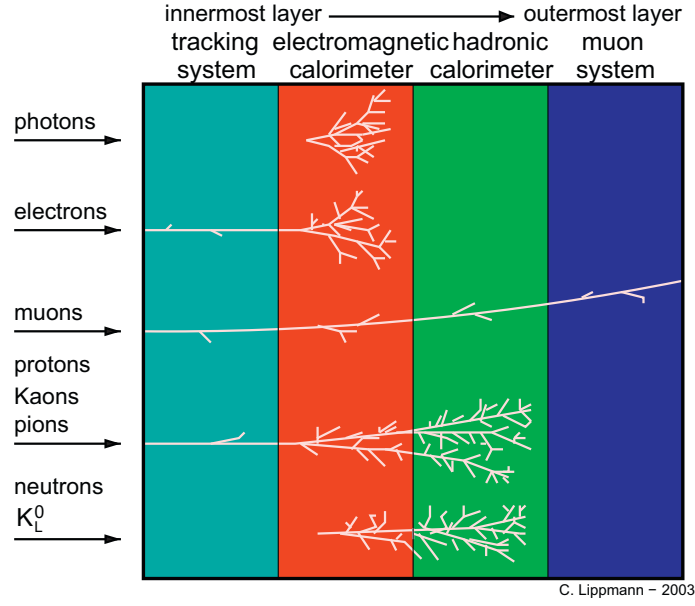


Figure 3.1: Particle penetration power in detectors [39]

come larger and denser, except in the case of the muon system. In the STAR experiment there is no hadronic calorimeter. Instead, the STAR magnet serves as a separator for muons from other particles.

The difference in the interactions of the various particle types will be explained next. The fact that electrons have electric charge makes them different from photons in the tracking detectors. Muons differ from the electrons only by their mass, in which the muon is about 200 times larger. Since the stopping power, which is related to the energy loss, depends on velocity, $\beta\gamma$ and not momentum, $m\beta\gamma$ as shown in Figure 3.2, an electron and muon with the same momentum can have velocities which are different by two orders of magnitude. Therefore the energy loss of an electron and muon are different:

electrons lose their energy via radiative shower, while muons are in the minimum ionization region. This explains the signal difference of electrons and muons in the electromagnetic calorimeter. While pions and muons have similar masses, the absence of the strong interaction in muons makes their interaction in the hadronic calorimeter different.

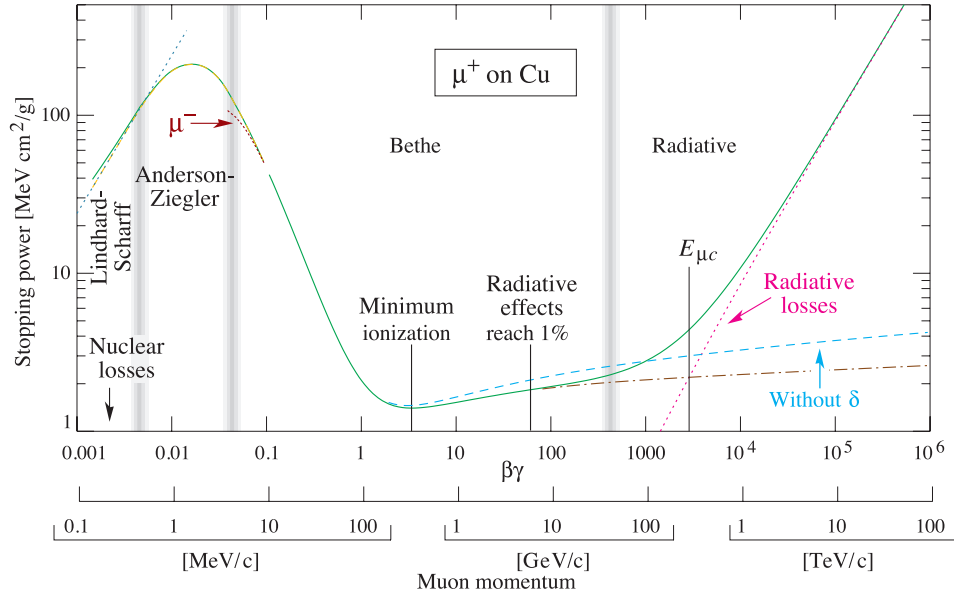


Figure 3.2: Muon stopping power in copper vs. velocity [10]

3.1.2 PID by determining mass

The three most abundant charged hadrons in relativistic heavy ion collisions are pions, kaons, and protons (and their antiparticles). Since their interactions with detectors are similar as shown in Figure 3.1 and they are stable particles, they cannot be separated either based on the interaction dif-

ference or by decay kinematics. However, their identification is crucial, for example, in the resonance study of $\phi \rightarrow K^+ + K^-$ and $\Lambda(1520) \rightarrow p + K$. Particle identified spectra of those particles can also reveal freeze-out parameters, such as the kinematic and chemical freeze-out temperatures and the collective flow velocity, of the hot and dense medium created in heavy ion collisions.

To identify stable particles, it is necessary to determine their charge and mass. The charge sign can be measured from the direction the track curves in a magnetic field and the charge number is obtained from energy loss in the gas dE/dx . Because the mass cannot be directly measured, it has to be extracted from other observables, namely momentum p , velocity β , and energy E . Mass can be calculated via $m^2 = E^2 - p^2$ where the energy is measured in calorimeters in general. There is an Electromagnetic Calorimeter (EMC) detector in STAR, and it is used in analyses that require PID at high momentum, $p > 3 \text{ GeV}/c$. In this dissertation, mass measurements are made from p and β , which are related by $p = \gamma\beta m$ or $m = p/\gamma\beta$.

While the momentum can be (directly) determined only from the curvature of tracks, the particle velocity is accessible by measuring one of the following four observables: dE/dx , time of flight, Cherenkov radiation, and transition radiation. In the STAR experiment, the first two measurements, dE/dx and TOF, are available and each requires a dedicated detector.

dE/dx represents the amount of ionization energy loss of a moving particle per unit length in a gas. As a particle travels through a gas, it loses energy due to collisions with the gas. Since the amount of energy loss depends only on

the particle's velocity (and charge number, z) as shown in Figure 3.3, the energy loss value (dE/dx) provides velocity information. So, if two particles have the same momentum but different masses, they have different velocities and, therefore, different dE/dx values. For this reason, there are several bands in the dE/dx vs. momentum plot corresponding to the each mass of the particle. With the **TOF** measurement, on the other hand, velocity is directly measured

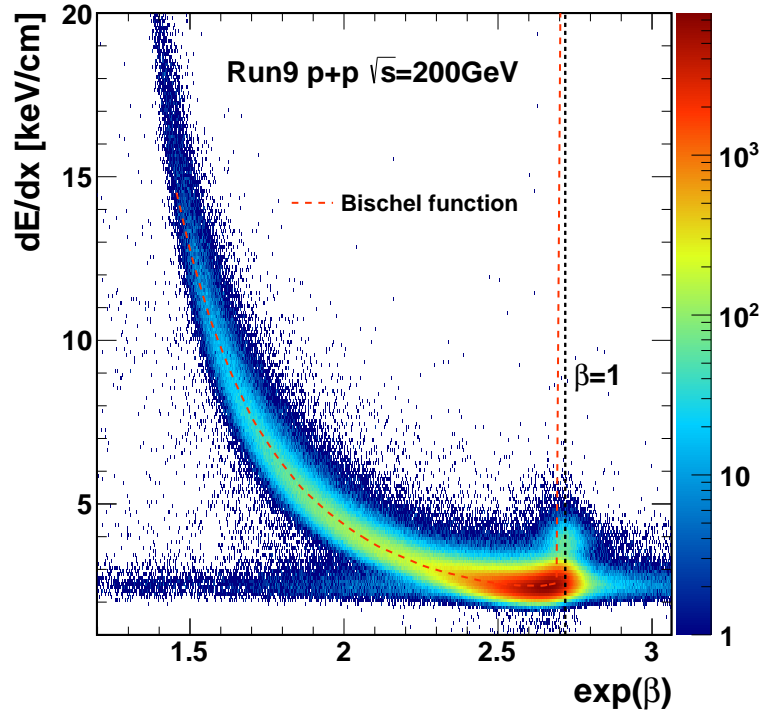


Figure 3.3: dE/dx vs. $\exp(\beta)$ for all particle species [Run9 p+p data]: The red dashed line shows expected dE/dx value (the Bischel Function) for the STAR TPC. The black dashed line is $\beta=1$ limit.

and compared with momentum to obtain a particle's mass. The fact that dE/dx and TOF depend differently on β provides more separation between

particle distributions when both measurements are used simultaneously. TOF has significant separation power at low momentum. While, dE/dx has good separation power at high momentum due to the relativistic rise.

The rest of this chapter discusses details associated with various PID techniques. The actual PID method used in this dissertation is discussed in Section 4.3 in the Analysis chapter below.

3.2 Choice of PID Methods

Choosing a method of PID is highly dependent on the purpose of the identification. For example, track-wise identification is not necessary in the spectra analysis of stable particles, for which yield information in each p_T bin is enough. In this case, even if the separation is not good enough to identify single particles, the yields (amplitudes) can be extracted from the fit procedure in satisfiable precisions. Conversely in resonance analyses, track-wise identification is necessary to reconstruct the parent's invariant mass. This requires many additional considerations such as a cut efficiency correction (see Section 3.6), which is necessary to obtain total yield of the particles. The method to calculate the correction also needs to be considered. Additionally, a balance needs to be found between the purity and efficiency of the identification. For example, in resonance analyses, a tighter cut (more purity) suppresses background, but also decreases the reconstructed signal due to lower PID efficiency. If a simpler method provides sufficient separation for a particular purpose, adding more observables and/or using more sophisticated methods is

not advantageous because it can increase systematical uncertainties and not increase the efficiency and purity significantly.

3.2.1 Separation Power

To quantify the PID capability of an observable, the separation power can be used. It shows the amount of separation between two particle distributions in terms of their standard deviations.

$$s_{i,j} \equiv \frac{\text{separation}}{\text{resolution}} = \frac{|\mu_i - \mu_j|}{\sqrt{\sigma_i^2 + \sigma_j^2}} \quad (3.1)$$

where μ_i is the mean value of a distribution for a particle species i in the observable and σ_i is the standard deviation of the distribution. It is important to note that the separation power only tells how separated two distributions are and it does not indicate the level of contamination. For example, even if pions and electrons are well separated, pions contaminate the electron sample significantly due to the large pion abundance.

When more than one independent (orthogonal) detector measurement, in our case dE/dx and TOF, is available, more separation power can be gained by adding the additional dimensions (Figure 3.4a),

$$s_{i,j}^{Total} \equiv \sqrt{(s_{i,j}^{TPC})^2 + (s_{i,j}^{TOF})^2}. \quad (3.2)$$

In Figure 3.4b the separation powers between kaons and other particles (pions and protons) are calculated from actual data. The dashed lines at the bottom are the separation power from dE/dx only and show small separation powers

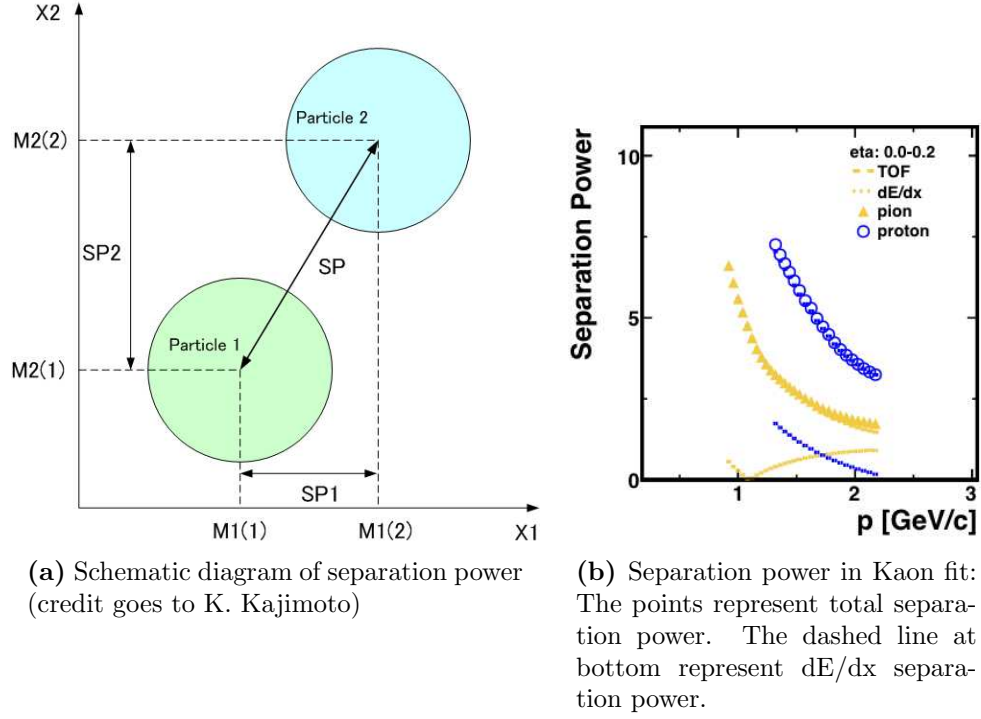


Figure 3.4: 2D separation power

at this momentum range. Adding TOF measurements significantly improve the separation as shown in the points which represent the total separation powers in the figure. Since adding another measurement also adds another source of inefficiency and systematical uncertainties, benefit of the separation power gain should be compared to any down-side effects.

3.2.2 Separation Method

There are two main methods to separate particles track-wise. One is to only consider the distribution of the particles that we want to select using a $n\sigma$ cut. The other one is to take into account other particle distributions

using a probability cut. Either or both of them can be applied depending on situations.

3.2.2.1 $n\sigma$ Method

In general, due to a finite resolution of measurements, measured values form a distribution around their expected (mean) value. The distance of a measured value from the mean is related to a probability. Usually the distance from the mean is normalized by the standard deviation σ called $n\sigma$. $n\sigma$ of a variable X for a particle species *part* is defined as

$$n\sigma_X^{part} = \frac{X - \mu_X^{part}}{\sigma_X^{part}} \quad (3.3)$$

where μ_X^{part} and σ_X^{part} are the mean and standard deviation of X respectively. If there are more than one particle species, since $n\sigma$ can be defined for each particle species and each particle's distribution has different mean and σ , the particle species has to be specified when $n\sigma$ is defined. $n\sigma$ does not require information about other particle's distributions.

For a Gaussian distribution, the probability that a measured value will fall within $\pm\delta$ of the expected value is

$$P(\delta) = \frac{1}{\sqrt{2\pi}\sigma} \int_{\mu-\delta}^{\mu+\delta} e^{-(X-\mu)^2/2\sigma^2} dX = \text{erf}\left(\frac{\delta}{\sqrt{2}\sigma}\right). \quad (3.4)$$

If the distributions of particles are well separated or the analysis is not very sensitive to contaminations from other particles, a selection based on $n\sigma$ values is good enough to separate particles. Then, the PID cut efficiency can be

analytically calculated from Equation 3.4 without computational methods, like the Monte Carlo method.

3.2.2.2 Probability Method

However, if all of the information (amplitude, mean and sigma) about the distributions of other particle species is available, the probability of being each particle species can be obtained. The probability is defined below

$$P^{part}(X) \equiv \frac{N^{part} \times PDF^{part}(X; \mu^{part}, \sigma^{part})}{\sum_i N^i \times PDF^i(X; \mu^i, \sigma^i)} \quad (3.5)$$

where i runs over all relevant particle species including the particle we want to select. N^i is the fraction of yield of the particle i ($\sum_i N^i = 1$). The $PDF^i(X; \mu^i, \sigma^i)$ is the probability density function of X for the particle i , which is characterized by parameters, μ^i and σ^i . Once a cut (selection) range of the variable X is defined by requiring the probability to be bigger than some value, the cut efficiency (see Section 3.6) can be calculated by integrating the PDF^{part} over the cut range. It is usually difficult to calculate this integration analytically due to a complicated shape of the cut range, so the Monte Carlo method is used. The details are discussed with real data in Section 4.3 in the Analysis chapter. This probability method is very useful to separate particles while controlling contaminations when the particle distributions are close to each other.

3.3 Choice of Distributions

To apply both $n\sigma$ and probability methods, it is convenient to describe particle distributions in terms of analytical functions, like the Gaussian and Student's T distributions. The particle distribution can also be described by, so called, an expected distribution, which is derived from data and, therefore, reflects all detector resolutions and inefficiencies. The expected distribution is favorable when a suitable analytical distribution is not found to describe the particle distribution. Before choosing a distribution, a (test) ***statistic***, a form of observable (such as m^2 and $1/\beta$), has to be chosen because it affects the shape of particle distributions. For example, if a distribution of m is the Gaussian shape, a distribution of m^2 would not be the Gaussian shape. This choice of statistic affects only shape of distributions but not affects the separation power of the observable. The separation power of one observable would not be changed by changing the form of the observable. Since the choice of distributions depends on each statistic of the measurement, the dE/dx and TOF distributions are discussed separately.

3.3.1 PID with dE/dx

In the STAR experiment, while the expected (mean) dE/dx value of tracks can be obtained by the Bichsel function [40] which is a function of β , the actual dE/dx value of a track is measured from energy deposits along the track. Since the values of the energy deposits follow a Landau distribution with a long tail to the high energy side, the most probable dE/dx value of the

track is approximated by the truncated mean from only the lowest 70% energy deposits in order to reduce the influence of the high energy deposits in the tail. Those truncated means also have statistical track-wise fluctuations and the distribution is quite well approximated by the log-normal distribution. For this reason, if $\log(dE/dx)$ is used as a statistic, the result distribution follows the Gaussian distribution. It is convenient to define the normalized version of this statistic as follows,

$$n\sigma_{dE/dx}^{part} = \frac{\log(dE/dx) - \log(dE/dx_{exp})^{part}}{\sigma_{\log(dE/dx)}}, \quad (3.6)$$

where $\log(dE/dx_{exp})^{part}$ is the log of the expected value from the Bichsel function with particle mass assumption. $\log(dE/dx)$ is calculated from data and the resolution ($\sigma_{\log(dE/dx)}$) depends on the number of fit points used in the helix fit. If the calibration of the dE/dx value is ideal, this statistic for the particle has a Gaussian distribution with mean 0 and sigma 1. For this reason the Gaussian distribution is used to fit and describe the particle distributions for $n\sigma_{dE/dx}^{part}$.

As you can see from Figure 3.5, dE/dx can be used for PID at low momentum ($p < 1\text{GeV}/c$), while it can not be used at intermediate momentum since the lines start merge. This is the region where TOF improves the PID capability by a great amount as shown in Figure 3.6.

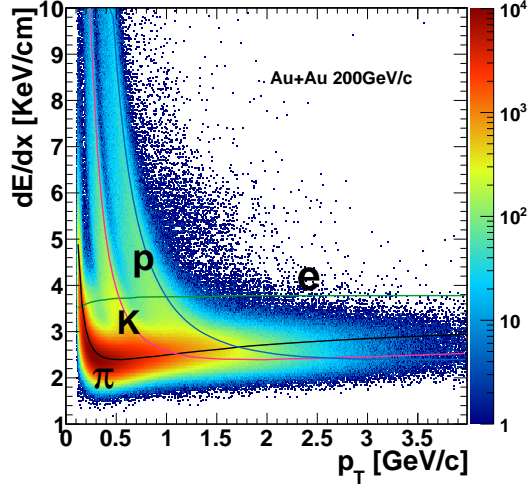


Figure 3.5: Energy Loss in gas per unit length vs. momentum

3.3.2 PID with TOF

The expected value of the particle velocity is calculated with a given momentum and mass assumption as

$$\beta^{part} = \frac{1}{\sqrt{1 + m_{part}^2/p^2}}. \quad (3.7)$$

The velocity measurement is done from TOF and track length,

$$\beta = \frac{v}{c} = \frac{L}{ct} \quad (3.8)$$

where t is from the TOF system, *i.e.*, $t \equiv t_{stop} - t_{start}$ and L is from tracking in the TPC.

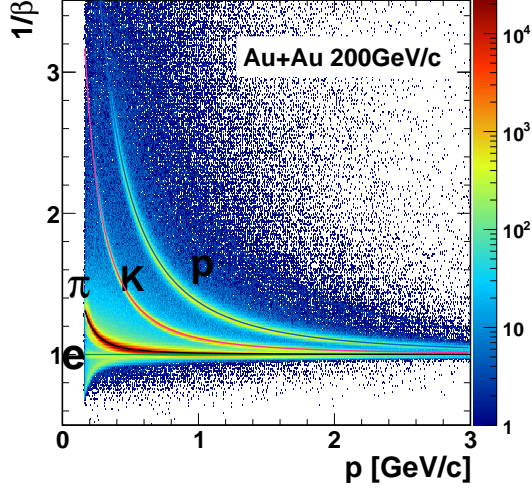


Figure 3.6: $1/\beta$ v.s. momentum

3.3.2.1 Statistic (form of observable)

There are several choices of statistic for TOF each with their own pros and cons depending on the situation. Three statistics, m^2 , $\Delta\beta^{-1}/\beta^{-1}$, and $\Delta\beta^{-2}$, are shown. We choose $\Delta\beta^{-1}/\beta^{-1}$ for this analysis based on its behavior at high momentum.

m^2 The most intuitive choice of statistic would be m^2 , which is calculated from p , t , and L as follows,

$$m^2 = \frac{p^2}{\gamma^2 \beta^2} = p^2 \left(\frac{c^2 t^2}{L^2} - 1 \right) \quad (3.9)$$

The reason that m^2 is used instead of m is because m^2 could be a negative value due to the resolution of the measurements as shown in Figure 3.7a. In that case $m = \sqrt{m^2}$ is an imaginary number and can not be defined. To avoid

this undefined value of statistic, a statistic must have continuity at $\beta = 1$ as shown in Table 3.1. For example, since γ^2 has discontinuity at $\beta = 1$, it is not used as a statistic.

β	0	1_-	1_+	∞
γ^2	1	$+\infty$	$-\infty$	0
$1/\gamma^2\beta^2$	∞	0_+	0_-	-1
$1/\beta$	∞	1_-	1_+	0

Table 3.1: Continuity of statistic

The resolution of m^2 is obtained by error propagation as

$$\left(\frac{\delta m^2}{m^2}\right)^2 = 4 \left[\left(\frac{\delta p^{-1}}{p^{-1}}\right)^2 + \gamma^4 \left\{ \left(\frac{\delta t}{t}\right)^2 + \left(\frac{\delta L}{L}\right)^2 \right\} \right]. \quad (3.10)$$

Due to the γ factor in front of the time and length terms, the resolution considerably increases as momentum becomes higher while the expectation value (mass) is constant. The actual distributions of m^2 in p+p collisions at $\sqrt{s_{NN}} = 200$ GeV in Run 8 are presented in Figure 3.7a. Figure 3.7b shows an example of a fit with Gaussian functions, which fail to describe the tails of the particle distributions. The advantage of using m^2 as a statistic in PID is that the expectation values are constant without any mass assumption, thus it is possible to fit all particles, e, μ, π, K , and p , together over the wide momentum range. This m^2 is also convenient when one wants to study p_T distribution of the stable particles directly from the fit, although the resulting distribution in each p_T bin becomes more non-Gaussian due to the fact that the resolution depends on p , not p_T .

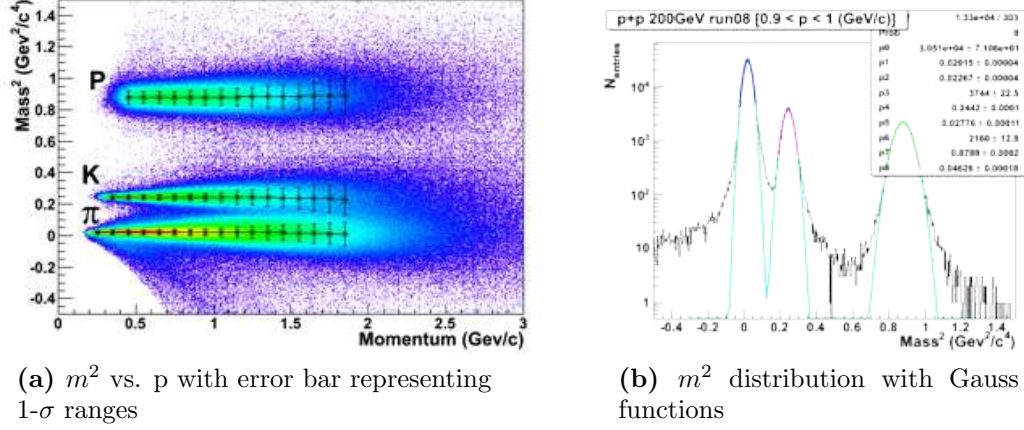


Figure 3.7: m^2 distributions (p+p 200 GeV Run8)

$\Delta\beta^{-1}/\beta^{-1}$ This statistic is found to have constant resolution at high momentum and a more Gaussian like distribution than m^2 (see Figure 3.8b). It is defined as

$$\frac{\Delta\beta_{part}^{-1}}{\beta^{-1}} = \frac{\beta_{TOF}^{-1} - \beta_{TPC}^{-1}}{\beta_{TOF}^{-1}} = 1 - \frac{L}{ct} \sqrt{1 - \frac{m_{part}^2}{p^2}} \quad (3.11)$$

where m_{part}^2 is the mass of the particle we want to select. The expectation value for the particle, $part$, is 0 by definition. The resolution dependency is

$$\delta \left(\frac{\Delta\beta^{-1}}{\beta^{-1}} \right)^2 = \gamma^{-4} \left(\frac{\delta p^{-1}}{p^{-1}} \right)^2 + \left(\frac{\delta t}{t} \right)^2 + \left(\frac{\delta L}{L} \right)^2. \quad (3.12)$$

The actual distribution with a pion mass assumption is presented in Figure 3.8a. Because of the γ^{-1} factor in the resolution, this $\Delta\beta^{-1}/\beta^{-1}$ has nearly constant resolution at high momentum. In the high momentum region, due to low multiplicity of particles, the particles need to be integrated over a wide momentum range in order to perform a well constrained fit. This

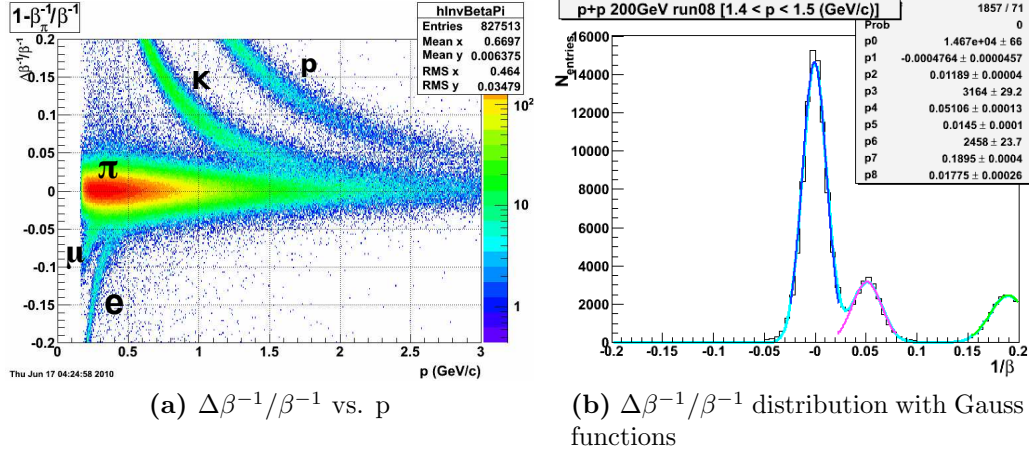


Figure 3.8: $\Delta\beta^{-1}/\beta^{-1}$ distributions (p+p 200 GeV Run 8)

constant resolution of $\Delta\beta^{-1}/\beta^{-1}$ helps to extract the distribution's width with smaller errors and bin size effects compared to the m^2 statistic. This is the reason that $\Delta\beta^{-1}/\beta^{-1}$ is chosen in this study. This constant resolution at high momentum is also important when extrapolated parameters are employed at a higher momentum range, $p > 3$ GeV/c, where clear separation is usually difficult and hence obtaining the parameters by fitting is also difficult. The disadvantage of $\Delta\beta^{-1}/\beta^{-1}$ statistic is that each particle distribution has to be fitted separately since mass assumption is necessary.

$\Delta\beta^{-2}$ This statistic is constructed to have its expectation (mean) value to be a linear function of p^{-2} . So, it is possible to estimate the amount of width broadening due to mean variation within a momentum bin. By subtracting the contribution of the mean variation from the fit width, we could obtain the width including only detector resolutions. Since narrower width means more

separation power, a more efficient PID is possible. This statistic is calculated by

$$\Delta\beta_{part}^{-2} = \beta_{TOF}^{-2} - \beta_{TPC}^{-2} = \left(\frac{ct}{L}\right)^2 + \frac{m_{part}^2}{p^2} - 1 \quad (3.13)$$

and its resolution dependency is

$$\delta(\Delta\beta^{-2})^2 = 4\beta^{-2} \left[\gamma^{-2} \left(\frac{\delta p^{-1}}{p^{-1}} \right)^2 + \left(\frac{\delta t}{t} \right)^2 + \left(\frac{\delta L}{L} \right)^2 \right]. \quad (3.14)$$

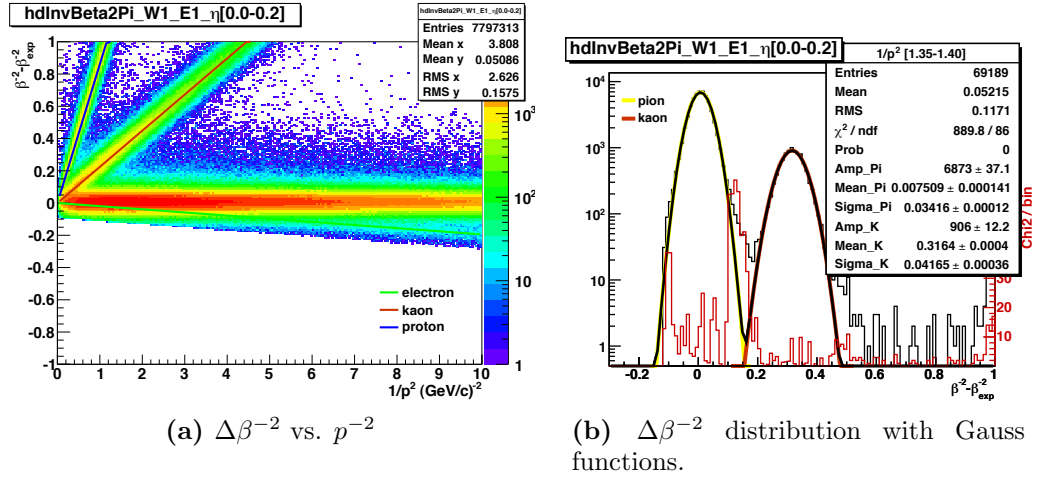


Figure 3.9: $\Delta\beta^{-2}$ distributions (p+p 200 GeV Run9)

The actual distributions of $\Delta\beta^{-2}$ with a pion mass assumption in p+p collision at $\sqrt{s_{NN}} = 200$ GeV in Run 9 are presented in Figure 3.9a. Since the track momentum resolution depends on p_T^{-1} , the width of this distribution might be parametrized as a function of p_T^{-1} and it could be extended to high momentum (small p^{-2}). Additionally, high momentum tracks are all in a small region at low p^{-2} so there is enough entries to fit the distributions. The disadvantage of this statistic is using p^{-2} . Usually, observables (like particle's

yields) are plotted as functions of p or p_T . The obtained observables from the fit need to be converted to the functions of p or p_T to be compared to other results.

3.3.2.2 Fit Function (Distribution)

Since the accuracy of PID depends on how well a distribution of the chosen statistic is described, it is important to find an appropriate function form (PDF) for the statistic. Usually, the Gaussian function is used because of its well defined mean and sigma, and the fact that the Gaussian function is implemented in many software programs. While the $\Delta\beta^{-1}/\beta^{-1}$ statistic can be described with the Gaussian function in p+p collisions, in Au+Au collisions there is long tail due to fluctuations in the number of start side detectors (upVPDs). The tail cannot be fit by a Gaussian function as shown in the plot in the left panel of Figure 3.10. It is found that a student's T function can better describe $\Delta\beta^{-1}/\beta^{-1}$ as shown in the right panel of Figure 3.10. The student's T function is defined as

$$p(x; \mu, \lambda, \nu) \equiv B^{-1} \left(\frac{1}{2}, \frac{\nu}{2} \right) \sqrt{\frac{\lambda}{\nu}} \left(1 + \frac{\lambda(x - \mu)^2}{\nu} \right)^{-\frac{\nu+1}{2}} \quad (3.15)$$

For the details of the Student's T distribution, see Appendix A.1.

Expected function Another way to describe the particle distributions is by using so called *expected functions* which are derived directly from data in a momentum range with good particle separation. Assuming the shape of the distributions are independent of momentum, one can use this expected

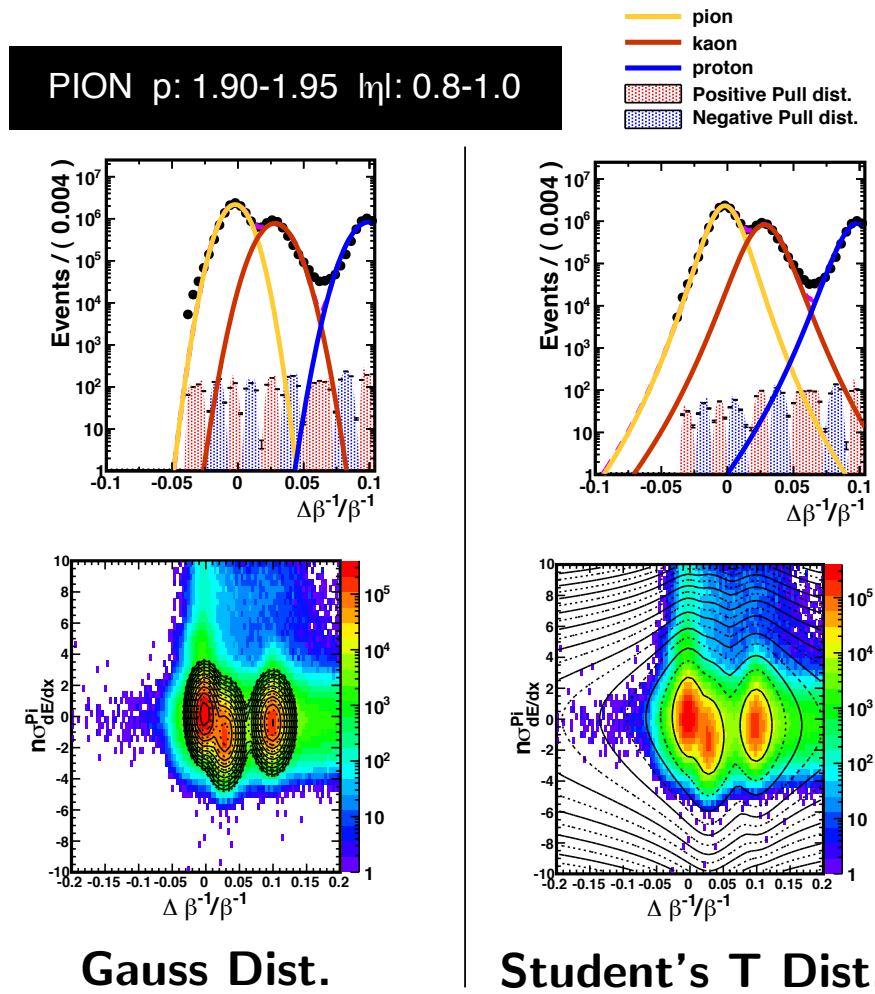


Figure 3.10: Gauss and Student's T distributions. The “Pull” is defined as $(\text{Data-Func.})/\text{Bin error}$.

function to fit particle distributions beyond the well separated momentum range. As an example, the expected function of m^2 is discussed below.

The procedures for obtaining the expected m^2 distribution are as follows. First, to take into account the TOF detector resolution, the distributions

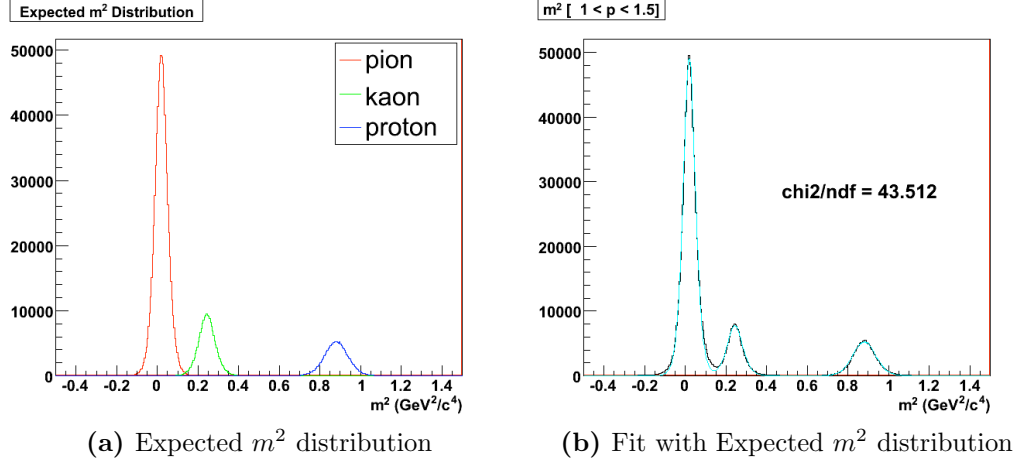


Figure 3.11: Expected m^2 distribution at $1.0 > p > 1.5 \text{ GeV}/c$

of the time difference Δt between the measured and true (expected) times are obtained for each particle species. The Δt distribution is extracted at a well separated momentum range by applying PID selection on dE/dx for each particle species and calculating

$$\Delta t = t_{TOF} - t_{TPC}^{part} = t_{TOF} - \frac{L}{c} \sqrt{1 + m_{part}^2/p^2}. \quad (3.16)$$

Because the Δt distributions are expected to be independent of momentum, the Δt distributions can be used to generate m^2 distributions at any momentum bin by smearing t (according to the Δt distributions) in Equation 3.9, where L is taken from actual tracks within the momentum bin. In Figure 3.11a, one example of the generated m^2 distributions for pions, kaons, and protons is presented. Using those distributions as fit functions, we fit the m^2 spectrum from the real data as in Figure 3.11b by varying positions and amplitudes of the expected functions as fit parameters.

3.4 Combined PID

A simple way to apply PID cuts is based on applying dE/dx and TOF separately [41]. However, using dE/dx and TOF simultaneously maximizes the PID capabilities. This is done by selecting an area in the shape of an ellipse as in Figure 3.12a, or an even more complex shape as in Figure 3.12b. This simultaneously applying two PID cuts can reduce background compared to the PID by applying dE/dx and TOF separately where the selected area is rectangular in shape and it includes more contaminations at corners from other particle distributions.

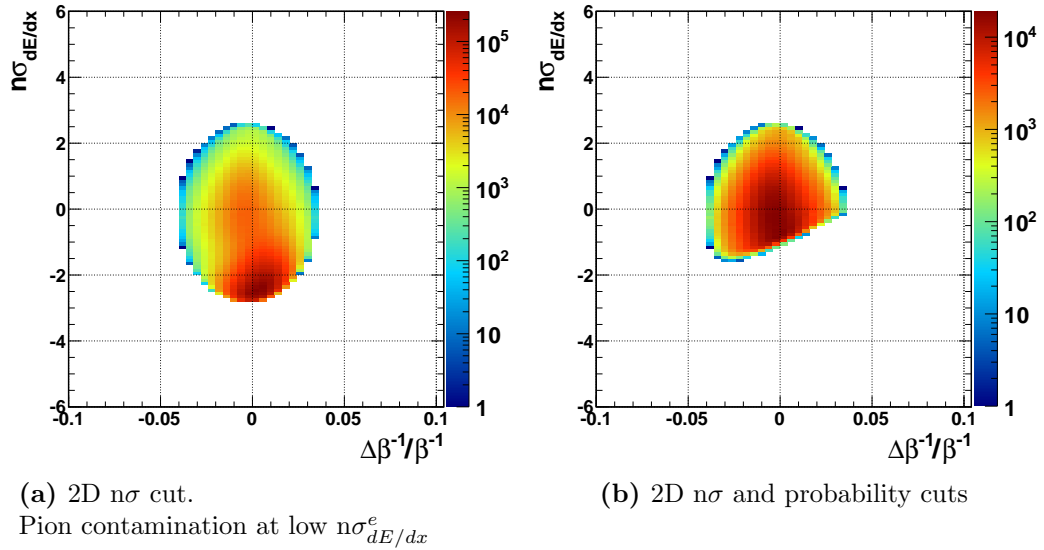


Figure 3.12: Electron identification in 2D at $p=1-1.1$ GeV/ c

3.5 Obtain Distributions by Fit

Usually precise descriptions of particle distributions are obtained via fitting. At low momentum where both dE/dx and TOF have good separation powers, the target particle distribution is fit with a 1-particle function, that describes only one particle species. In the overlap region, 2-particle or 3-particle fit functions are used to achieve better results. A 2D fit is used in this work because more information, *i.e.* fit points, are available to constrain the fit parameters compared to other procedures, where one cuts on one statistic, usually TOF, and fits the other shape, dE/dx , in 1D. One example of 3-particle fitting in 2D is shown in Figure 3.13. An issue with 2D fitting is in its difficulty to control the 2D fit functions because of larger number of fit parameters. Careful constraints have to be made on the fit parameters.

At high momentum it is difficult to fit distributions due to loss of separation power even in 2D. There are several ways to improve fit results by constraining parameters.

3.5.1 Constraint with pure samples

One way is by selecting a clean region, where the contaminations from other particles are small, in one variable and fitting the sampled distribution in the other variable (1D Fit). Another way is by obtaining decay daughters from unstable particles by topological cuts and an invariant mass cut, and then fit the daughters' distribution in 2D. This method is possible only if there are enough statistics to reconstruct decay particles. This method is discussed in

PION p: 1.95-2.00 $|\eta|$: 0.0-0.2

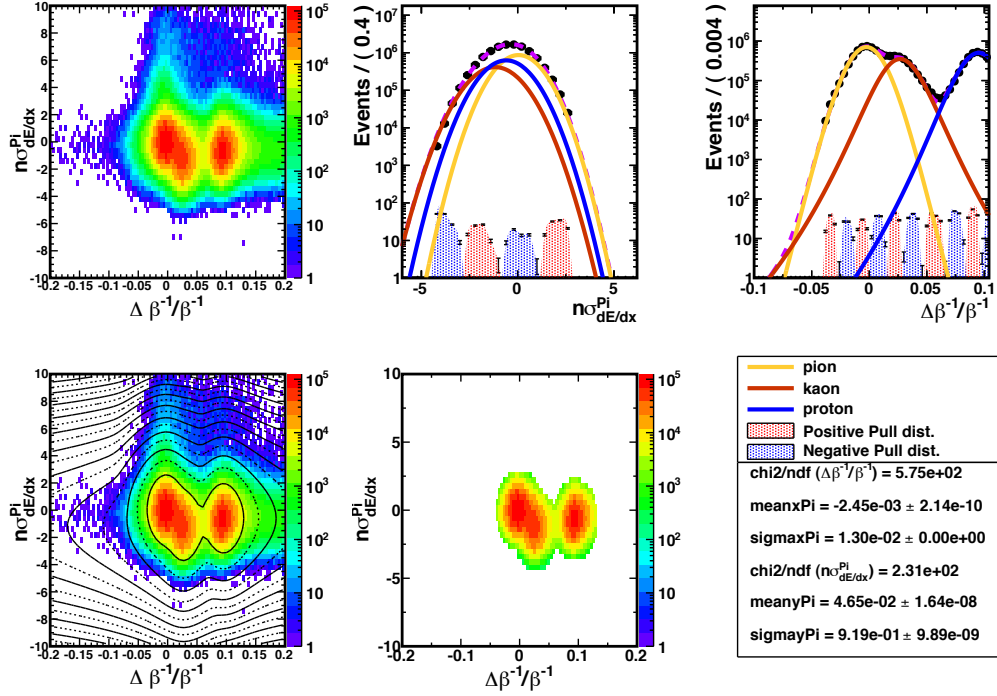


Figure 3.13: Pion fit example. The Gauss and Student's T function are used for dE/dx and $\Delta\beta^{-1}/\beta^{-1}$, respectively.

details in Section 4.3.2 in the Analysis chapter.

3.5.2 Constraint by parameter behavior

In some cases, a parameter can be fixed to another parameter by physical reasons. For example, merged pions are two pion tracks close to each other (mostly decayed daughters from γ) which are mistakenly reconstructed as one pion track due to lack of spacial resolution in the TPC. Since those merged

pion tracks are pions, merged pions are expected to have the same mean value of $\Delta\beta^{-1}/\beta^{-1}$ as the mean value of pion distribution, but the σ of $\Delta\beta^{-1}/\beta^{-1}$ might be different from a regular pion distribution. Also, the mean dE/dx of merged pions is expected to be twice that of the regular pion distribution.

3.6 Efficiency Correction

Often the main interest is in the particle yields and then one needs to know how many particles are lost due to applying PID cuts in order to correct yields. For the $n\sigma$ cut, thanks to the Gaussian distribution, it is easy to calculate the probability for a given $n\sigma$ via Eq. 3.4. For instance, 68% of particles are within 1-sigma distance from the mean. For the probability cut, the situation is more complicated due to the complexity of the selected area. In this case the cut efficiency is calculable using the Monte Carlo method. Tracks are generated according to the particle distributions and then the probability cut is applied to the generated tracks. Then, the efficiency is given by a ratio of the number of tracks which satisfy the cut to the number of the generated tracks. The detailed procedure is elaborated with actual data in Section 4.5.2 in the Analysis chapter.

When choosing a PID method, one has to consider how to calculate its PID efficiency too because it affects the final results. The calculation is sometimes time consuming if a complicated PID method is chosen.

3.7 TOF Resolution

If the parameters of the particle distributions can be parametrized as functions of momentum, tighter constraints are possible and it enable particle identification at even higher momentum.

For example, the dependency of the $\Delta\beta^{-1}/\beta^{-1}$ on measured values, the resolution (σ) of $\Delta\beta^{-1}/\beta^{-1}$ can be written as a function of p with parameters of measurement's resolutions as follows

$$\begin{aligned}\delta\left(\frac{\Delta\beta^{-1}}{\beta^{-1}}\right)^2 &\equiv \delta\left(\frac{\beta_{TOF}^{-1} - \beta_{exp}^{-1}}{\beta_{TOF}^{-1}}\right)^2 \\ &= \left(\frac{\delta t}{t}\right)^2 + \left[\frac{D_T}{l_T} \left[1 - \left(\frac{0.3BD_T}{2p_T}\right)^2\right]^{-1/2} - 1 + \gamma_{exp}^{-2}\right]^2 \left(\frac{\delta p_T^{-1}}{p_T^{-1}}\right)^2 \\ &\quad + (1 + \gamma_{exp}^{-2})^2 (\tanh\eta \delta\eta)^2\end{aligned}$$

where $\left(\frac{\delta p_T^{-1}}{p_T^{-1}}\right)^2 = (C_{SP}^2 p_T^2 + C_{MS}^2 \beta^{-2})$. The detailed derivation is given in Appendix B. The variable t is the time of flight (≈ 10 ns) and δt is its resolution (≈ 120 ps). This resolution includes start side and stop side resolutions. The second term of the equation above is the contributions from the transverse length l_T and transverse momentum p_T measurements. Because both transverse length and momentum are calculated from the curvature of a track, their resolutions are included in the same term. The B is the magnetic field strength (0.5 Tesla) and the D_T is the transverse distance from the collision vertex to the TOF tray (≈ 214 cm). The C_{SP} and C_{MS} are coefficients of special resolution and multi-scattering resolution in the TPC respectively. The third term

is the contribution from the resolution in pseudo-rapidity η . This is a function of p_T and η with given particle mass and the fit parameters: δt , $\delta\eta$, C_{SP} , and C_{MS} .

In Figure 3.14, one example of the parametrization fit is presented with its components. The contribution from the momentum resolution (the orange line) is dominant at low momentum (small γ), and decreases at high momentum due to the γ^{-2} factor. On the other hand, the contribution of the time resolution becomes dominant at high momentum and approaches a constant, which is the same for all particles. The simultaneous fit to

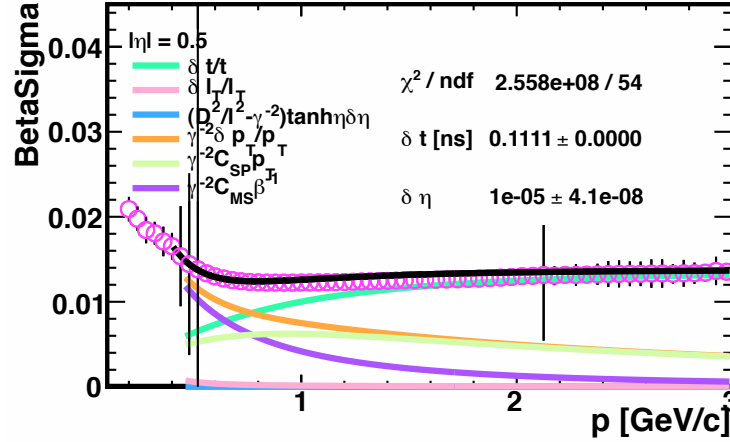


Figure 3.14: $\Delta\beta_p^{-1}/\beta^{-1}$ resolution vs. momentum with components in Au+Au collisions. The C_{SP} and C_{MS} are fixed at 0.015 and 0.0065 respectively

resolutions of three particles is shown in Figure 3.15. The resolutions for kaons and protons are shifted for presentation purpose. Those functions share the same parameter values and the only difference is particle masses in the equation. This might imply the parameterization is valid.

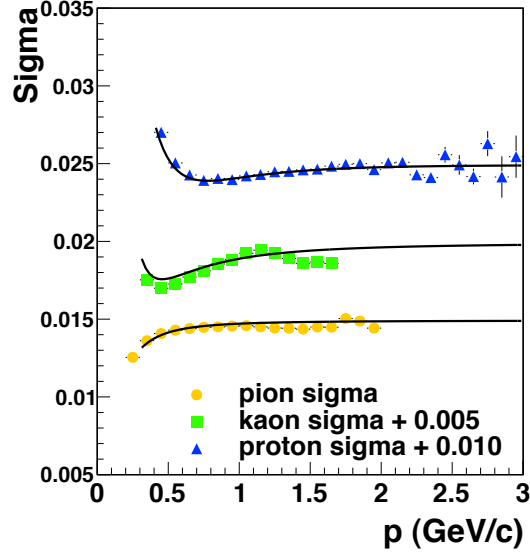
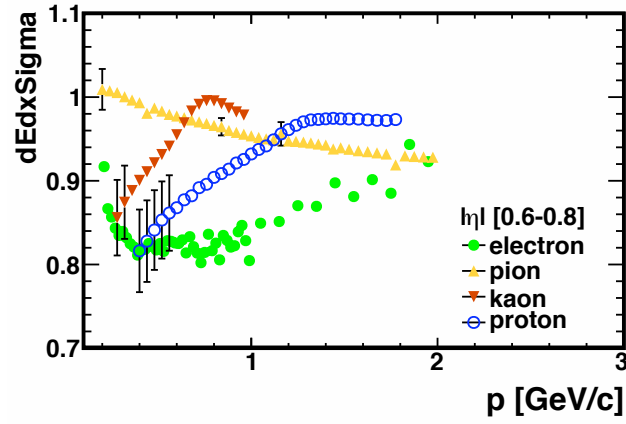


Figure 3.15: $\Delta\beta_p^{-1}/\beta^{-1}$ resolution for π , K, and p with the same parameters in p+p collisions

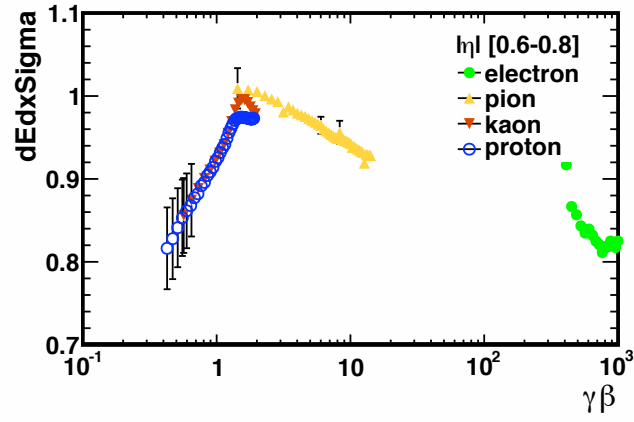
In the current formalism the δt contains the time resolution of the start and stop side detectors. Since the start side time resolution depends on the number of lit upVPDs, the δt might be decomposed further in terms of the number of lit upVPDs. This is left for future study.

3.8 $n\sigma_{dE/dx}$ Resolution

For the $n\sigma_{dE/dx}$ measurement, it is difficult to parameterize its resolution as a function of momentum because it is already normalized by the resolution of $\log(dE/dx)$, which depends on the number of measured dE/dx points in a track. Although the $n\sigma_{dE/dx}$ resolution vs. momentum in Figure 3.16a does not exhibit any trend, the $n\sigma_{dE/dx}$ resolution vs. $\gamma\beta$ manifests



(a) $n\sigma_{dE/dx}$ resolution vs. p



(b) $n\sigma_{dE/dx}$ resolution vs. $\gamma\beta$

Figure 3.16: $n\sigma_{dE/dx}$ resolution for all particles (Au+Au 200 GeV Run10)

some trend. When compared to Figure 3.3, it seems that the higher the dE/dx value, the smaller the resolution. This makes sense because the high dE/dx value means more ionization and a higher number of reconstructable clusters in the TPC, which makes dE/dx measurements more accurate. This is only a hypothesis and needs to be studied.

Chapter 4

$\phi \rightarrow e^+ + e^-$ Analysis

In this chapter, a detailed explanation of the $\phi \rightarrow e^+ + e^-$ analysis is presented. This chapter is organized as follows: In Section 4.1 and 4.2, the data set and the basic event and track selections are presented, while Section 4.3 describes the electron (and positron) identification in detail, which includes the method to obtain the electron distribution from a pure electron sample, and the separation methods in 2D, $n\sigma_{dE/dx}$ and $\Delta\beta^{-1}/\beta^{-1}$. Then, the techniques for reconstruction and extraction of the $\phi \rightarrow e^+ + e^-$ signals are discussed in Section 4.4. This chapter ends with the efficiency correction (Section 4.5) and systematical uncertainty study (Section 4.6) to obtain the final results.

4.1 Data Set

The data presented here was taken in the year 2010 from Au+Au collisions at $\sqrt{s_{NN}} = 200$ GeV with the minimum bias trigger in the STAR experiment at RHIC.

- Trigger: VPD minimum bias trigger, which requires a coincidence on the east and west side upVPDs (trigger ID = 2600[0123]1)

- Production: P10ik (library: SL10k)
- FileCatalog Command: `production=P10ik,filetype=daq_reco_MuDst, trgsetupname=AuAu200_production,filename=~st_physics, storage!=HPSS,tpx=1`
- Number of Events: 350M events (before event cuts), 250M events (after event cuts)

4.1.1 Event Distributions

To characterize events, several event distributions plotted as functions of various variables are checked for quality assurance and shown below. The weighted reference multiplicity (refMult) distributions with two different cuts on the vertex positions along the beam axis V_Z are presented in Figure 4.1a. The refMult is the number of charged primary tracks in a mid rapidity region ($|\eta| \leq 0.5$) in an event and the weighting factors are calculated by the Monte Carlo simulation to take into account the trigger inefficiency. Since different cuts on the difference of V_Z measured by the TPC and upVPD $|V_Z(TPC) - V_Z(VPD)|$ were used in the main analysis and the pure electron sample analysis (explained later in Section 4.3.2), differences are checked. Most of the differences are less than 10% and are in peripheral events, where contributions to the ϕ signals are limited. The difference in the number of events is 1.26% as shown in Figure 4.2b. Figure 4.1b shows the number of lit upVPD used in the start time calculation. There is some structure due to a truncation method to improve the timing resolution by reducing outliers.

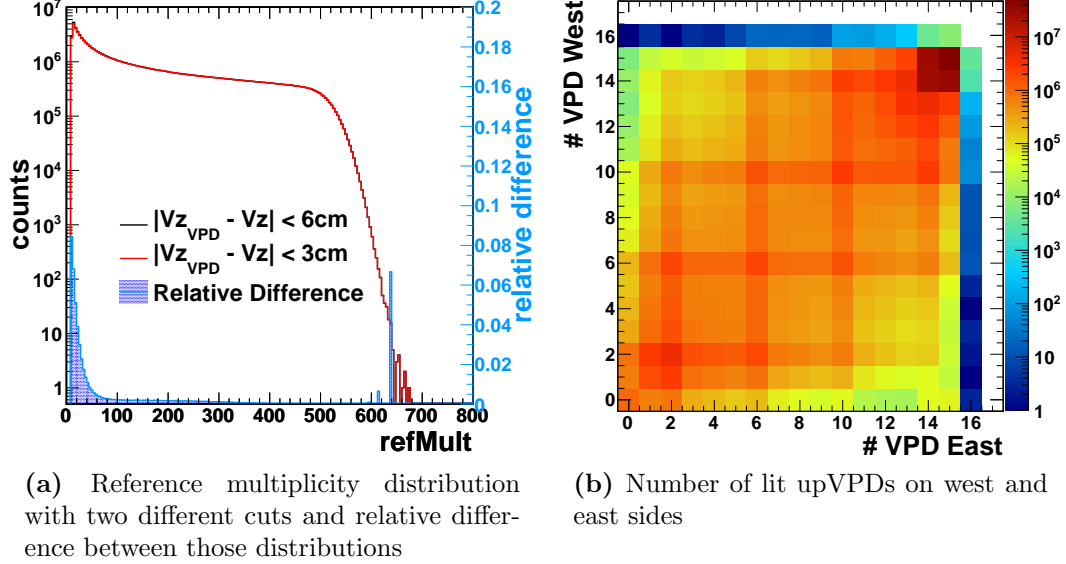


Figure 4.1: Reference multiplicity and upVPD

The position of the primary vertices along the beam axis (V_Z) are shown in Figure 4.2a. The filled area shows the events used in this analysis. The dashed line is the Gaussian function fitted to the data and the fit results are plotted in the middle of the figure. The difference of V_Z from the TPC and upVPD are plotted in Figure 4.2b. The distribution is not Gaussian. This might be a result of the upVPD resolution rather than the TPC resolution since the V_Z value from the TPC is calculated from a larger number of tracks compared to the number of hits in the upVPD (at most 2×19 PMTs). If both resolutions are Gaussian, it would be a Gaussian distribution because the difference (or sum) of normally distributed random variables also has a normal (Gaussian) distribution. The primary vertex positions in 2D are plotted in

Figure 4.3.

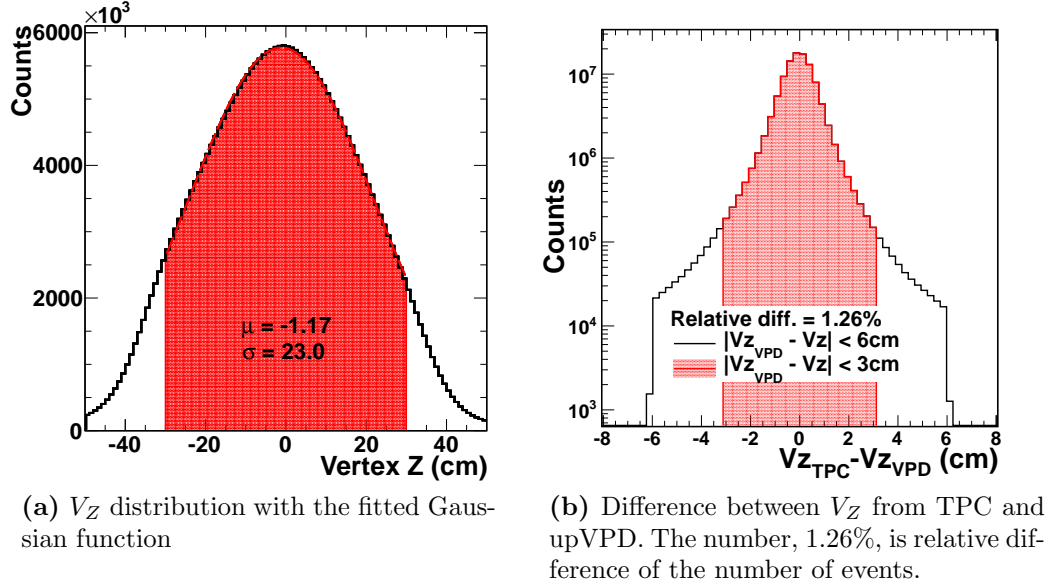


Figure 4.2: Primary vertex position on z axis

4.2 Event & Track Selection

4.2.1 Event Cut

The events are selected with a V_Z within ± 30 cm from the geometric center of the TPC to take full advantage of the symmetric, large acceptance and to minimize geometric bias due to asymmetric acceptances at the edge of the detectors. The deviation of primary vertices from the center (beam center) in the x-y plane, V_r , are required to be less than 2 cm to avoid events at the beam pipe. Since the TOF detector was used, we also required that the difference between the V_Z reconstructed from TPC and upVPD is within

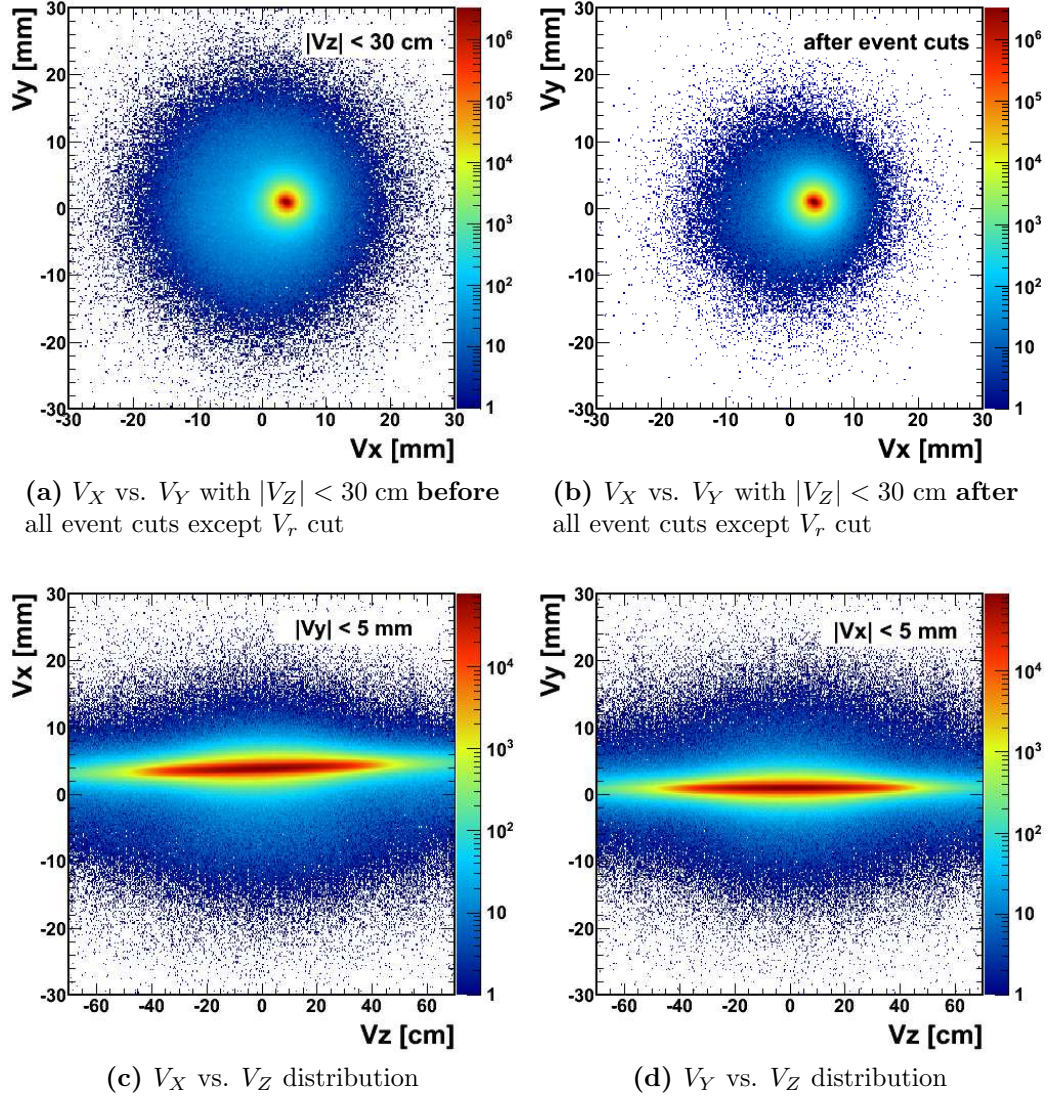


Figure 4.3: Primary vertex position

± 3 cm to ensure the TOF start times are calculated from the same vertices as primary vertices in the events. This cut also serves as an efficient rejection of pile-up events, where two or more separated collisions are reconstructed as

one event. Hits are required in the upVPDs on both the east and west sides to calculate collision times. Since this cut is included in the basic cuts in the TOF reconstruction chain, it might not be needed again at this level. After an additional 0-80% centrality selection based on the refMult value [42], about 250M events are analyzed in this study.

4.2.2 Track Cut

Primary tracks, which have a distance of closest approach (DCA) within 1.1 cm and have at least 22 fit points (nHitsFit) in the TPC, are selected. The DCA cut reduces contaminations from daughter tracks of weak decayed resonances, which typically have decay lengths of several cm, as well as e^\pm tracks from γ conversion at the beam pipe. The requirement on the fit points ensures the tracks have good momentum measurements. Tracks are also required to have the ratio of the nHitsFit to the number of possible points in the TPC (nHitsPoss), which is at most 45 points, be greater than 0.52. With this requirement we can avoid split tracks, one track reconstructed into two tracks. Both track momentum p and transverse momentum p_T have to be bigger than 0.18 GeV/ c to reach TOF trays and there is a maximum momentum limit $p = 2$ GeV/ c due to inefficiency in electron PID. Above this momentum limit, pion contamination is severe. Since TOF is used, track pseudo-rapidity is required to be less than ± 1 .

TOF related track cut The TOF Match Flag selects tracks which are correctly matched with TOF hits. See the subsection “Matching” in Section 2.3.3 about the TOF Match Flag. To diminish miss-matched tracks β is required to be greater than 0.05, which removes slow hits, and the TOF of tracks (≈ 7 ns for regular tracks) must be greater than 1 ns.

4.2.3 Pair Cut

The opening angles between a pair of e^+ and e^- tracks are required to be bigger than 30° in order to reduce combinatorial backgrounds. The opening angle distribution from simulation is given in Figure 4.4 with the mean and sigma obtained by fit. Because an optimized opening angle cut does not change

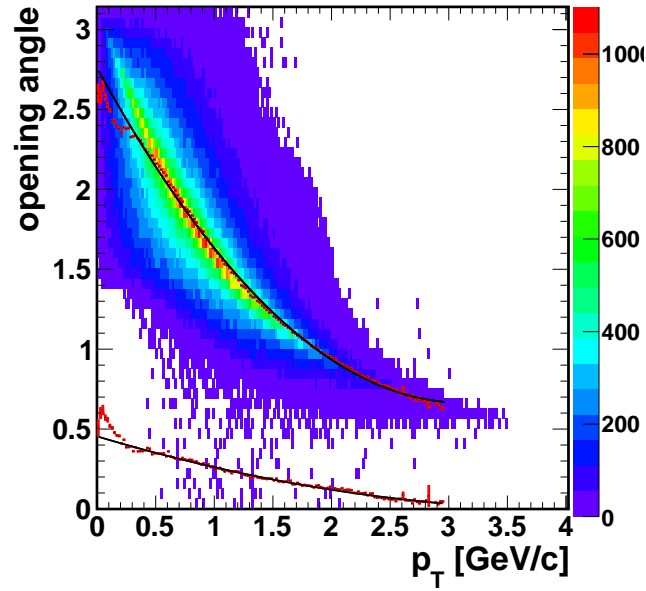


Figure 4.4: e^\pm opening angle from ϕ from simulation with its mean (top) and σ (bottom)

results, the fixed value, 30° , is adopted in this analysis for ease.

The summary of event and track cuts are listed in Table 4.1.

Event Cuts	
Centrality	0-80%
Vertex z-position	$ V_Z < 30$ cm
Vertex x,y-position	$\sqrt{V_X^2 + V_Y^2} < 2$ cm
VPD V_Z	$ V_Z(TPC) - V_Z(VPD) < 3$ cm
# of VPD Hits	number of $VPD_{East,West} \geq 1$
Track Cuts	
nHitsFit	$nHitsFit \geq 22$
nHitsFit / nHitsPoss	$nHitsFit / nHitsPoss > 0.52$
global DCA	$gDCA < 1.1$ cm
p	$0.18 < p < 2$ GeV/ c
p_T	$0.18 < p_T$ GeV/ c
pseudo-rapidity	$ \eta \leq 1$
TOF Match Flag	$\neq 0$
β	> 0.05
Time of flight	> 1 ns
Pair Cut	
Opening angle	$\theta > 30^\circ$

Table 4.1: Event and track cuts

4.3 Electron Identification

With the TOF detector it is possible to separate electrons from other particles at low momentum, $p \leq 0.4$ GeV/ c . Combined with the electron separation power from the relativistic rise of dE/dx at high momentum, the TOF information enables us to identify electrons up to $p = 2$ GeV/ c in this

analysis. An example of the electron distribution in 2D space is presented in Figure 4.5. To identify particles we need to know their distributions in

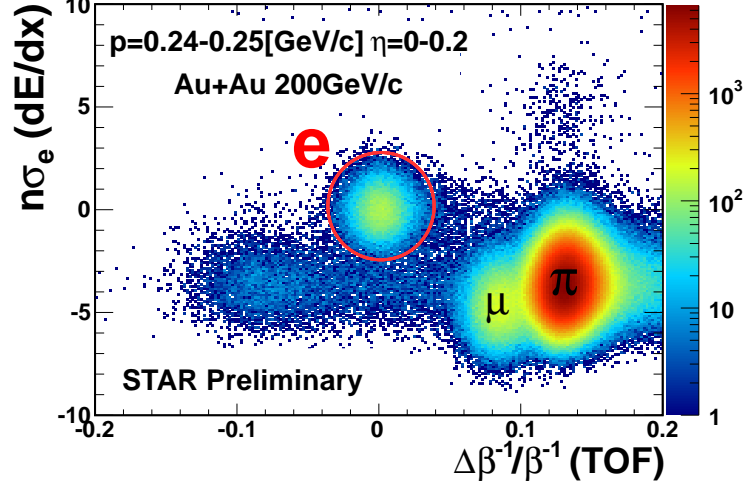


Figure 4.5: Combined electron identification ($p=0.24-0.25$ GeV/ c , $|\eta|=0-0.2$)

measurements, in this case $n\sigma_{dE/dx}^e$ and $\Delta\beta^{-1}/\beta^{-1}$, which are defined in Section 3.3 as

$$n\sigma_{dE/dx}^e = (X - X_{exp}) / \sigma(X) \quad (4.1)$$

$$\Delta\beta^{-1}/\beta^{-1} = (\beta_{TOF}^{-1} - \beta_{exp}^{-1}) / \beta_{TOF}^{-1}, \quad (4.2)$$

where $X \equiv \log(dE/dx)$ and $\beta_{exp}^{-1} = \frac{E}{p} = \sqrt{1 + m_e^2/p^2}$. As discussed in Section 3.3, there are main methods to describe particle distributions. One is using expected distribution, which is obtained from real data at well separated kinematic regions. The other is using well known analytical distributions, such as Gaussian and student's T distributions. In the former method, the actual data can be fit with the expected distribution functions in a not well separated

kinematic region by shifting and scaling them. In the latter method, there is more flexibility. For example, for the Gaussian distributions the sigma parameter can be treated as a fitting parameter as well as the amplitude (scaling) and mean (shifting). In this study, we use the latter method with a Gaussian distribution for both $n\sigma_{dE/dx}^e$ and $\Delta\beta^{-1}/\beta^{-1}$ for all particles except the pion distribution, for which student's T distribution is used to describe the tails of $\Delta\beta^{-1}/\beta^{-1}$ distribution better. First, the parameters of distributions are obtained from pure electron samples, and then, using those distributions we can separate electrons from other particles.

4.3.1 Contaminations

Even with TOF, electrons are well separated only up to $p \approx 0.4$ GeV/ c at STAR, before other particles contaminate the electron distribution. The main contamination comes from pions. Even though the pion distribution is well separated from electrons, because of its large yield, the tail of the pion distribution overlaps the electron distribution. The next largest contaminations are from miss matched kaons and protons, which are regular kaon and proton tracks but matched with the wrong TOF hits mostly caused by gamma conversion, mostly at the TOF trays. Another contamination source is merged pions, which are two pion tracks close to each other that are reconstructed as one track. This distribution is characterized by the same beta value as that of pions and a dE/dx value twice as larger as pion value, since it is the energy loss of two pion tracks. See Figure 4.6 for those contaminations.

Due to these contaminations, it is hard to obtain the correct parameters of the electron distribution. However, by selecting pure electron samples from gamma conversion pairs near collision vertices, it is possible to obtain parameters with a reasonable precision.

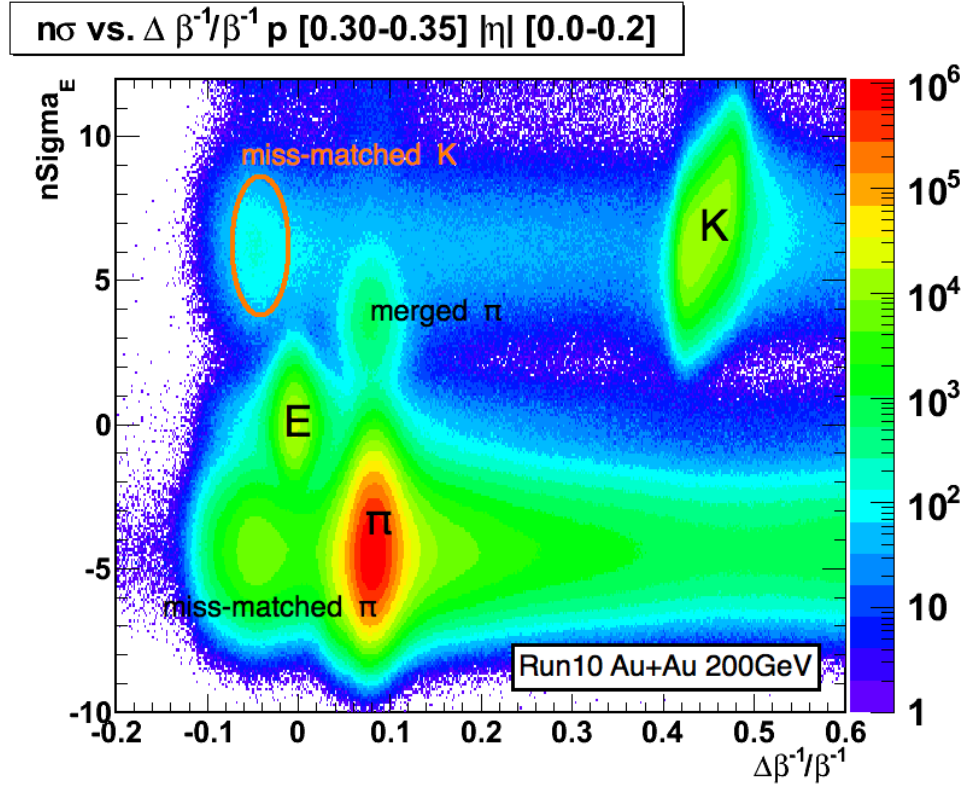


Figure 4.6: Particle distributions around electrons

4.3.2 Pure Electron Sample

There are two purposes for using a pure electron sample.

- Obtain parameters of the electron distribution in $n\sigma_{dE/dx}^e$ vs $\Delta\beta^{-1}/\beta^{-1}$.
- Calculate the TOF matching efficiency for electrons.

Selection Procedure

The same event cuts are used as in the main analysis except the $|V_Z(TPC) - V_Z(VPD)| < 6$ cm cut. The e^-e^+ pairs from gamma conversions are selected by applying geometric cuts.

1. Identify all possible global tracks with $|n\sigma_{electron}| < 2$ cut as well as minimum track quality cuts, $nHitsFit > 15$ points and the ratio of $nHitsFit$ to $nHitsPoss$ to be bigger than 0.52.
2. Select tracks among those global tracks by requiring global DCA less than 2 cm and $0.2 < p_T \leq 2$ GeV/ c as primary track candidates, since we want the primary track electron distribution.
3. For selecting e^-e^+ pairs from gamma conversions (unlike-sign pairs), calculate the pair values from all possible pairs of a primary candidate (electron or positron) and an opposite charged global track candidate.
4. Apply a geometrical cut such that the pair has a DCA between two tracks $dcaAB$ of less than 1 cm, which reflects the fact that real gamma conversion pairs have DCA=0 at conversion points. Since parent gammas come from primary vertices, the following two pair cuts reduce background. The first pair cut is that the reconstructed gamma momentum

has to point in the same direction as that from the primary vertex to the conversion point, which is at the middle point between two tracks at their DCA, *i.e.*, $\mathbf{p}_\gamma \cdot \mathbf{L} > 0$. The other requirement is that the DCA of the parent (γ) to the primary vertex *dcaParent* has to be less than 3 cm. The last and most important cut is requiring invariant mass of the pair m_{ee} to be less than 0.005 GeV/c² since $m_\gamma = 0$.

5. If the pair satisfies those pair cuts, store the primary track as a pure electron (positron).
6. Repeat the procedures for unlike-sign pairs to estimate combinatorial background.

The schematic picture of those pair values is presented in Figure 4.7 and the pair cuts are listed in Table 4.2.

QA

About 199M events (after the event cuts) are analyzed for the pure electron sample. Figure 4.8 shows distributions of the conversion points. The beam pipe in the center, some support structures for the inner tracker at $y=20$ cm, and the TPC inner field cage at $r \approx 50$ cm are evident. Since gamma conversions are expected to happen at those structures, the distribution of the conversion points seem reasonable.

The invariant mass distributions of like-sign (LS) and unlike-sign (ULS) pairs are presented in Figure 4.9a. There is a peak from gamma conversion

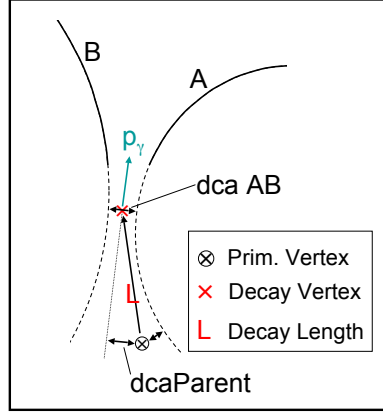


Figure 4.7: Schematic picture of a conversion pair

All Global Tracks (e^- and e^+)
$ n\sigma_e^{global} \leq 2$
$nHitsFit \geq 15$
$nHitsFit / nHitsPoss > 0.52$
Primary Tracks
Primary Tracks
$gDCA \leq 2$ cm
$0.18 < p_T < 2$ GeV/c
Pair Cuts
$dcaAB < 1$ cm
$\mathbf{p}_\gamma \cdot \mathbf{L} > 0$
$dcaParent < 3$ cm
$m_{ee} < 0.005$ GeV/c ²

Table 4.2: Track cuts for pure electron sample

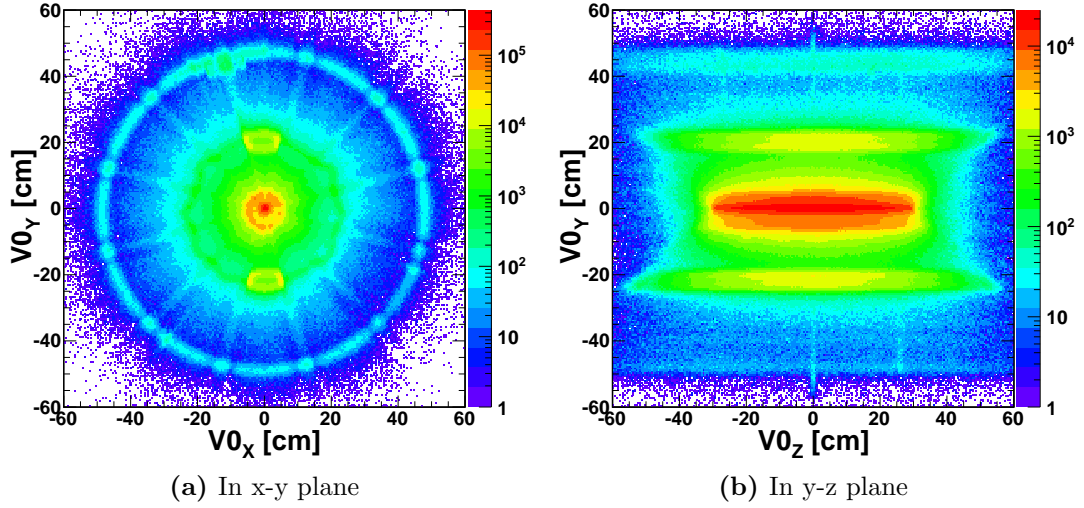


Figure 4.8: Reconstructed conversion points

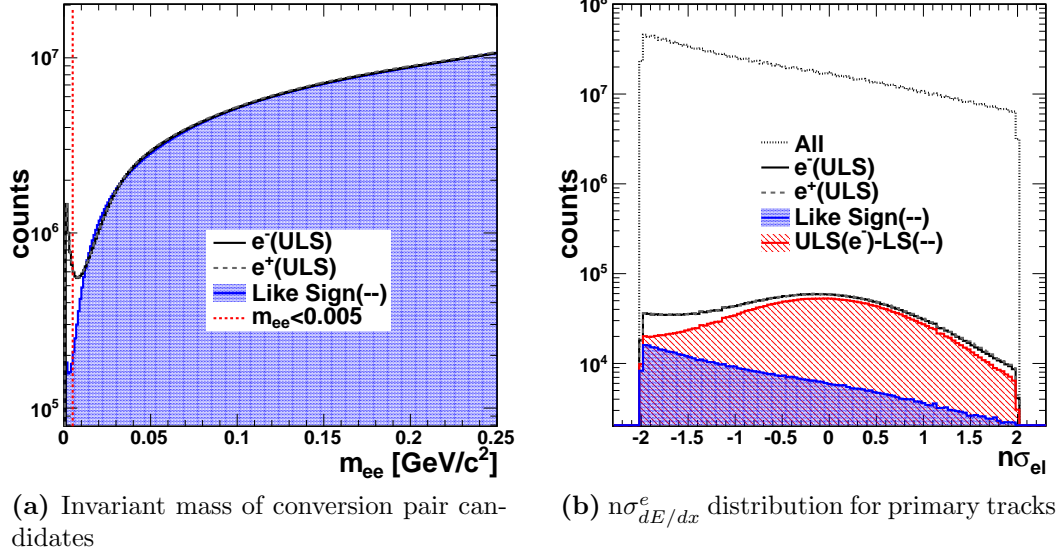


Figure 4.9: QA histograms for the pure electron sample

pairs around invariant mass equal to 0 in unlike-sign pairs. The normalized like-sign distribution (blue filled area) represents background and agrees with unlike-sign distribution at large invariant mass. Inside the invariant mass cut region (less than the red dashed line) most of them are from unlike-sign pairs (gamma conversion pairs). Figure 4.9b shows $n\sigma_{electron}$ distributions. All accepted primary tracks without the pair cuts are plotted with a short dashed line, which is labeled as “All” in the legend. The unlike-sign distributions and like-sign distributions are after the invariant mass cut. The red filled histogram shows the unlike-sign distribution minus the like-sign distribution (background), which represents electron tracks without background. It should look like a Gaussian distribution with $\mu = 0$ and $\sigma = 1$ by definition of $n\sigma$. By integration, the backgrounds in the unlike-sign samples are estimated to be

$\approx 17\%$ at $-2 \leq n\sigma_{el} \leq 2$ and $\approx 11\%$ at $-0.5 \leq n\sigma_{el} \leq 2$. The $-0.5 \leq n\sigma_{el} \leq 2$ cut is used in the calculation of the TOF matching efficiency in Section 4.5.1. To save time like-sign pairs are calculated with only 43M events (Figure 4.9). The unlike-sign pairs look similar in the final sample of 199M events.

2D Fit for Electrons

The parameters of electron distribution are obtained by fitting the pure electron sample up to $p = 2$ GeV/ c . After this step, all electron distribution parameters except its yield (or relative heights) are determined. The yield parameter is necessary for the probability cut and the yield is determined by fitting all of the data used in the main analysis with the other relevant particle distributions. The fit procedures are as follows:

1. Fill 2D $(\Delta\beta^{-1}/\beta^{-1}, n\sigma_{dE/dx}^e)$ histograms at each momentum bin and η bin with the pure electron sample with additional track cut, $\text{gDCA} < 1.5$ cm. Those bin sizes are $\Delta p = 20$ MeV/ c and $\Delta\eta = 0.2$. The distribution is divided into five η bins to reflect the resolution dependencies on momentum and η because the momentum resolution is a function of p_T while the β resolution is a function of p , where p and p_T have a relationship $p = p_T \cosh\eta$.
2. In each momentum and η bin, fit with a 2D Gaussian function in an area defined by $(n\sigma^X/a)^2 + (n\sigma^Y/b)^2 \leq 1$, where $X \equiv \Delta\beta^{-1}/\beta^{-1}$, $Y \equiv n\sigma_{dE/dx}^e$, and $n\sigma^X \equiv (X - X_{exp})/\sigma_{exp}^X$ (same for Y). By definition X_{exp}

and $Y_{exp} = 0$. In this study, we set $\sigma_{exp}^X = 0.013$, $\sigma_{exp}^Y = 1$, $a = 3$, and $b = 2$. With this criteria, we can cut out the 2D histogram in an ellipse.

3. After 2-dimensional fit, project the cut-out data and fit function onto both $\Delta\beta^{-1}/\beta^{-1}$ and $n\sigma_{dE/dx}^e$ axes for a quality check of the fit.

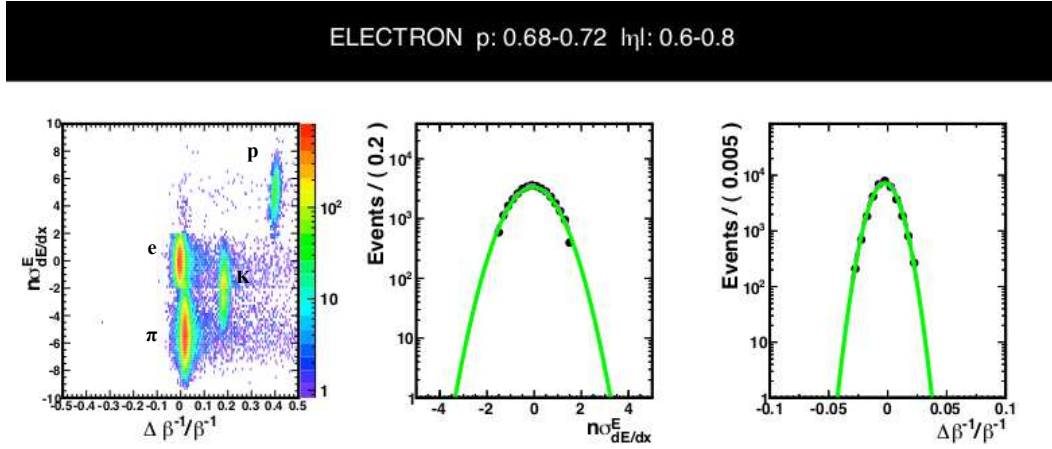


Figure 4.10: 2D fit of the pure electron sample at $p = 0.3 - 0.32$ [GeV/c], $|\eta| = 0.2 - 0.4$

Figure 4.10 shows an example of a 2D fit at $p = 0.7$ GeV/c and $|\eta| = 0.7$. In this pure electron sample fit, only one particle distribution is used. Because $n\sigma_{dE/dx}^e$ values from global and primary tracks are different, there are some tracks of other particles outside of $|n\sigma_{dE/dx}^e| < 2$ even after the pure electron selection cut on $n\sigma_{dE/dx}^e$. When the TOF matching efficiency is calculated from the pure electron sample, additional cuts on $n\sigma_{dE/dx}^e$ are applied to reduce those contamination from other particles. Figure 4.11 shows the obtained fit parameters for the electron distribution (2D Gaussian distribution).

ELECTRON Fit Parameters

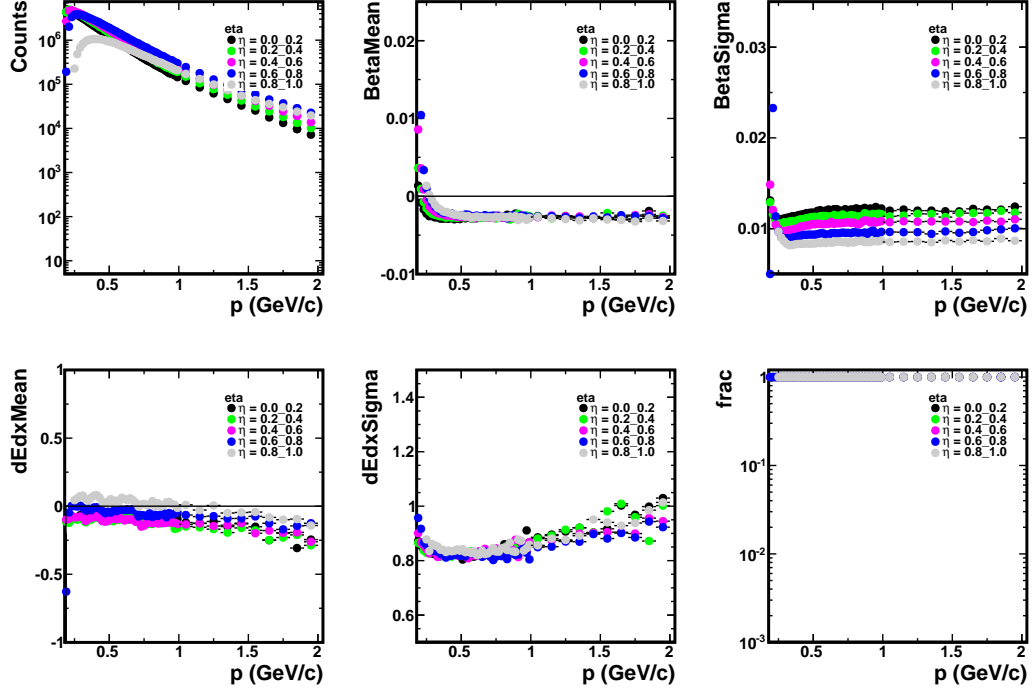


Figure 4.11: Summary of the 2D fit parameters in the pure electron sample fit

4.3.3 Fit with All Relevant Particles

The relative amplitudes between particles are required for applying the probability cut. For acquiring the amplitude of the electron distribution as well as the other relevant particle distributions, those distributions have to be fitted together. The multi-particle fitting is difficult and careful fit procedures are necessary as described below:

1. Fill 2D ($\Delta\beta^{-1}/\beta^{-1}$, $n\sigma_{dE/dx}^e$) histograms at each momentum bin and η

bin with the event and track cuts explained in Section 4.2.

2. Fix mean and sigma of the electron's $\Delta\beta^{-1}/\beta^{-1}$ and $n\sigma_{dE/dx}^e$ to the values extracted from the pure electron sample. Then, fit π , K, p distributions along with the electron distributions.
3. Fit the miss matched kaons and protons at well separated momentum regions ($p < 0.5$ GeV/ c for the miss matched kaons and $p < 0.9$ GeV/ c for the miss matched protons) to obtain N_{missK}/N_K and N_{missp}/N_p ratios.
4. Fix the N_{missK}/N_K and N_{missp}/N_p ratios at all momentum bins.
5. Fit all particles, electron, pion, merged pion, and miss matched kaon and proton, to obtain their yields. Only the amplitude is a free fit parameter for the electron distribution. In each momentum and η bin, the fit is performed with 2D Gaussian functions in the same areas defined in the previous pure electron sample fit. This criterion cuts out the ellipse shapes as shown in the bottom middle panel in Figure 4.12.
6. Project the data in the ellipse and the fit function onto both $\Delta\beta^{-1}/\beta^{-1}$ and $n\sigma_{dE/dx}^e$ axes for a fit quality check.

Student's T distribution In the fit procedure explained above, we employed the student's T distribution to describe the long tails of pion distribution in $\Delta\beta^{-1}/\beta^{-1}$. It is important to estimate the pion tails correctly so that

ELECTRON $p: 0.48-0.50 \quad |\eta|: 0.0-0.2$

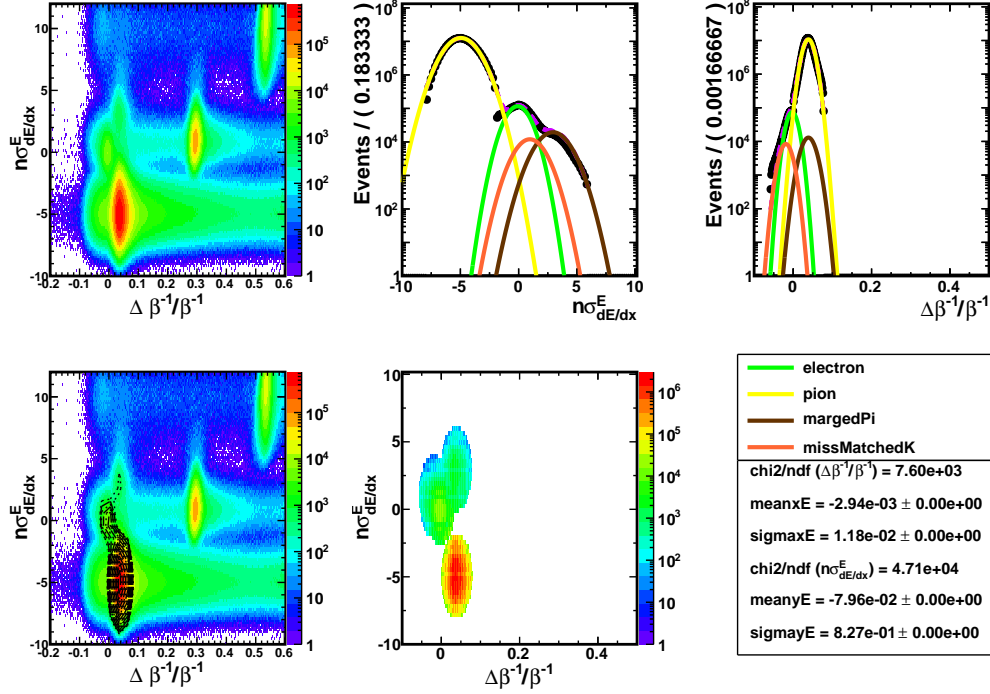


Figure 4.12: 2D fit example at $p = 0.48 - 0.5 \text{ GeV}/c$, $|\eta| = 0 - 0.2$

the yield of the electron distribution located on the tails is extracted. The applicability of the student's distribution can be interpreted as follows.

Due to the central limit theorem, we expect that the deviation of the measured start-time, which is an average time of all lit upVPDs, from the true start time would distribute as a Gaussian (normal) distribution for a fixed number of lit upVPDs. The distributions of the start-time deviation with different numbers of lit upVPDs have different resolutions. The combined distribution is no longer a Gaussian distribution, but a student's T distribution.

A student's T distribution can be obtained by convolving a Gaussian and a Gamma function, which represents a distribution of resolutions in this case. See Appendix A.1 for details about the student's T distribution.

Separation Power The separation power measures the extent to which each particle's distribution is separated. The separation powers between electrons and the other particles in the fit are plotted in Figure 4.13.

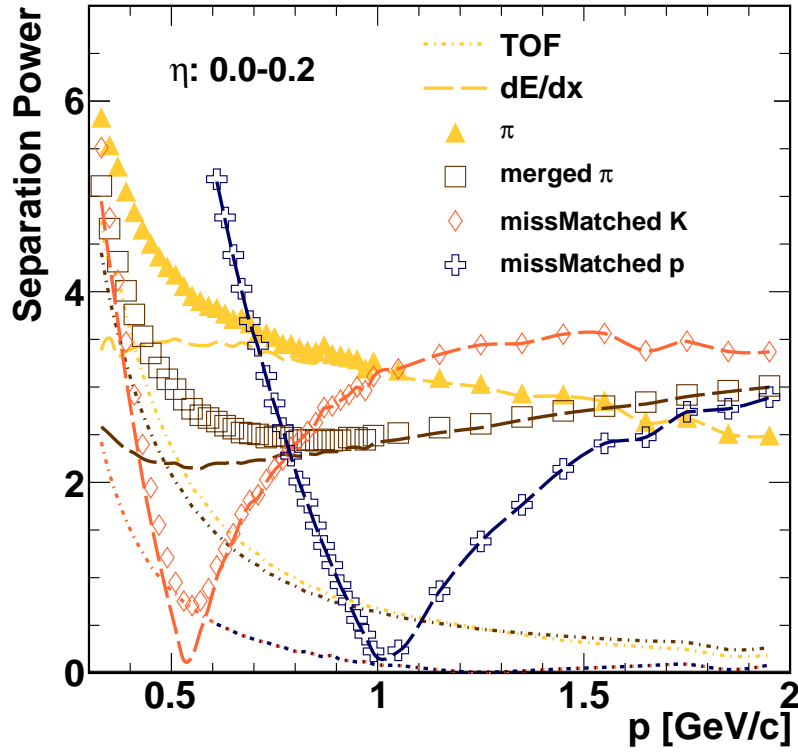


Figure 4.13: Separation power between electrons and other particles

Distribution after PID cut: Real (Blue) & Mc (Red) ($0.80 \leq p < 0.82$ [GeV/c])

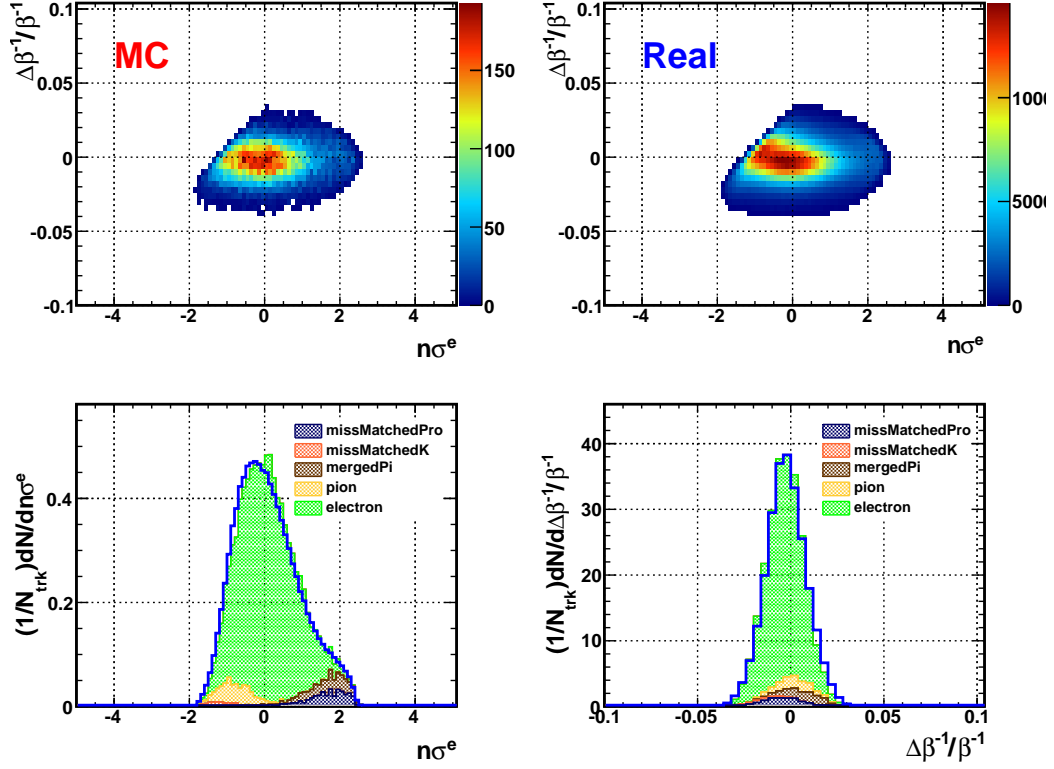


Figure 4.14: Distribution of real and MC data after the 2D $n\sigma$ and probability cuts. The real data after the PID is presented as blue lines and the MC data is given as filled histograms in the bottom panels.

4.3.4 2D $n\sigma$ and Probability cuts

Although the obtained $\Delta\beta^{-1}/\beta^{-1}$ and $n\sigma_{dE/dx}^e$ distributions can be used separately in PID, using them in combination provides more separation power. The $n\sigma$ and probability cuts defined in Section 3.2.2 are extended to two

variable versions. The 2D $n\sigma$ cut is defined as

$$\left(\frac{n\sigma_X}{a}\right)^2 + \left(\frac{n\sigma_Y}{b}\right)^2 < 1, \quad (4.3)$$

where $X \equiv \Delta\beta^{-1}/\beta^{-1}$ and $Y \equiv n\sigma_{dE/dx}$. The above inequality selects out an ellipse on the $n\sigma_X$ and $n\sigma_Y$ axes with radii of a and b , and $a = b = 3$ in this analysis. This method of applying dE/dx and β cuts simultaneously has an advantage over other methods in which the two cuts are applied separately because, in the later case, a rectangle in the 2D histogram is cut while in our method an ellipse with higher purity is cut. The 2D probability cut is defined as

$$P^e(X, Y) \equiv \frac{N^e \times \text{PDF}(X; \boldsymbol{\theta}_X^e) \times \text{PDF}(Y; \boldsymbol{\theta}_Y^e)}{\sum_i N^i \times \text{PDF}(X; \boldsymbol{\theta}_X^i) \times \text{PDF}(Y; \boldsymbol{\theta}_Y^i)}, \quad (4.4)$$

where PDF is a probability density function and $\boldsymbol{\theta}_X^i$ and $\boldsymbol{\theta}_Y^i$ are parameter sets for particle i . The summation in the denominator includes only electron and pion for simplification. All PDFs are Gaussian functions except the pion $\Delta\beta^{-1}/\beta^{-1}$ distribution, for which the student's T function is used. In this analysis, a probability bigger than 60% is required to be identified as an electron or positron. Figure 4.14 shows the selected track distributions compared to MC tracks. The MC tracks are generated according to the particle distributions to check the PID method (both of them are normalized for the sake of comparison).

4.4 Signal Extraction (reconstruction)

In this section, the method of reconstructing ϕ signals from the identified e^\pm pairs in the previous section is introduced.

4.4.1 Invariant Mass Reconstruction

The ϕ invariant mass is reconstructed from all e^+ and e^- pairs in the same event (unlike-sign distribution). Since these pairs include uncorrelated pairs as well, the mixed-event technique is adopted to estimate the uncorrelated combinatorial background [43] [44]. Invariant mass can be calculated as

$$M_{e^+e^-}^2 = (E_{e^+} + E_{e^-})^2 - (\vec{p}_{e^+} + \vec{p}_{e^-})^2, \quad (4.5)$$

where the mass of the electron is used to calculate E_{e^\pm} . It is worth mentioning that since the electron mass is used to calculate the invariant mass of a resonance, even if a kaon pair from a ϕ meson is misidentified as an electron-positron pair, the invariant mass values from those kaon pairs have a smaller invariant mass due to the large mass difference of an electron and kaon. Thus, small kaon contaminations do not affect our ϕ analysis.

4.4.2 Mixed-event Technique (background subtraction)

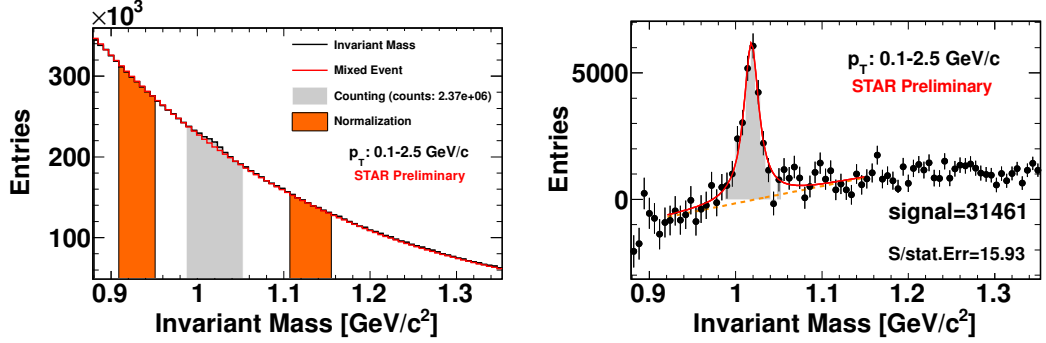
The mixed-event background is reconstructed with electron and positron pairs from different events, where no real correlations from resonances are possible. However, in the same event, even e^+ and e^- pair not from a ϕ can have some correlations originating from experimental artifacts in the TPC. In order

to include those event-wise geometrical correlations in the mixed-event technique, e^+ and e^- pairs are selected only from the same event class. We defined the event classes with 10 bins in both V_Z position and reaction plane angle of the events [45], and 8 centrality bins so that the geometrical correlations are taken into account in the mixed-event background as well. One event is mixed with 20 other events in the same event class.

Like-sign pairs Another technique to reproduce the combinatorial background is the like-sign technique. In this technique, instead of pairing e^+ and e^- , the same charge sign electrons or positrons in the same event are paired to calculate invariant mass. The resulting invariant mass distribution does not contain any resonance signals but includes the geometrical correlations as well as the combinatorial background. The disadvantage of this method is that the background errors are larger compared to that of the mixed-event background. In the mixed-event technique, the number of mixed events can be chosen to reduce the errors, in this analysis a factor of $1/\sqrt{20} \approx 0.22$ smaller than the errors in the like-sign technique. Due to this disadvantage, the like-sign technique is not used in this analysis.

4.4.3 Signal Counting and Breit-Wigner Function Fit

After normalizing the mixed-events background to the unlike-sign invariant mass distribution and subtracting it from the unlike-sign invariant mass distribution, we can extract ϕ signals as in Figure 4.15b. The statistical



(a) Invariant mass distribution of the e^+e^- pairs in the same event (black line) with the normalized mixed-event background (red line). The orange areas show the normalization areas for the mixed-event background.

(b) p_T integrated $\phi \rightarrow e^+e^-$ signals after the mixed-events background subtraction. The red lines are the non-relativistic Breit-Wigner functions representing the $\phi \rightarrow e^+e^-$ signals and the orange slope shows the residual background.

Figure 4.15: e^+e^- invariant mass distribution at $p_T = 0.1 - 2.5$ GeV/c

errors of the invariant mass histogram are calculated as following. Let N_S^i be the i -th bin entry after the background subtraction and $N_S^i = N_R^i - \alpha N_{BG}^i$ where N_R^i and N_{BG}^i are i -th bin entries of the invariant mass histogram from the same-event and mixed-event, respectively, and α is the normalization factor of the background, typically $\approx 0.05 = 1/20$. Then the statistical error of N_S^i is given by

$$(\Delta N_S^i)^2 = N_R^i + \alpha^2 N_{BG}^i + N_{BG}^i \frac{\alpha}{\sum_j N_{BG}^j} (1 + \alpha), \quad (4.6)$$

where we assume the statistical errors of bin entries are Poisson, i.e., $\Delta N_{R,BG}^i = \sqrt{N_{R,BG}^i}$. The first and second terms correspond to the errors from the same-event and mixed-event invariant mass histograms, respectively. The third term is from the normalization factor itself and the summation in the denominator

is over bins in the normalization ranges.

To obtain the resonance signal shape, we fit the invariant mass distribution with the Breit-Wigner function plus slope, which represents residual background. The Breit-Wigner function is defined as

$$f_{BW} \equiv \frac{dN}{dM_{ee}} = \frac{N\Gamma/2\pi}{(M_{ee} - M_0)^2 + \Gamma^2/4}, \quad (4.7)$$

where N is the area under the Breit-Wigner function, M_0 is the resonance mass position, and Γ is a decay width. The $\Gamma/2\pi$ is a normalization factor. From this fit function, the mass and width of the resonance are extracted. The yield at each p_T bin is estimated by counting the invariant mass bin entries above the residual background function in the signal range at $M_{ee} = M_\phi \pm 30 \text{ MeV}/c^2$ (typically, the bin counting consists about 85% of total yield), and by integration of the fit function outside of the signal range as expressed in Eq. 4.8,

$$\frac{d^2N}{dydp_T} = \sum_i \left. \frac{dN}{dydp_T} \right|_{M_{ee}^i} - f_{BG}(M_{ee}^i) + \int_{min}^{M_{ee}^{low}} + \int_{M_{ee}^{hi}}^{max} dM_{ee} f_{BW}(M_{ee}) \quad (4.8)$$

where M_{ee}^i implies i-th bin in the M_{ee} axis and f_{BG} is the residual background function. The $M_{ee}^{low,hi}$ are low and hi edges of the signal counting range. The min and max are $M_{ee} = 0.9$ and $1.15 \text{ GeV}/c$, and those limits are far enough from the signal shape to include all signals. The dy is equal to 2 in this analysis since we consider ϕ resonances in $|y| < 1$. The statistical error of $d^2N/dydp_T$ is estimated from errors in the bins and the residual background function. The

latter errors are calculated from the covariant matrix, σ_{ij} , of the fit parameters and gradients of the function at bin center with respect to the fit parameters,

$$df(M_{ee})^2 = \sum_{i,j} \frac{\partial f(M_{ee})}{\partial p_i} \sigma_{ij} \frac{\partial f(M_{ee})}{\partial p_j}. \quad (4.9)$$

To measure the ϕ transverse momentum spectrum, we repeat the same procedure in each transverse momentum bin. The p_T bin widths are determined so that all bins have similar significances.

4.4.4 dN/dy and Mean Transverse Momentum Estimation

After applying all corrections explained in Section 4.5, we obtain the corrected p_T spectrum of ϕ and fit it with the Maxwell-Boltzmann (m_T exponential) distribution using an “integral” fit option in the ROOT software. The Maxwell-Boltzmann distribution is given as

$$\frac{1}{2\pi p_T} \frac{d^2 N}{dy dp_T} = \frac{dN/dy}{2\pi T(m_0 + T)} e^{-(m_T - m_0)/T}, \quad (4.10)$$

where $m_T = \sqrt{m_0^2 + p_T^2}$. The total yield, dN/dy , is calculated by bin counting at $p_T = 0.1-2.5$ GeV/ c and integration of the fit function at $p_T = 0-0.1$ & $2.5-10$ GeV/ c . The mean p_T is also calculated in a similar fashion to that expressed in Equation 4.11. The extrapolation or integration of the fit function contributes 3.7% for dN/dy and 8.3% for $\langle p_T \rangle$.

$$\frac{dN}{dy} = \sum_i \left. \frac{dN}{dy dp_T} \right|_{p_T^i} \Delta p_T^i + \int_0^{p_T^{low}} + \int_{p_T^{hi}}^{10} dp_T f_{MB} \quad \text{and} \quad (4.11)$$

$$\langle p_T \rangle = \left[\sum_i \left. \frac{dN}{dy dp_T} \right|_{p_T^i} p_T \Delta p_T^i + \int_0^{p_T^{low}} + \int_{p_T^{hi}}^{10} dp_T p_T f_{MB} \right] / dN/dy, \quad (4.12)$$

where p_T^i is an i -th p_T bin center and Δp_T^i is a bin width at the bin, and f_{MB} is the Maxwell-Boltzmann distribution function.

4.5 Efficiency Correction

Due to the inefficiencies in detectors and the PID method, some amount of e^\pm which contribute to the ϕ signal are not reconstructed. To obtain the corrected total yield, we need to estimate those inefficiencies, which consist of TPC acceptance and track efficiency, TOF matching efficiency (TOF acceptance plus matching efficiency), and PID method efficiency. We assume each efficiency is independent from each other, i.e., total efficiency is calculated by multiplying all efficiencies.

4.5.1 TOF Matching Efficiency

The TOF matching efficiency and acceptance of the TOF detectors are calculated from data by comparing all reconstructed tracks with tracks that have associated TOF hits. We need to match TPC tracks with TOF hits since to calculate velocity β the track length is also necessary. Due to the

smaller coverage ($|\eta| < 0.9$) of the TOF system, tracks do not always have corresponding TOF hits. Currently, there is no reliable simulation of the TOF system available to estimate the efficiency. Instead the real data is used to estimate it. Because there is some particle dependency in the efficiency, we use the pure electron sample in this study. The TOF matching efficiency is defined as

$$\text{Eff}^{TOF} \equiv N_{(TOF|TPC)} / N_{TPC}^{selected}, \quad (4.13)$$

where $N_{TPC}^{selected}$ is number of tracks in the TPC after the track quality cuts and $N_{(TOF|TPC)}$ is the number of those tracks which have a matched TOF hit.

As shown in Figure 4.10, even the pure electron sample has contaminations from other particles. Several cuts on the $n\sigma_{dE/dx}^e$ are applied to minimize them. The contaminations are also obvious in Figure 4.16b, where the contamination bands intersect the electron distribution. The estimated TOF matching efficiencies are presented in Figure 4.16a. The black line shows the efficiency without any additional cuts to the pure electron sample. The pink and purple points represent different cut ranges in $n\sigma_{dE/dx}^e$. Those differences are included in the systematical uncertainties. The efficiencies in ϕ and η in the TPC are plotted for QA purposes in Figure 4.17a and 4.17b.

4.5.2 PID Cut Efficiency (acceptance)

The PID cut efficiency is calculated directly from the two-dimensional Gaussian distributions for the electron obtained in Section 4.3.2. All of the necessary information to calculate PID efficiency is contained in the fraction of

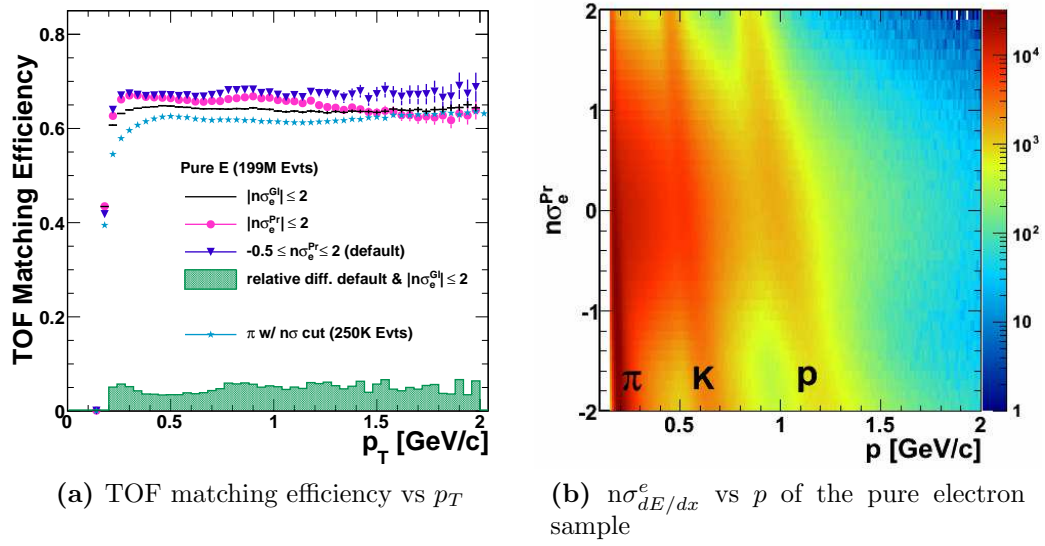


Figure 4.16: TOF matching efficiency

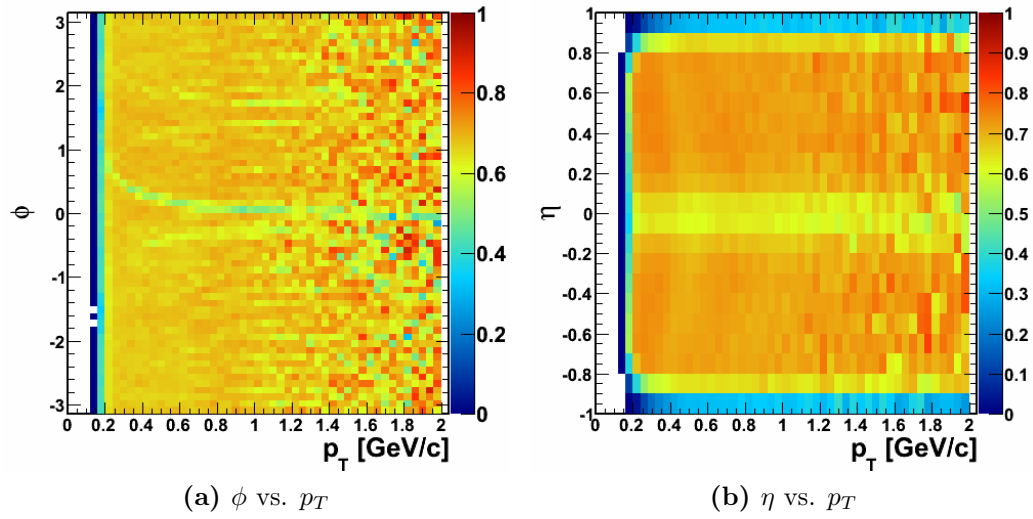


Figure 4.17: TOF matching efficiency in 2D

accepted electrons compared to the total electron distribution. In other words, once the PID cut region is determined by the probability cut, the efficiency

only depends on the electron distribution. The other particle distributions do not affect the accuracy of the PID efficiency. The PID efficiency is estimated in the following way:

1. Generate electrons according to the fit distribution.
2. Apply the PID cuts ($2D \ n\sigma$ and probability cuts) to each generated track.
3. Calculate the efficiency as $\text{Eff}^{PID} \equiv N_{RC}/N_{MC}$.

As evident in the last line, the efficiency does not depend on the amplitude of the distribution because it is a ratio. The systematical uncertainty of the PID efficiency depends only on the means and sigmas in the electron distribution. This is why obtaining electron distribution with as little contamination as possible is important.

Purity

For quality assurance, the purity of the identified electrons and positrons is estimated in a similar manner. For this estimation, the other particle distributions are also necessary as described below:

1. Generate $\Delta\beta^{-1}/\beta_E^{-1}$ vs. $n\sigma_E$ distributions for the other particles according to the fit parameters using Monte Carlo method as in the bottom left plot in Figure 4.18. $\rightarrow N_{MC}^i$.
2. Select tracks with the PID cuts. $\rightarrow N_{Sel}^i$.

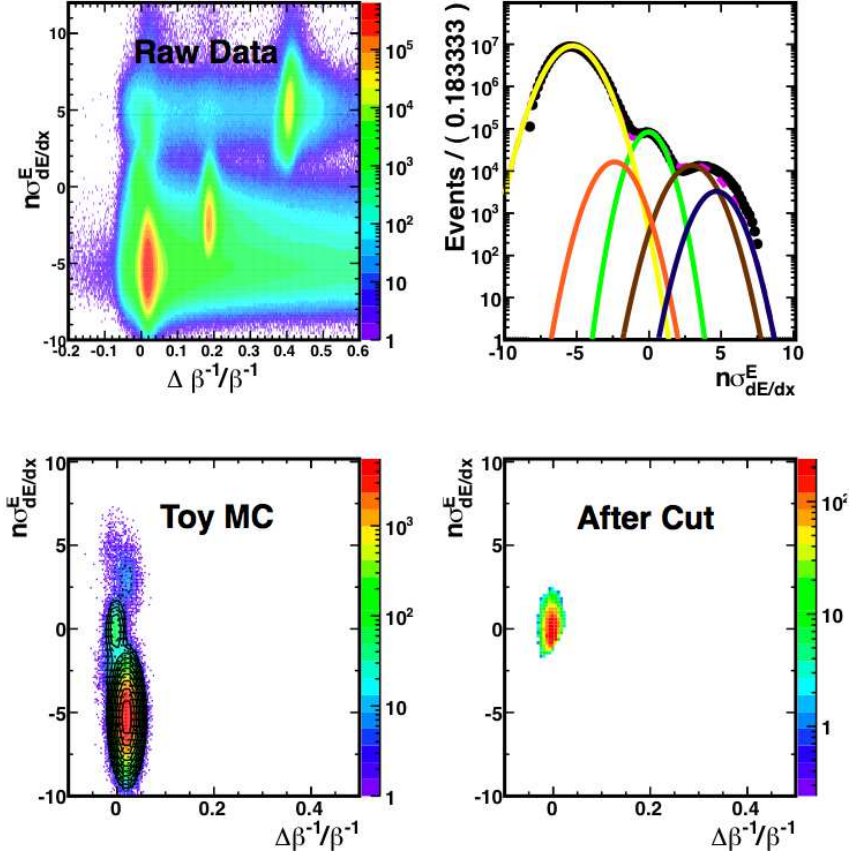


Figure 4.18: PID efficiency and purity calculation

3. Calculate the purity as $Pur_i^{PID Cut} \equiv N_{Sel}^i / \sum_j N_{Sel}^j$, where j includes all relevant particles.

The PID efficiency, purity, and contaminations are plotted in Figure 4.19a. By integrating over the momentum range $p = 0.1 - 2 \text{ GeV}/c$, the total electron purity is estimated to be 94.8%. The accepted yields are also given in Figure 4.19b to show the amount of other tracks included in the selected electrons and positrons.

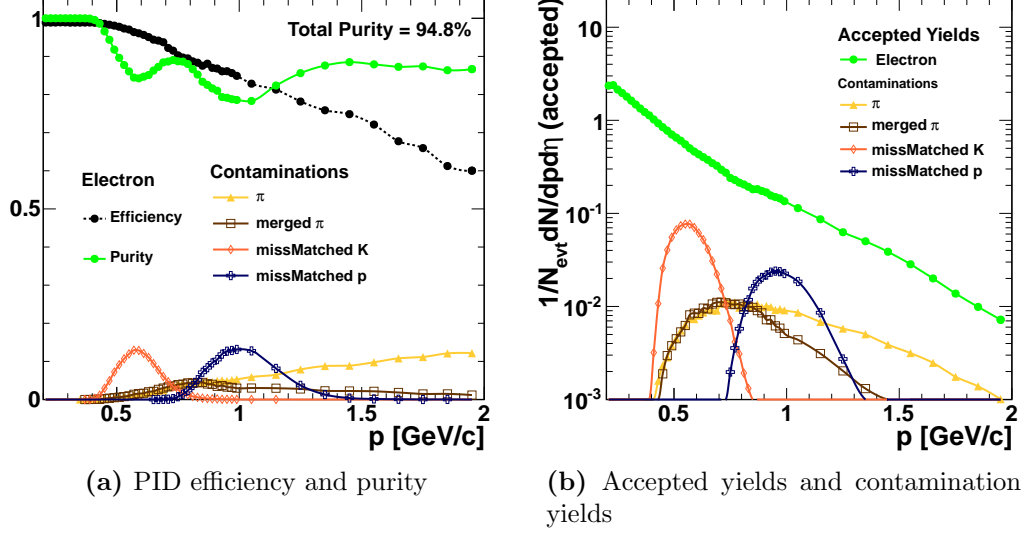


Figure 4.19: PID efficiency and contamination yields

4.5.3 TPC Acceptance & Track Quality Cut Efficiency

The track Reconstruction (Rc) efficiency and TPC acceptance have been obtained by embedding Monte-Carlo (MC) $\phi \rightarrow e^+e^-$ tracks into real events at the detector's response level with GEANT and reconstructing them via the STAR production chain along with real tracks. In this way, the efficiency includes the TPC geometry acceptance and the track reconstruction efficiency.

While the desired final result is dN/dy in $|y| \leq 1$, in the real measurement $dN/dy|_{|y| \leq 1}$ might or might not include the ϕ signals from outside of the y range due to the detector resolution and the limited detector acceptance, $|\eta| \leq 1$. To correct for these effects, the MC parent particles, ϕ , are generated for not only $|y| \leq 1$ but also beyond the $|y| = 1$ limits. Because the detector

resolution in η or y is only a few percent, generating the MC parents within $|y| \leq 1.2$ was sufficient.

We also estimate the track quality cuts efficiency by applying the track quality cut used in our analysis to the reconstructed tracks. At this point, the TOF matching efficiency and PID efficiency are applied to each daughter track. If both daughters, e^+e^- , are reconstructed after all of the efficiencies are applied, the parent ϕ is counted as reconstructed. The final pair efficiency is calculated as

$$\text{Eff}^{total} \equiv N_{Rc}^{\phi \rightarrow e^+e^-} / N_{MC}^{\phi \rightarrow e^+e^-}. \quad (4.14)$$

In order to obtain correct efficiency for $dN/dy|_{|y| \leq 1}$, the MC ϕ s are counted only within $|y| \leq 1$ and the Rc ϕ s are counted within $|y| \leq 1$ regardless if the input (MC) ϕ originates at a $|y|$ larger than 1 to simulate real measurements. The errors on the efficiency are calculated with the Bayesian approach [46], as follows,

$$Err \equiv \sqrt{\frac{N_{Rc} + 1}{N_{MC} + 2} \left(\frac{N_{Rc} + 2}{N_{MC} + 3} - \frac{N_{Rc} + 1}{N_{MC} + 2} \right)}. \quad (4.15)$$

Figure 4.20 shows the changes of ϕ reconstruction efficiency as each efficiency is applied. The total ϕ reconstruction efficiency is presented in purple at the bottom of the figure.

4.6 Systematic Error Estimation

In this study, we consider systematical errors from the simulation, PID parameters, TOF matching efficiency, and fit conditions. The systematic un-

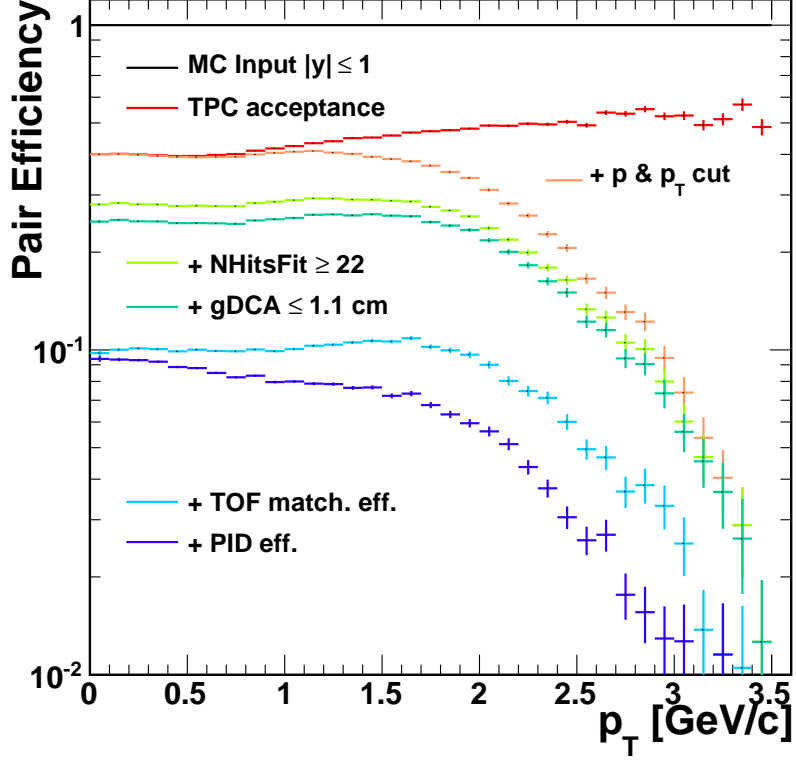


Figure 4.20: ϕ reconstruction efficiency

certainties of the $\phi \rightarrow e^+e^-$ yield were estimated by varying the track selection cuts such as global DCA, NHitsFit points, and the PID probability cut value. The default values and variations are listed in Table 4.3. We also varied the normalization ranges for the mixed-events, the signal fit range, fit function form for the residual background, and histogram binning.

The procedures are as follows:

1. Vary fit conditions:

Category		Default	Variation
Simulation	NHitsFit	NHitsFit ≤ 22 points	20, 21, 23, 24
	global DCA	gDCA ≤ 1.1 cm	0.9, 1.0, 1.2 (cm)
	Opening Angle	30°	40, 50, 60 (°)
Particle identification		PID Purity $\geq 60\%$	50, 55, 65, 70 (%)
TOF Matching Efficiency		$-0.5 < n\sigma_e^{pr} \leq 2$	$-2 < n\sigma_e^{pr} \leq 2$, no $n\sigma_e^{pr}$ cut

Table 4.3: Condition changes in systematic error study

Repeatedly fit the ϕ invariant mass signal with different fit conditions, such as normalization ranges, fit ranges, and fit functions for the residual background (the first and second degree polynomials). Then, calculate weighted mean and (biased) variance for $dN/dydp_T$, mass, and width as,

$$\mu_{X(p_T)} \equiv \sum_i w_i X_{i(p_T)} / \sum_j w_j \quad \text{and} \quad (4.16)$$

$$\sigma_{X(p_T)}^2 \equiv \sum_i w_i (X_{i(p_T)} - \mu_{(p_T)})^2 / \sum_j w_j, \quad (4.17)$$

where X are $dN/dydp_T$, mass, or width. The weights, w_i , are $1/(\text{err. of } X_{i(p_T)})^2$. The summations are over all of the fit conditions. Take the square root of the variance, σ_X , as a systematic uncertainty from this fit procedure.

2. Vary cut conditions:

Change one quality cut value and repeat step 1. To separate systematical errors from statistical, the weighted means from the step 1 are used. Repeat this for all values around the default cut value. Take the square root of the variance from the default value, X'_0 , as systematic errors from

these cut conditions,

$$\sigma_{X(p_T)}'^2 \equiv \sum_i w'_i (X'_{i(p_T)} - X'_{0(p_T)})^2 / \sum_j w'_j \quad (4.18)$$

where $X'_{i(p_T)} = \mu$ and $w'_i = 1/\sigma^2$ from the previous step.

3. Total systematic errors:

Total systematic errors are calculated by adding each systematical error in quadrature without considering correlations between them.

The summary of systematic errors is presented in Table 4.4. The values are given in percentages of the measured values. The errors in each p_T bin are shown in Figure 4.21 for $d^2N/dydp_T$, 4.22a for the fit mass, and 4.22b for the fit width.

Category		$d^2N/dydp_T$ (%)	mass (%)	width (%)
Simulation	NHitsFit	6.3	0.066	7.6
	global DCA	6.4	0.048	6.4
	Opening Angle	2.3	0.013	2.6
Particle identification		4.6	0.043	5.9
TOF Matching Efficiency		8.3	0.0	0.0
Fit condition		3.8	0.007	3.4

Table 4.4: Systematic errors averaged over p_T bins in percentage

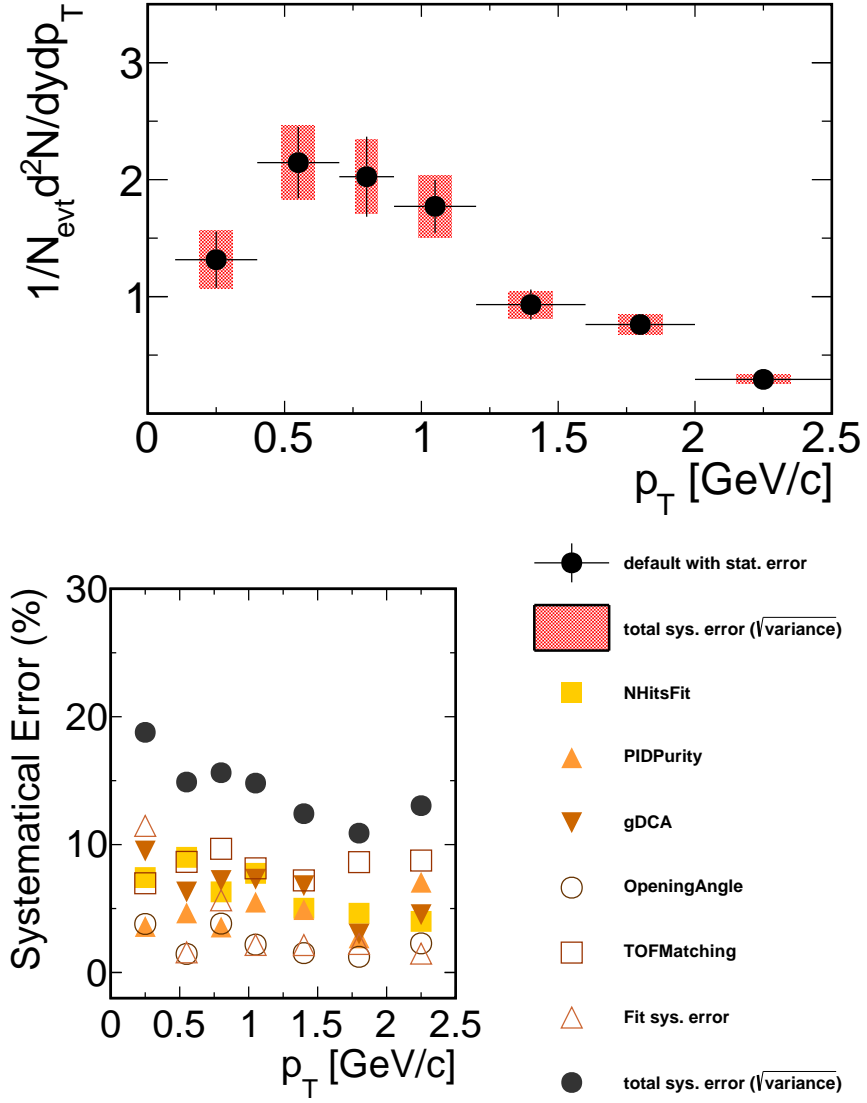
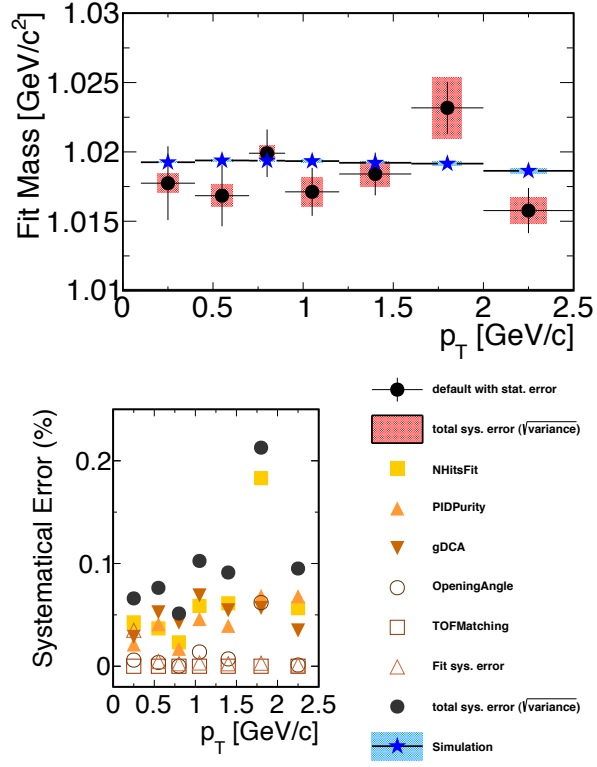
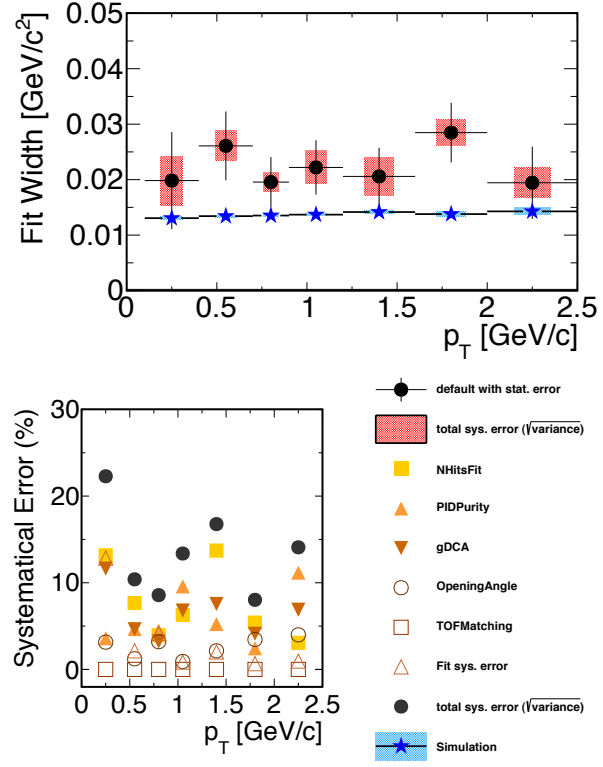


Figure 4.21: Systematical uncertainty on p_T spectrum



(a) Fit mass



(b) Fit width

Figure 4.22: Systematical uncertainty of fit mass and width

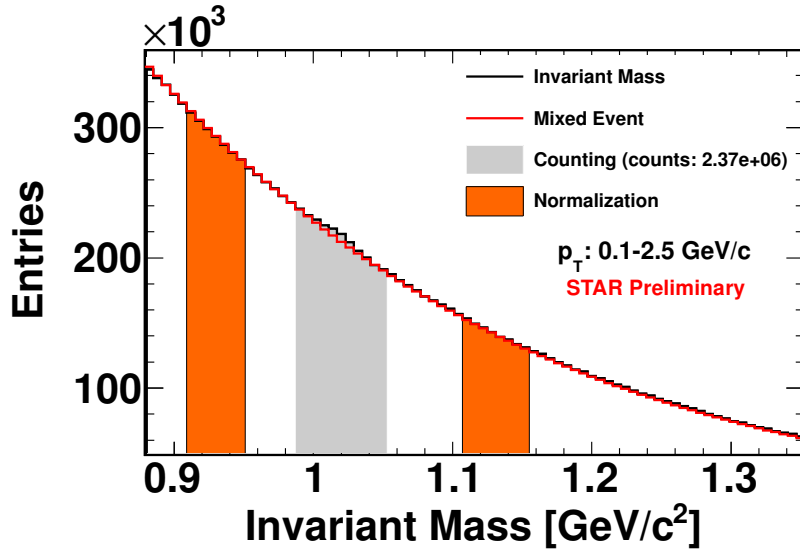
Chapter 5

Results

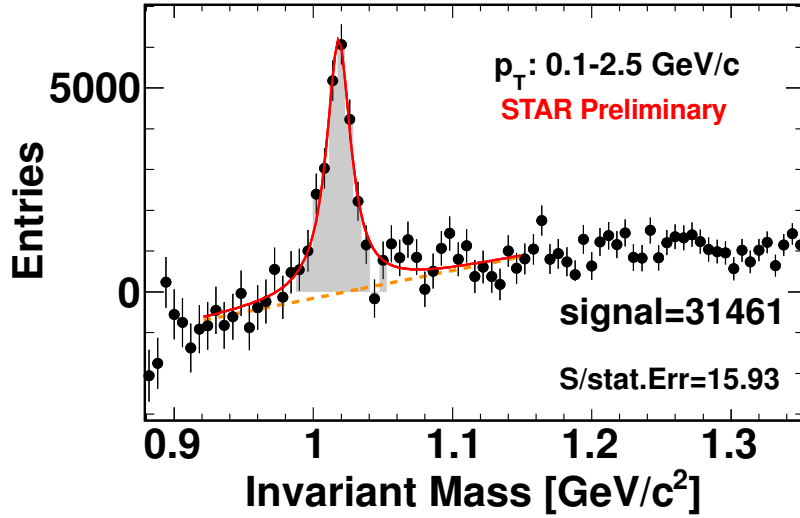
In this chapter, various results of this analysis are presented. The extracted ϕ signals in each p_T bin as well as the p_T integrated signal are discussed in Section 5.1. To investigate the possible mass shift and width broadening, the ϕ signals are compared to the simulation results in Section 5.2. The p_T spectrum of $\phi \rightarrow e^+e^-$ is presented in Section 5.3. The total yield, dN/dy , and mean transverse momentum, $\langle p_T \rangle$, of ϕ are obtained from the spectrum. In Section 5.4 the $\phi \rightarrow e^+e^-$ p_T spectrum is compared to the spectrum from the hadronic decay channel, $\phi \rightarrow K^+K^-$ [47].

5.1 Signals

Figure 5.1a shows the invariant mass distribution of the e^+e^- pairs in the same event (black line) with the normalized mixed-event background (red line) in the transverse momentum range of 0.1 to 2.5 GeV/ c . The orange areas show the normalization areas for the mixed-event background. The $\phi \rightarrow e^+e^-$ signal after the mixed-event background subtraction in the same p_T range is presented in Figure 5.1b. The red line is the non-relativistic Breit-Wigner function representing the $\phi \rightarrow e^+e^-$ signal and the orange line shows the



(a) Invariant mass distribution of the e^+e^- pairs in the same event (black line) with the normalized mixed-event background (red line). The orange areas show the normalization areas for the mixed-event background.

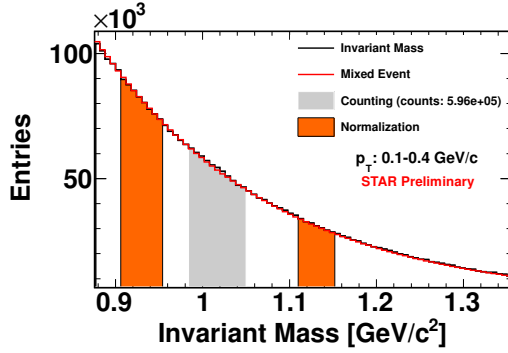


(b) p_T integrated $\phi \rightarrow e^+e^-$ signals after the mixed-events background subtraction. The red lines are the non-relativistic Breit-Wigner functions representing the $\phi \rightarrow e^+e^-$ signals and the orange slope shows the residual background. The gray area is a signal counting range.

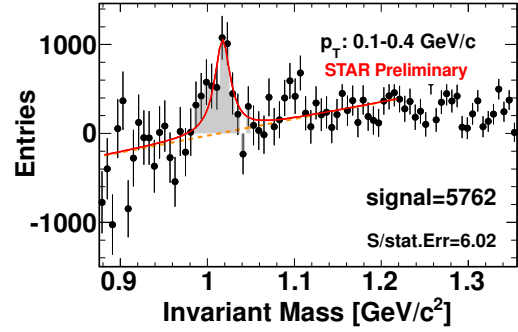
Figure 5.1: e^+e^- invariant mass distribution in Au+Au collisions at $\sqrt{s_{NN}} = 200$ GeV/c at $p_T = 0.1 - 2.5$ GeV/c 114

residual background. The gray regions show the signal counting regions in both figures. We can extract the signals with significance of 15.93.

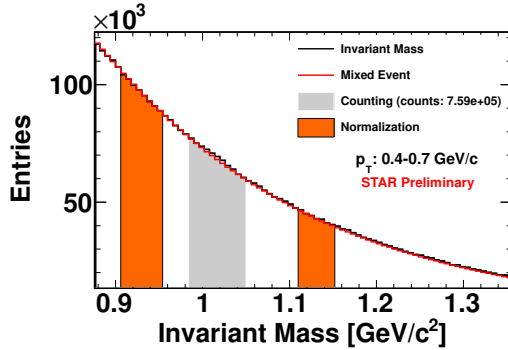
The p_T integrated signal is divided into seven p_T bins as shown in Figures 5.2, 5.3, and 5.4, and the same procedures of the background subtraction and fitting are conducted. The p_T bin sizes are determined so that each extracted signal has a significance of at least 6.



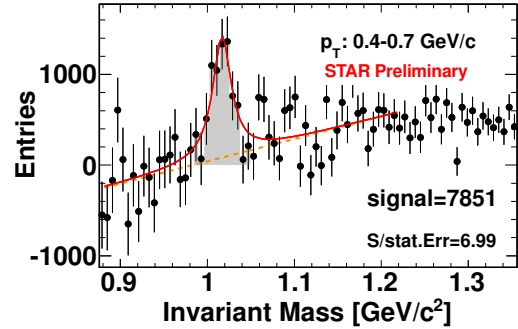
(a) e^+e^- invariant mass distribution



(b) After mixed event background subtraction

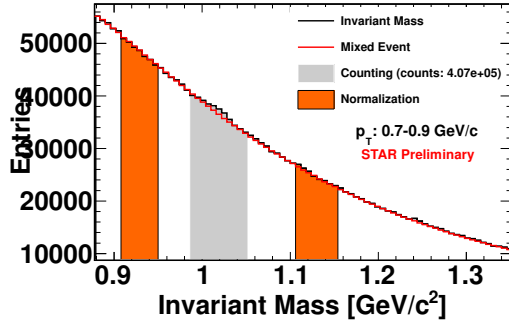


(c) e^+e^- invariant mass distribution

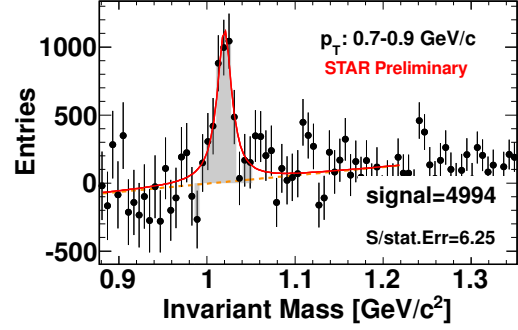


(d) After mixed event background subtraction

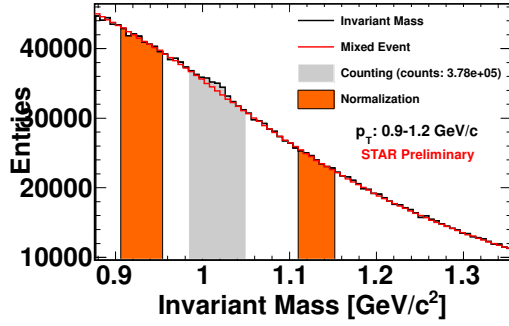
Figure 5.2: e^+e^- invariant mass distributions and $\phi \rightarrow e^+e^-$ signals



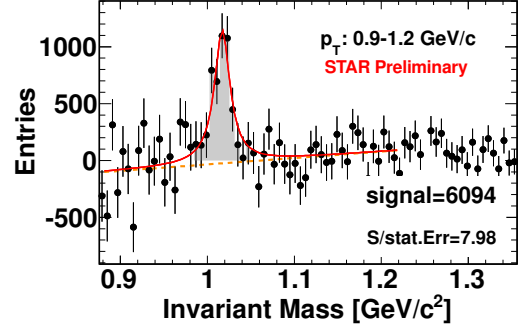
(a) e^+e^- invariant mass distribution



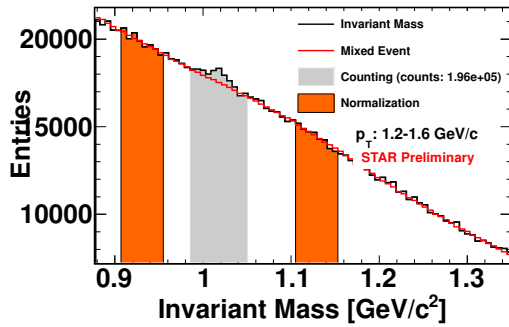
(b) After mixed event background subtraction



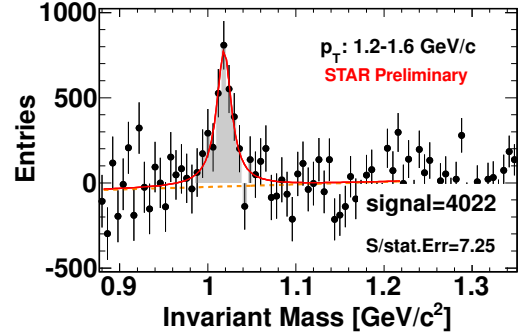
(c) e^+e^- invariant mass distribution



(d) After mixed event background subtraction

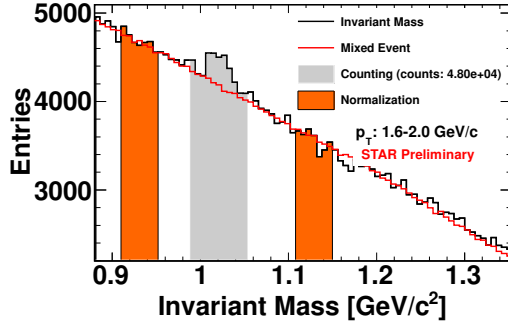


(e) e^+e^- invariant mass distribution

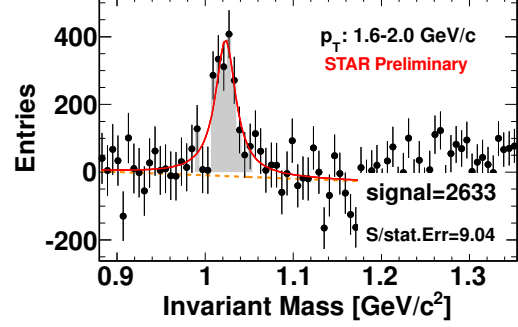


(f) After mixed event background subtraction

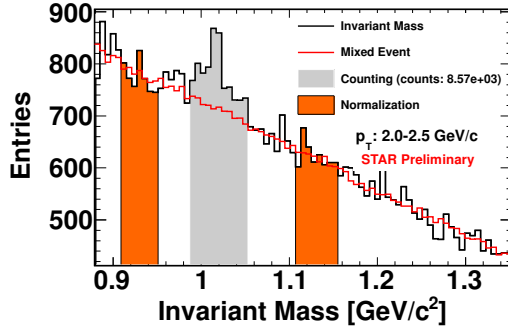
Figure 5.3: e^+e^- invariant mass distributions and $\phi \rightarrow e^+e^-$ signals



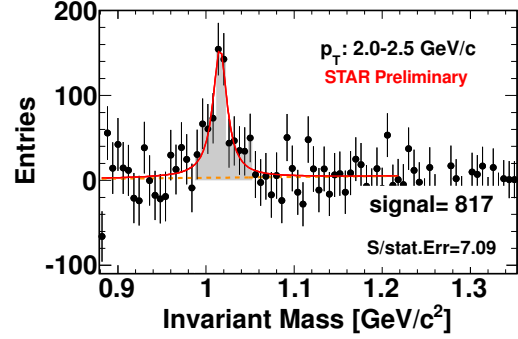
(a) e^+e^- invariant mass distribution



(b) After mixed event background subtraction



(c) e^+e^- invariant mass distribution

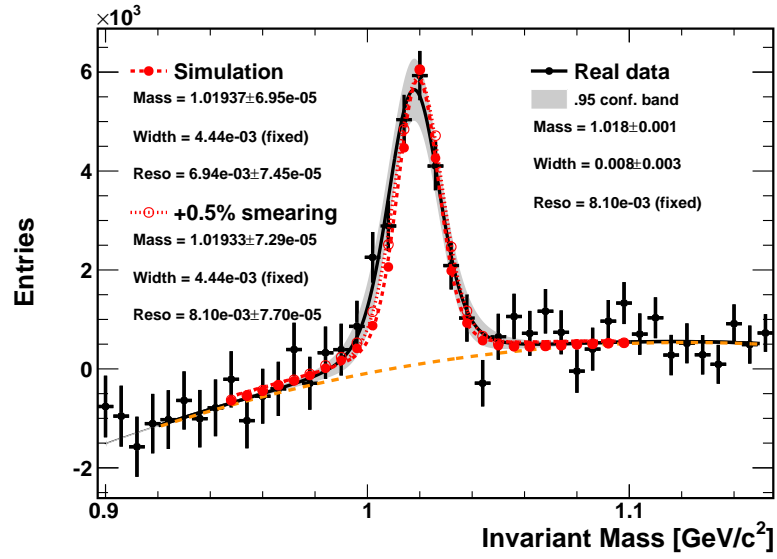


(d) After mixed event background subtraction

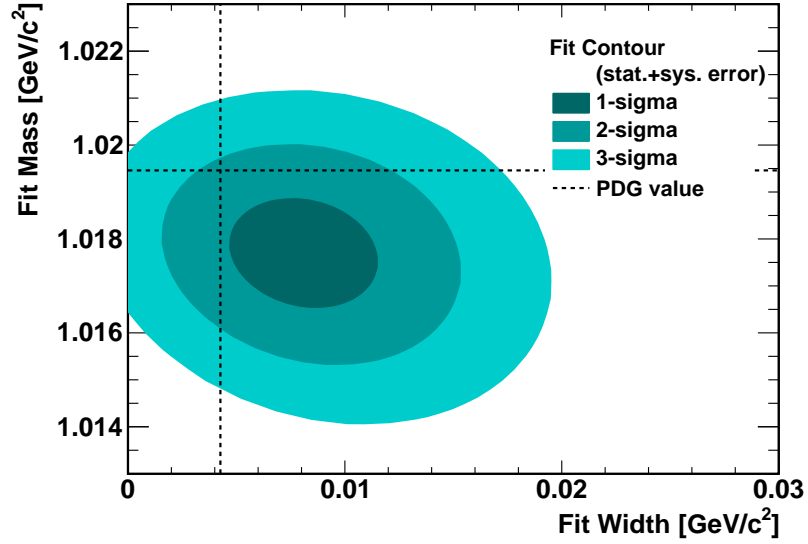
Figure 5.4: e^+e^- invariant mass distributions and $\phi \rightarrow e^+e^-$ signals

5.2 Mass and Width

In order to examine if there are mass shifts and/or width broadening, the resulting invariant mass distributions are compared to the simulated $\phi \rightarrow e^+e^-$ distributions. Simulations are done by embedding ϕ resonances into the real Au+Au collision data at the detector response level and reconstructed by the STAR reconstruction chains along the real tracks so that the simulation data can include the detector resolutions and inefficiencies. Two



(a) Invariant mass distribution comparison between the real data and simulation



(b) Fit contour of the fit to the real data

Figure 5.5: Mass and Width from the p_T integrated signal at $p_T = 0.1 - 2.5 \text{ GeV}/c$

sets of simulations are considered here. One is the default simulation data and the other is the simulation with additional 0.5% momentum smearing, which comes from studying the invariant mass line shape of J/ψ . The smearing is calculated as $\sigma_{p_T} = 5.1 \times 10^{-3} p_T$.

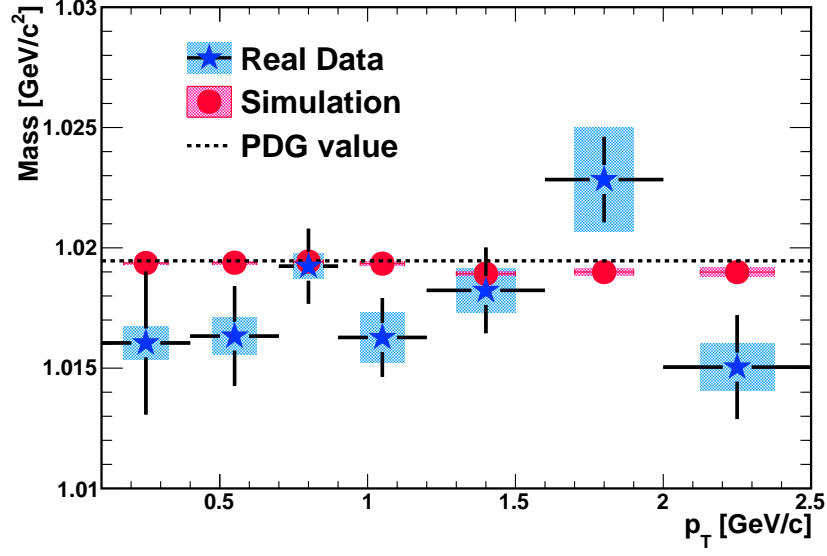
In Figure 5.5a, the p_T integrated ϕ invariant mass distribution is plotted with the two simulations. The black points are the real data and the red solid points and open circles are the default and additional momentum smearing simulations, respectively. Both simulations are added to the background function and normalized to the real data at the highest bin. To fit the invariant mass distributions, the Voigt function is used so that the detector resolutions are incorporated. The Voigt function is a convolution of the Breit-Wigner function with the Gaussian function, which represents the detector resolutions and smears the Breit-Wigner shape. The black solid line is the Voigt fit function for the real data and the red long dashed and short dashed lines are the Voigt fit functions to the default and the additional smearing simulations, respectively. First, in order to determine the detector resolution, the simulations are fitted with the Voigt function with a fixed Breit-Wigner width set to the value of the vacuum ϕ width. Next, the real invariant mass shape is fitted by the Voigt function with a fixed Gaussian resolution set to the detector resolution value from the previous fit to the simulation. For the detector resolution, the value from the simulation with additional momentum smearing is used because it is more realistic. This allows the width of the resonance signal to be separated from the detector resolution and it can be

compared directly with the vacuum width of ϕ . The fit contours are presented in Figure 5.5b. The fit contours include the statistical and systematic errors added in quadrature. The fit results are $M_\phi = 1017.7 \pm 0.77 \pm 0.88 \text{ MeV}/c^2$ (1.48σ away from the PDG value) and $\Gamma_\phi = 7.98 \pm 2.52 \pm 2.28 \text{ MeV}/c^2$ (1.05σ away from the PDG value). From this invariant mass shape, we set an upper limit of $15.3 \text{ MeV}/c^2$ on the width and a lower limit of $1015.3 \text{ MeV}/c^2$ on the mass with a 95% confidence level.

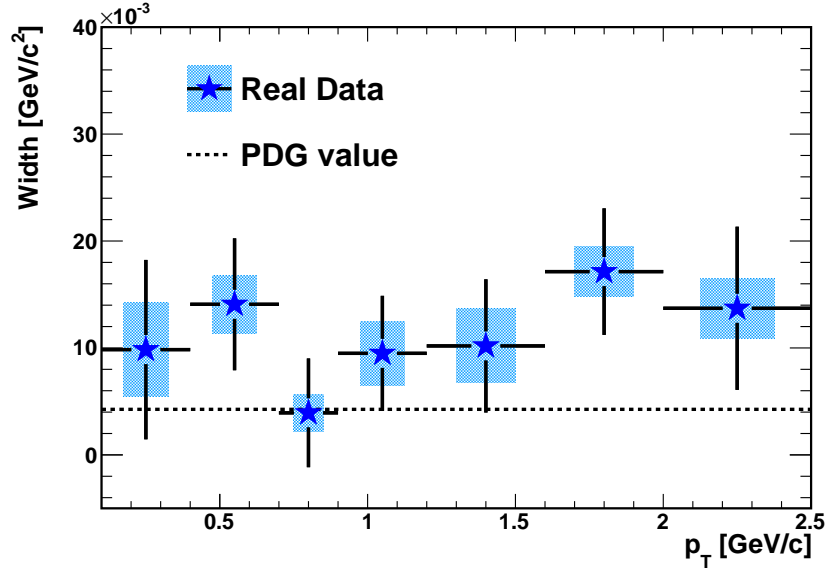
Figures 5.6 show the fit results of the mass and width of the $\phi(1020)$ meson in each p_T bin with blue star points. The bars and filled boxes are statistical and systematic errors, respectively. The simulation results with additional smearing and the particle data group (PDG) values [21] are plotted with red points and a dashed line, respectively. Here, the same fit process as in the fit to the p_T integrated signal are repeated in each p_T bin. The mass deviations from simulation results are 1.40σ and 1.56σ at $p_T = 1.6 - 2$ and $2 - 2.5 \text{ GeV}/c$, respectively. The width deviations are 1.58σ and 2.11σ at $p_T = 0.4 - 0.7$ and $1.6 - 2 \text{ GeV}/c$, respectively. Those deviations are less than 2σ in the mass and width, but the fit values are systematically lower in the mass and higher in the width.

5.3 Corrected $\phi(1520)$ Transverse Momentum Spectrum

The corrected $\phi \rightarrow e^+e^-$ yields at the rapidity $|y| < 1$ for the 0-80% centrality events from Au + Au collisions at $\sqrt{s_{NN}} = 200 \text{ GeV}$ are presented in Figure 5.7. The $\phi(1020)$ yield per unit rapidity (dN/dy) is calculated by



(a) Mass vs. p_T of $\phi(1020)$



(b) Width vs. p_T of $\phi(1020)$

Figure 5.6: Mass and width vs. p_T . The blue star points represent the fit results. The bars and filled boxes are statistical and systematic errors, respectively. The red points are the simulation with the additional momentum smearing. The dashed lines show the PDG values. The widths of the simulation are not plotted since those are fixed to the PDG value. The systematic errors on the width from the simulation are included in those of real data in the width plot.

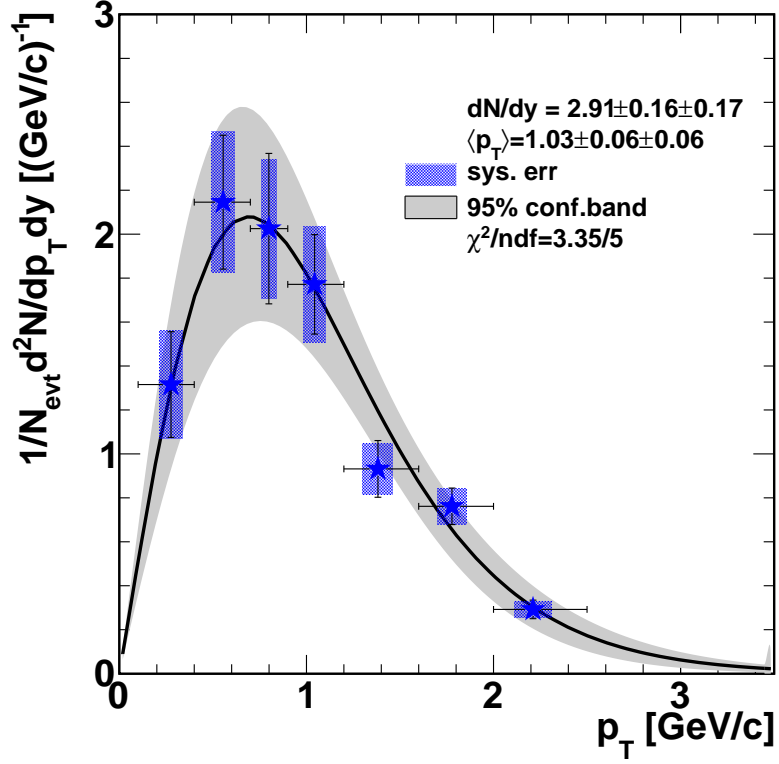


Figure 5.7: Corrected $\phi \rightarrow e^+e^-$ yields within rapidity $|y| < 1$ for the 0-80% centrality events from Au + Au collisions at $\sqrt{s_{NN}} = 200$ GeV. The vertical bars are statistical errors and the boxes are the systematic errors. The solid line is the exponential fit functions and the gray band represents a 95% confidence band of the fit. The values of dN/dy and $\langle p_T \rangle$ correspond to the best estimated values and statistical and systematical errors. The histograms are plotted with mean p_T in each p_T bin estimated from the fit functions.

counting signals within the transverse momentum range and integrating the exponential fit function for the rest as explained in Section 4.4.4. The mean transverse momentum ($\langle p_T \rangle$) is obtained in a similar way. The contributions from the extrapolation to unmeasured p_T regions are 3.7% and 8.3% for dN/dy and $\langle p_T \rangle$, respectively. We obtain $dN/dy = 2.91 \pm 0.16$ (stat.) ± 0.17 (sys.)

and $\langle p_T \rangle = 1.03 \pm 0.06$ (stat.) ± 0.06 (sys.) GeV/ c . The points are shifted to the mean p_T in each bin estimated from the fit function. The dN/dy deviation from the hadronic channel result [47] ($dN/dy = 2.68 \pm 0.15$) is 0.83σ . The $\langle p_T \rangle$ deviation from the hadronic channel result ($\langle p_T \rangle = 0.962 \pm 0.0145$ GeV/ c) is 0.79σ .

p_T (GeV/ c)	$\langle p_T \rangle$ (GeV/ c)	$dN/dydp_T$ (GeV/ c) ⁻¹	stat. err.	sys. err.
0.1-0.4	0.276	1.316	0.241	0.247
0.4-0.7	0.555	2.146	0.305	0.320
0.7-0.9	0.799	2.025	0.342	0.316
0.9-1.2	1.043	1.772	0.226	0.262
1.2-1.6	1.382	0.932	0.129	0.116
1.6-2.0	1.778	0.761	0.083	0.083
2.0-2.5	2.211	0.292	0.042	0.038

Table 5.1: $\phi \rightarrow e^+e^-$ corrected yield

5.4 Comparison to Hadronic Decay Channel

Figure 5.8 shows the $\phi \rightarrow e^+e^-$ invariant yields in blue and the red points represent STAR published $\phi \rightarrow K^+K^-$ results [47] in the same centrality range (0-80%). The error notations are the same as in the Figure 5.7. The red filled boxes on the hadronic result show 10% systematical errors mentioned in Reference [47]. In the bottom panel, the relative differences between those two results, i.e., $(N_{ee} - N_{KK})/N_{KK}$, are plotted. The N_{KK} are calculated by integrating the fit function to the hadronic decay channel result (dashed line) in each p_T bin. The ϕ measurements in the di-leptonic decay channel deviates from the STAR published hadronic decay results at most 1.4σ (at

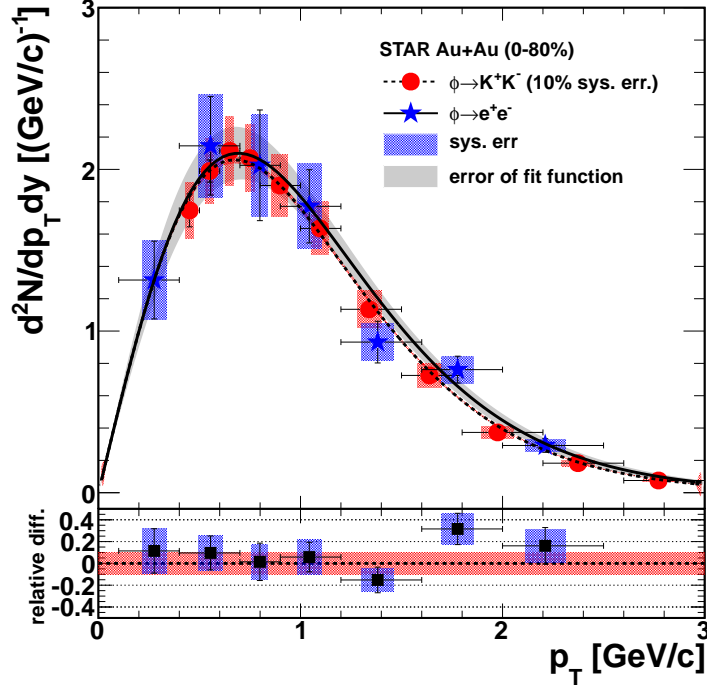


Figure 5.8: The $\phi \rightarrow e^+e^-$ and $\phi \rightarrow K^+K^-$ yields within rapidity $|y| < 1$ for the 0-80% centrality events from Au + Au collisions at $\sqrt{s_{NN}} = 200$ GeV. The vertical bars are statistical errors and the boxes are the systematic errors. The dashed and solid lines are the exponential fit functions to the hadronic and leptonic decay channel results and the gray band represents errors of the fit function to the leptonic result. The histograms are plotted with mean p_T in each p_T bin estimated from the fit functions.

$p_T = 1.6 - 2$ GeV/ c) if we take into account the 10% systematical uncertainty of the published result.

5.5 Model Comparison

To better understand this result, we compare it with a model calculation (from Ralf Rapp in personal communication), which is based on an

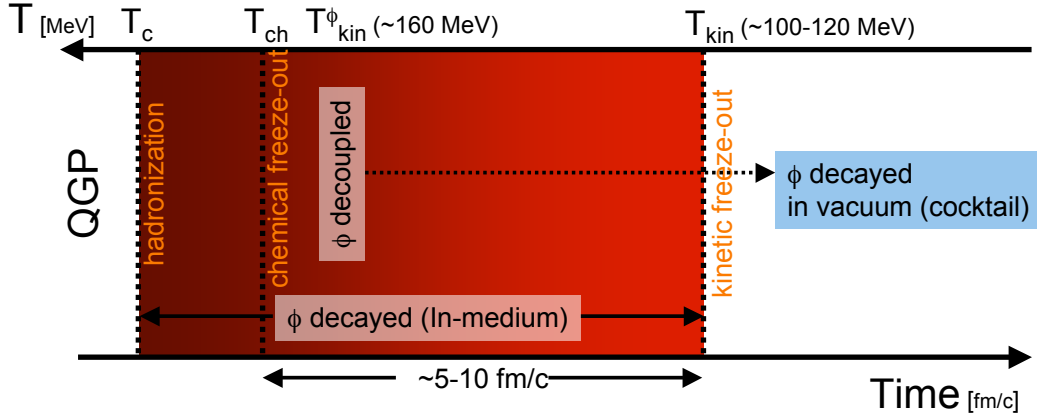
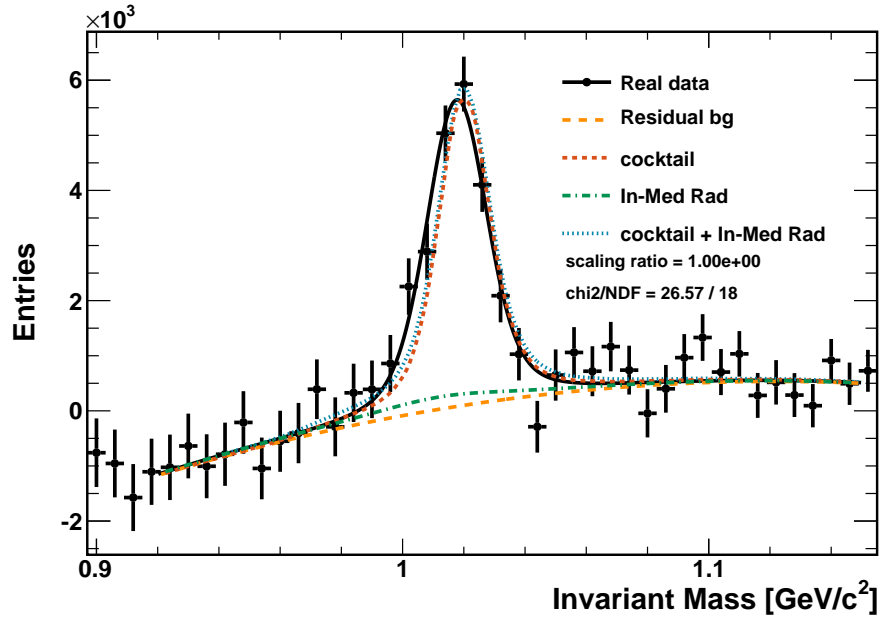
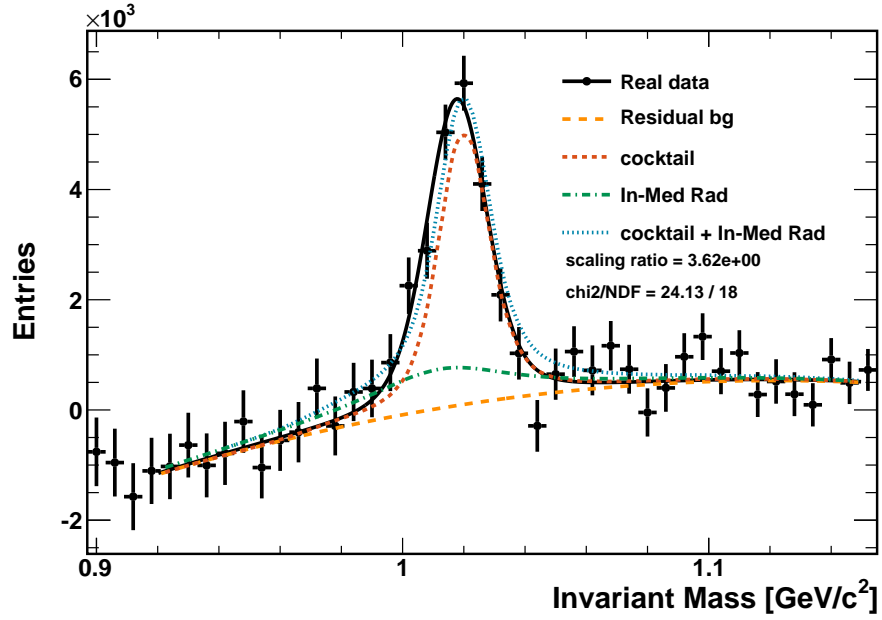


Figure 5.9: Schematic picture of the model calculation

effective chiral hadronic Lagrangian with coupling constants determined from the hadronic vacuum properties. This model includes an in-medium ϕ spectral function with expanding thermal fireball model [48], and subsequent improvements are applied [49]. There are two components. One is a “cocktail” contribution, which comes from the final state decays after the hadronic interaction stops (kinetic freeze-out). Most of the ϕ s decay in vacuum since the lifetime of ϕ (44 fm/c) is longer than the lifetime of hadronic medium (5 – 10 fm/c). Also, ϕ ’s decouple from the hadronic medium earlier ($T_{kin}^{\phi} \approx 160$ MeV) [50] than regular non-multi-strangeness hadrons do. The other component in the model is an “in-medium” contribution, which is from thermal (detailed balanced) dilepton radiation from the hadronic medium with medium modified ϕ spectral function. Due to the detailed balance of $\phi \leftrightarrow e^+e^-$ and/or K^+K^- , the number of ϕ s is constant at a given T. So, the number of decaying ϕ in medium is determined by the lifetime of the fireball and predicted by the model. The schematic picture of this model is presented in Figure 5.9.



(a) Fit with fixed ratio between the two components.



(b) Components fit with free ratio between the two components.

Figure 5.10: Components fit of the model calculation to the real $\phi \rightarrow e^+e^-$ data

To make a fair comparison the detector resolutions and inefficiencies have to be taken into account. We let ϕ decay into e^+e^- according to the invariant mass shapes and p_T spectra described by the blast wave model [51]. The parameters for the blast wave model are chosen as $T = 161$ MeV and $\beta_{surface}=0.65$ for the cocktail, and $T = 140$ MeV and $\beta_{surface}= 0.7$ for the in-medium radiation to match the theoretical model. The velocity profile is set so that $\beta_{avg} = 2/3 \beta_{surface}$. Then, all of the detector effects such as the detector resolutions, energy loss effect, and reconstruction inefficiencies, are applied on the daughters e^+e^- . Using the resulting invariant mass shapes, we perform a component fit to the real data. The fit results are shown in Figure 5.10. Since the ratio between the two components are part of the theoretical prediction, we fix the integrated yields ratio at 0.11 in the fit in Figure 5.10a, i.e. only the total amplitude is a free parameter. In Figure 5.10b, the ratio is also treated as a free parameter and a better χ^2 value is obtained with a 3.62 times larger in-medium contribution. There is the possibility to have more medium modification.

Chapter 6

Conclusion

The ϕ meson production from the e^+e^- channel in Au+Au collisions at $\sqrt{s_{NN}} = 200$ GeV is measured. This analysis requires a good electron and positron identification and it is only possible with the newly installed TOF detector at the STAR experiment. The p_T integrated ($p_T = 0.1 - 2.5$ GeV/ c) $\phi \rightarrow e^+e^-$ signal with significance of 15.93 is obtained in this analysis. From this invariant mass shape we set an upper limit of 15.3 MeV/ c^2 on the width and a lower limit of 1053.2 MeV/ c^2 on the mass with 95% confidence level. We also obtain the ϕ signals in seven p_T bins and measure the rapidity density of $dN/dy = 2.91 \pm 0.16(\text{stat.}) \pm 0.17(\text{sys.})$ and the mean transverse momentum of $\langle p_T \rangle = 1.03 \pm 0.06(\text{stat.}) \pm 0.06(\text{sys.})$ GeV/ c . The p_T spectrum is compared to the previously measured ϕ spectrum from the hadronic decay channel, $\phi \rightarrow K^+K^-$ [47]. Two results are consistent within 1σ in total yield and there is no indication of medium modification. The p_T integrated invariant signal is compared to the theoretical model which includes the hadronic medium effects. The contribution from the in-medium modification in the hadronic medium is small due to the long lifetime of ϕ meson. This indicates that the remaining small discrepancy between the measured and vacuum invariant mass shapes might be a sign of modification in the QGP, which is not included in the

current theoretical model.

Future Direction

This measurement can be improved by the higher statistics we have already taken in the year 2011. It is also interesting to study the system size effects by measuring ϕ signals in different centralities, in which the hadronic medium lifetime would be different. Since the model calculation shows the medium modified ϕ invariant mass shape with a large mass shift (≈ 50 MeV) and width broadening (≈ 35 MeV), yet small contribution, more dedicated study on the momentum resolution and detector effects are necessary to measure the signature of the chiral symmetry restoration.

Also, this analysis can be improved with the Muon Telescope Detector, which was recently assembled by the University of Texas at Austin group. With this detector subsystem, the di-muon channel is available and provides much cleaner signals and better momentum resolutions, which are both huge advantages in the chiral symmetry restoration search via resonance particles.

Appendices

Appendix A

Students' T Distribution

A.1 Physical meaning of Students' T Distribution

The Students' T distribution can be obtained via the convolution of a Gaussian distribution with a Gamma distribution, which describes the distribution of the resolution parameter in the Gaussian. This convolution is written as

$$\int_0^\infty A e^{-\frac{1}{2}\tau x^2} \frac{\tau^{k-1} e^{-\tau/\theta}}{\theta^k \Gamma(k)} d\tau = \frac{A}{\theta^k \Gamma(k)} \int_0^\infty \tau^{k-1} e^{-\left(\frac{x^2}{2} + \frac{1}{\theta}\right)\tau} d\tau, \quad \tau \equiv \frac{1}{\sigma^2}, \quad (\text{A.1})$$

where θ and k are the scale and shape parameters of the Gamma distribution, and τ and σ are resolution and standard deviation of the Gaussian distribution, respectively. With the definition $z \equiv \left(\frac{x^2}{2} + \frac{1}{\theta}\right)\tau$ and $d\tau = \left(\frac{x^2}{2} + \frac{1}{\theta}\right)^{-1} dz$,

$$\begin{aligned} (\text{Eq. A.1}) &= \frac{A}{\theta^k \Gamma(k)} \int_0^\infty \frac{z^{k-1}}{\left(\frac{x^2}{2} + \frac{1}{\theta}\right)^{k-1}} e^{-z} \left(\frac{x^2}{2} + \frac{1}{\theta}\right)^{-1} dz \\ &= \frac{A}{\theta^k \Gamma(k)} \left(\frac{x^2}{2} + \frac{1}{\theta}\right)^{-k} \underbrace{\int_0^\infty z^{k-1} e^{-z} dz}_{= \Gamma(k)} \\ &= A \left(\frac{x^2 \theta}{2} + 1\right)^{-k}, \end{aligned} \quad (\text{A.2})$$

where the wavy underline indicates an equivalence to the Gamma function $\Gamma(k)$. This is the Students' T distribution with $1/\theta = \frac{\nu}{2\lambda}$ and $k = \frac{\nu+1}{2}$. The ν and λ are the number of degrees of freedom and scale parameter, respectively. The mean of the Gamma distribution is $k\theta = \frac{\nu+1}{2} \frac{2\lambda}{\nu} = \lambda \frac{\nu+1}{\nu}$. The variance is $k\theta^2 = \frac{\nu+1}{2} \frac{(2\lambda)^2}{\nu} = 2\lambda^2 \frac{\nu+1}{\nu^2}$. The mean of the Students' T distribution is μ for $\nu > 1$ and its variance is $\frac{1}{\lambda} \frac{\nu}{\nu-2}$ for $\nu > 2$.

The Students' T distribution describes random variables sampled from many parent Gauss distributions with different resolutions, whose distribution is described by the Beta function. This is applicable to the TOF resolution in Au+Au collisions, in which the TOF start side detectors (upVPD) have many hits and the measured time have different resolution depending on the number of hits. To confirm this hypothesis, the Beta distribution from fits to real data has to be compared to the resolution distribution estimated from the number of lit upVPDs. This is left for future studies.

A.2 Integration of Students' T Distribution

The Students' T distribution is defined without a normalization factor as follow

$$\left(1 + \frac{\lambda(x - \mu)^2}{\nu}\right)^{-\frac{\nu+1}{2}}. \quad (\text{A.3})$$

Let us define $y \equiv \sqrt{\lambda}(x - \mu)$, $dy = \sqrt{\lambda}dx$. Then the integral is

$$\begin{aligned} \int_{-\infty}^{\infty} \left(1 + \frac{\lambda(x - \mu)^2}{\nu}\right)^{-\frac{\nu+1}{2}} dx &= \frac{1}{\sqrt{\lambda}} \int_{-\infty}^{\infty} \left(1 + \frac{y^2}{\nu}\right)^{-\frac{\nu+1}{2}} dy \\ &= \frac{2}{\sqrt{\lambda}} \int_0^{\infty} \left(1 + \frac{y^2}{\nu}\right)^{-\frac{\nu+1}{2}} dy. \end{aligned} \quad (\text{A.4})$$

In the last line the symmetry of the distribution in $\pm y$ is used. Again, let us define $t \equiv \frac{\nu}{\nu+y^2}$, then $y^2 = \nu(1/t - 1)$ and $2ydy = -\nu t^{-2}dt$. The integral range becomes $y = \infty \rightarrow t = 0$ and $y = 0 \rightarrow t = 1$.

$$\begin{aligned} (\text{Eq. A.4}) &= \frac{2}{\sqrt{\lambda}} \int_1^0 t^{\frac{\nu+1}{2}} \left(-\frac{1}{2} \sqrt{\frac{\nu t}{1-t}} t^{-2}\right) dt \\ &= \sqrt{\frac{\nu}{\lambda}} \int_0^1 t^{\frac{\nu-2}{2}} (1-t)^{-1/2} dt \\ &= \sqrt{\frac{\nu}{\lambda}} B\left(\frac{1}{2}, \frac{\nu}{2}\right) \end{aligned} \quad (\text{A.5})$$

$$\text{or} = \sqrt{\frac{\nu}{\lambda}} \frac{\Gamma(\frac{\nu}{2})\Gamma(\frac{1}{2})}{\Gamma(\frac{\nu+1}{2})} = \sqrt{\frac{\nu\pi}{\lambda}} \frac{\Gamma(\frac{\nu}{2})}{\Gamma(\frac{\nu+1}{2})}, \quad (\text{A.6})$$

where $B(\frac{1}{2}, \frac{\nu}{2})$ is the Beta function and $\Gamma(\frac{\nu}{2})$ is the Gamma function. Therefore its PDF (normalized to 1) should be

$$P(x; \mu, \lambda, \nu) = B\left(\frac{1}{2}, \frac{\nu}{2}\right)^{-1} \sqrt{\frac{\lambda}{\nu}} \left(1 + \frac{\lambda(x - \mu)^2}{\nu}\right)^{-\frac{\nu+1}{2}}. \quad (\text{A.7})$$

A.2.1 Integration from 0 to a

Let us start from Eq. A.4 but with the integral range from 0 to a and repeat the same replacements of variables, that is, $y = a \rightarrow t = \frac{\nu}{\nu+a^2}$ and

$y = 0 \rightarrow t = 1$.

$$\begin{aligned}
& \frac{2}{\sqrt{\lambda}} \int_0^a \left(1 + \frac{y^2}{\nu}\right)^{-\frac{\nu+1}{2}} dy \\
&= \sqrt{\frac{\nu}{\lambda}} \int_{\frac{\nu}{\nu+a^2}}^1 t^{\frac{\nu}{2}-1} (1-t)^{-1/2} dt \\
&= \sqrt{\frac{\nu}{\lambda}} \int_0^1 t^{\frac{\nu}{2}-1} (1-t)^{-1/2} dt - \sqrt{\frac{\nu}{\lambda}} \int_0^{\frac{\nu}{\nu+a^2}} t^{\frac{\nu}{2}-1} (1-t)^{-1/2} dt \\
&= \sqrt{\frac{\nu}{\lambda}} B\left(\frac{1}{2}, \frac{\nu}{2}\right) - \sqrt{\frac{\nu}{\lambda}} B\left(\frac{\nu}{\nu+a^2}; \frac{1}{2}, \frac{\nu}{2}\right), \tag{A.8}
\end{aligned}$$

where $B\left(\frac{\nu}{\nu+a^2}; \frac{1}{2}, \frac{\nu}{2}\right)$ is the incomplete Beta function. This is also written as

$$= \sqrt{\frac{\nu}{\lambda}} B\left(\frac{1}{2}, \frac{\nu}{2}\right) \left[1 - I\left(\frac{\nu}{\nu+a^2}; \frac{1}{2}, \frac{\nu}{2}\right)\right], \tag{A.9}$$

where $I\left(\frac{\nu}{\nu+a^2}; \frac{1}{2}, \frac{\nu}{2}\right)$ is the so called regularized Beta function. These functions are implemented in many statistical software and are very convenient when we calculate the efficiency or probability.

Integration from a to b

The integration of the PDF from a to b is

$$\begin{aligned}
& B\left(\frac{1}{2}, \frac{\nu}{2}\right)^{-1} \sqrt{\frac{\lambda}{\nu}} \int_a^b \left(1 + \frac{\lambda(x-\mu)^2}{\nu}\right)^{-\frac{\nu+1}{2}} dx \\
&= B\left(\frac{1}{2}, \frac{\nu}{2}\right)^{-1} \sqrt{\frac{\lambda}{\nu}} \frac{1}{\sqrt{\nu}} \int_{a'}^{b'} \left(1 + \frac{y^2}{\nu}\right)^{-\frac{\nu+1}{2}} dy, \tag{A.10}
\end{aligned}$$

where $a' \equiv \sqrt{\lambda}(a - \mu)$ and $b' \equiv \sqrt{\lambda}(b - \mu)$

$$\begin{aligned}
&= B\left(\frac{1}{2}, \frac{\nu}{2}\right)^{-1} \frac{1}{\sqrt{\nu}} \left[\int_{a'}^0 \left(1 + \frac{y^2}{\nu}\right)^{-\frac{\nu+1}{2}} dy + \int_0^{b'} \left(1 + \frac{y^2}{\nu}\right)^{-\frac{\nu+1}{2}} dy \right] \\
&= \frac{1}{2} \left(-\frac{a'}{|a'|}\right) \left[1 - I\left(\frac{\nu}{\nu + a'^2}; \frac{1}{2}, \frac{\nu}{2}\right)\right] \\
&\quad + \frac{1}{2} \left(\frac{b'}{|b'|}\right) \left[1 - I\left(\frac{\nu}{\nu + b'^2}; \frac{1}{2}, \frac{\nu}{2}\right)\right] \tag{A.11}
\end{aligned}$$

In order to reach the last line the previous result Eq. [A.9](#) is used.

Appendix B

TOF Resolution

B.1 Relation Between L_T and p_T

There is a relation between p_T and the radius of the helix curvature R

$$p_T = 0.3BR \quad (\text{B.1})$$

where B is the strength of a constant magnetic field. In STAR, $B \approx 0.5$ Tesla.

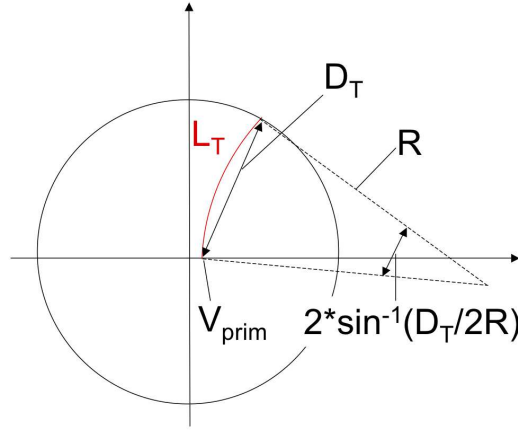


Figure B.1: Relation between p_T and L_T in the TPC

From Figure B.1 L_T can be written as a function of p_T ,

$$L_T = 2R \sin^{-1} \left(\frac{D_T}{2R} \right) = \frac{2p_T}{0.3B} \sin^{-1} \left(\frac{0.3BD_T}{2p_T} \right), \quad (\text{B.2})$$

where $D_T \simeq 214$ cm, $p_T = 0.3BR$, and $B \simeq 0.5$ Tesla]. The resolution of L_T depends on p_T as follows,

$$\frac{dL_T}{dp_T^{-1}} = \left[-(p_T^{-1})^{-2} A \sin^{-1} \frac{D_T}{Ap_T} + Ap_T \frac{D_T}{A} \frac{d}{d\left(\frac{D_T}{A} p_T^{-1}\right)} \left(\sin^{-1} \left(\frac{D_T}{A} p_T^{-1} \right) \right) \right] \quad (\text{B.3})$$

where $A \equiv \frac{2}{0.3B}$.

Now we need to define $\frac{d}{dX} (\sin^{-1} X)$. Let us define ρ as $\rho \equiv \sin^{-1} X$, so $X = \sin \rho$. Then,

$$\frac{dX}{d\rho} = \cos \rho \text{ and } \frac{d\rho}{dX} = \cos^{-1} \rho. \quad (\text{B.4})$$

Thus

$$\frac{d}{dX} (\sin^{-1} X) = \cos^{-1} \rho = \pm (1 - \sin^2 \rho)^{-\frac{1}{2}} = \pm (1 - X^2)^{-\frac{1}{2}}. \quad (\text{B.5})$$

In our case, $2\rho = 2 \sin^{-1} \left(\frac{D_T}{2R} \right)$. This is the angle shown in Figure B.1 and it can take values between 0 to π (above this value, we redefine ρ as an angle for opposite charged particle). So $\cos \rho$ is always positive. Therefore the Equation B.5 becomes

$$\frac{d}{dX} (\sin^{-1} X) = (1 - X^2)^{-\frac{1}{2}}. \quad (\text{B.6})$$

This result leads us

$$\frac{dL_T}{dp_T^{-1}} = -p_T L_T + p_T D_T \left[1 - \left(\frac{D_T}{A} p_T^{-1} \right)^2 \right]^{-\frac{1}{2}} \quad (\text{B.7})$$

or

$$\frac{\mathbf{p}_T^{-1}}{\mathbf{L}_T} \frac{d\mathbf{L}_T}{d\mathbf{p}_T^{-1}} = \frac{\mathbf{D}_T}{\mathbf{L}_T} \left[1 - \left(\frac{0.3\mathbf{B}\mathbf{D}_T}{2\mathbf{p}_T} \right)^2 \right]^{-\frac{1}{2}} - 1. \quad (\text{B.8})$$

B.2 Resolution of $\frac{\Delta\beta^{-1}}{\beta^{-1}}$

Let us calculate $\delta\left(\frac{\Delta\beta^{-1}}{\beta^{-1}}\right)$. The “ δ ” symbol indicates the standard deviation of a distribution of a variable considered. So $\delta\left(\frac{\Delta\beta^{-1}}{\beta^{-1}}\right)$ is standard deviation of the random variable $\frac{\Delta\beta^{-1}}{\beta^{-1}}$.

Recalling

$$\frac{\Delta\beta^{-1}}{\beta^{-1}} \equiv \frac{\beta_{TOF}^{-1} - \beta_{TPC}^{-1}}{\beta_{TOF}^{-1}} = 1 - \frac{L}{ct} \left(1 + \frac{m^2}{p^2} \right)^{\frac{1}{2}} \equiv X, \quad (\text{B.9})$$

we want to decompose the resolution of $\frac{\Delta\beta^{-1}}{\beta^{-1}}$, ie. $\delta\left(\frac{\Delta\beta^{-1}}{\beta^{-1}}\right)$, into several resolutions of measured variables, such as t , L , and p . For the time of flight t , it might be further decomposed into $t = T_{STOP} - T_{START}$, but, for now, only t is considered. The path length L of a track from a collision vertex to the TOF tray is calculated from the curvature of the track, which depends on p_T and the dip angle or η . Therefore, the resolution of L is correlated with resolution of p_T and η . The momentum resolution should be separated into two parts: p_T resolution and dip angle resolution (η resolution).

NOTE: The dip angle is defined as

$$\cos\theta \equiv \frac{p_z}{|p|} \quad (\text{B.10})$$

and relation with η is

$$\cos \theta \equiv \frac{pz}{|p|} = \frac{\sinh \eta}{\cosh \eta}. \quad (\text{B.11})$$

The resolution of $\frac{\Delta\beta^{-1}}{\beta^{-1}}$ is written below according to the error propagation rule with assumption that the errors of those variables are independent of each other,

$$\delta \left(\frac{\Delta\beta^{-1}}{\beta^{-1}} \right)^2 = \left(\frac{\partial X}{\partial t} \right)^2 (\delta t)^2 + \left(\frac{\partial X}{\partial p_T^{-1}} \right)^2 (\delta p_T^{-1})^2 + \left(\frac{\partial X}{\partial \cosh \eta} \right)^2 (\delta \cosh \eta)^2. \quad (\text{B.12})$$

Here p_T^{-1} is used instead of p_T because the resolution of transverse momentum scale with its inverse p_T^{-1} . The correct η dependency of the track length L is

$$L = \sqrt{L_T^2(p_T) + L_z^2} = \sqrt{L_T^2(p_T) + D_T^2 \sinh^2 \eta}, \quad (\text{B.13})$$

and L_z and D_T are related by

$$L_z = D_T \sinh \eta \text{ and } D = D_T \cosh \eta. \quad (\text{B.14})$$

The first derivatives of L are

$$\begin{aligned} \frac{\partial L}{\partial L_T} &= \frac{\partial}{\partial L_T} \sqrt{L_T^2 + L_z^2} = \frac{1}{2} 2L_T (L_T^2 + L_z^2)^{-\frac{1}{2}} \\ &= \frac{L_T}{L} \end{aligned} \quad (\text{B.15})$$

and

$$\begin{aligned} \frac{\partial L}{\partial \cosh \eta} &= \frac{D_T^2}{2L} \frac{\partial \sinh^2 \eta}{\partial \cosh \eta} = \frac{D_T^2}{2L} \frac{\partial (\cosh^2 \eta - 1)}{\partial \cosh \eta} \\ &= \frac{D_T^2}{L} \cosh \eta. \end{aligned} \quad (\text{B.16})$$

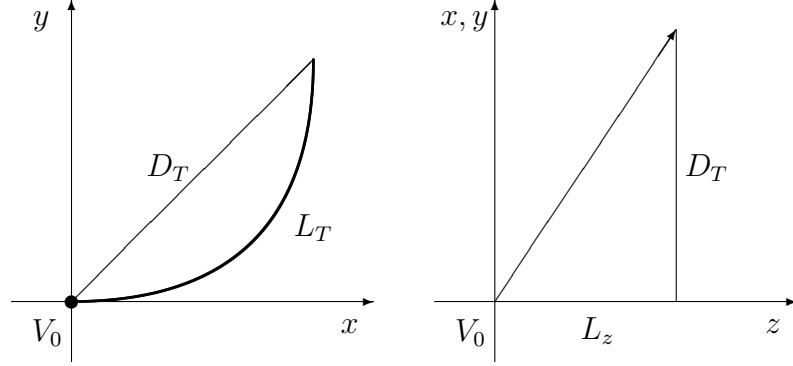


Figure B.2: Relation between D_T and track length

Each term in Equation B.12 is calculated next.

$$\begin{aligned}
\frac{\partial X}{\partial p_T^{-1}} &= \frac{-1}{ct} \sqrt{1 + \frac{m^2}{p^2} \frac{\partial L}{\partial L_T} \frac{\partial L_T}{\partial p_T^{-1}}} - \frac{L}{ct} \frac{\partial (1 + m^2 p_T^{-2} \cosh^{-2} \eta)^{\frac{1}{2}}}{\partial p_T^{-1}} \\
&= \frac{-L}{ct} \sqrt{1 + \frac{m^2}{p^2} \frac{L_T}{L^2} \frac{\partial L_T}{\partial p_T^{-1}}} - \frac{L}{ct} \frac{1}{2} \frac{2 p_T^{-1} m^2 \cosh^{-2} \eta}{\sqrt{1 + m^2 p^{-2}}} \\
&= (X - 1) \frac{L_T^2}{L^2} \frac{p_T^{-1}}{L_T} \frac{\partial L_T}{\partial p_T^{-1}} p_T + (X - 1) \frac{m^2 p^{-2}}{1 + m^2 p^{-2}} p_T \\
&= (X - 1) \frac{1}{p_T^{-1}} \left[\frac{L_T^2}{L^2} \frac{p_T^{-1}}{L_T} \frac{\partial L_T}{\partial p_T^{-1}} + \gamma_{TPC}^{-2} \right]. \tag{B.17}
\end{aligned}$$

Using eq. B.16

$$\begin{aligned}
\frac{\partial X}{\partial \cosh \eta} &= \frac{-1}{ct} \sqrt{1 + \frac{m^2}{p^2} \frac{\partial L}{\partial \cosh \eta}} - \frac{L}{ct} \frac{\partial (1 + m^2 p_T^{-2} \cosh^{-2} \eta)^{\frac{1}{2}}}{\partial \cosh \eta} \\
&= (X - 1) \frac{D^2}{L^2} \cosh^{-1} \eta - \frac{L}{ct} \frac{1}{2} \frac{-2 m^2 p_T^{-2} \cosh^{-3} \eta}{\sqrt{1 + m^2 p^{-2}}} \\
&= (X - 1) \frac{D^2}{L^2} \cosh^{-1} \eta - (X - 1) \frac{m^2 p^{-2}}{1 + m^2 p^{-2}} \cosh^{-1} \eta \\
&= (X - 1) \frac{1}{\cosh \eta} \left[\frac{D^2}{L^2} - \gamma_{TPC}^{-2} \right]. \tag{B.18}
\end{aligned}$$

Lastly,

$$\frac{\partial X}{\partial t} = \frac{L}{ct^2} \sqrt{1 + \frac{m^2}{p^2}} = -(X - 1) \frac{1}{t}. \quad (\text{B.19})$$

From eqs. B.8, B.17, B.18, and B.19, the total resolution is

$$\begin{aligned} \delta \left(\frac{\Delta \beta^{-1}}{\beta^{-1}} \right)^2 &= \left(\frac{\delta t}{t} \right)^2 \\ &+ \left(\frac{L_T^2}{L^2} \left\{ \frac{D_T}{L_T} \left[1 - \left(\frac{0.3 B D_T}{2 p_T} \right)^2 \right]^{-\frac{1}{2}} - 1 \right\} + \gamma_{TPC}^{-2} \right)^2 \left(\frac{\delta p_T^{-1}}{p_T^{-1}} \right)^2 \\ &+ \left(\frac{D^2}{L^2} - \gamma_{TPC}^{-2} \right)^2 \left(\frac{\delta \cosh \eta}{\cosh \eta} \right)^2. \end{aligned} \quad (\text{B.20})$$

In the Equation B.19 X is set to 0. This is true for the particle distribution of the mass assumption, but not true for other particle distributions. For example, for pion we assume pion mass to fill the $\frac{\Delta \beta^{-1}}{\beta^{-1}}$ histogram. The resolution of pion distribution (band) can be described by B.20, however, for kaon or proton distribution, we need to include the $(X - 1)$ factor in Equation B.19.

Appendix C

Spontaneous Symmetry Breaking

C.1 Spontaneous Symmetry Breaking

Spontaneous symmetry breaking describes the situation in which the Hamiltonian remains its symmetry, however the ground states don not. If the symmetry is a continuous symmetry, the ground states are infinitely degenerated and condensation occurs. This is due to the fact that one ground state transforms to another ground state that has the same energy due to the symmetry in the Hamiltonian. In order to see this, suppose the Hamiltonian H of a system is invariant under a unitary transformation operator U , and $|\Psi_0\rangle$ is a ground state with corresponding ground state energy E_0 . Hence,

$$H|\Psi_0\rangle = E_0|\Psi_0\rangle. \quad (\text{C.1})$$

The invariance of H under U operation can be written as

$$U^\dagger H U = H. \quad (\text{C.2})$$

Substituting this equation into Equation C.1 and acting another U operator yields

$$H(U|\Psi_0\rangle) = E_0(U|\Psi_0\rangle). \quad (\text{C.3})$$

This shows us that if $U|\Psi_0\rangle$ is distinct from $|\Psi_0\rangle$ due to symmetry breaking in the ground state, then the ground state of a system is degenerate. Generalizing to the case of continuous symmetries implies that the ground state must be infinitely degenerate.

Bibliography

- ¹E. Kolb and M. Turner, *The early universe* (Addison-Wesley, Redwood City, 1990) (cit. on p. 1).
- ²D. J. Gross and F. Wilczek, “Ultraviolet behavior of non-abelian gauge theories”, *Phys. Rev. Lett.* **30**, 1343–1346 (1973) (cit. on pp. 1, 3).
- ³H. D. Politzer, “Reliable perturbative results for strong interactions?”, *Phys. Rev. Lett.* **30**, 1346–1349 (1973) (cit. on pp. 1, 3).
- ⁴B. V. Jacak and B. Müller, “The exploration of hot nuclear matter”, *Science* **337**, 310 (2012) (cit. on p. 1).
- ⁵J. Adams et al., (STAR Collaboration), “Experimental and theoretical challenges in the search for the quark–gluon plasma: The STAR Collaboration’s critical assessment of the evidence from RHIC collisions”, *Nucl. Phys. A* **757**, 102 (2005) (cit. on p. 1).
- ⁶USA-NSAC, “Hot and Dense QCD Matter”, *Long Range Plans*, 2012 (cit. on p. 2).
- ⁷V. Koch, “Introduction to chiral symmetry”, arXiv:nucl-th/9512029, 1995 (cit. on p. 3).
- ⁸J. PresKill, “Introduction to chiral symmetry”, *Lecture note* (cit. on p. 3).
- ⁹J. D. Bjorken, “Asymptotic sum rules at infinite momentum”, *Phys. Rev.* **179**, 1547–1553 (1969) (cit. on p. 3).
- ¹⁰J. Beringer et al., “Review of particle physics”, *Phys. Rev. D* **86**, 010001 (2012) (cit. on pp. 4, 45).
- ¹¹R. Barate et al., “Measurement of the axial-vector τ spectral functions and determination of $\alpha_s(M_\tau^2)$ from hadronic τ decays”, *Eur. Phys. J. C* **4**, 409–431 (1998) (cit. on p. 9).

- ¹²Y. Nambu and G. Jona-Lasinio, “Dynamical model of elementary particles based on an analogy with superconductivity”, *Phys. Rev.* **122** (1961) (cit. on p. 9).
- ¹³J. Bardeen, L. N. Cooper, and J. R. Schrieffer, “Microscopic theory of superconductivity”, *Phys. Rev.* **106**, 162–164 (1957) (cit. on p. 10).
- ¹⁴J. Bardeen, L. N. Cooper, and J. R. Schrieffer, “Theory of superconductivity”, *Phys. Rev.* **108**, 1175–1204 (1957) (cit. on p. 10).
- ¹⁵L. N. Cooper, “Bound electron pairs in a degenerate fermi gas”, *Phys. Rev.* **104**, 1189–1190 (1956) (cit. on p. 10).
- ¹⁶N. Bilić and H. Nikolic, “Chiral-symmetry restoration in the linear sigma model at nonzero temperature and baryon density”, *Eur. Phys. J. C* **6**, 515–523 (1999) (cit. on p. 12).
- ¹⁷M. Peskin and D. Schroeder, *An introduction to quantum field theory* (Westview Press, 1995) (cit. on p. 14).
- ¹⁸G. E. Brown and M. Rho, “Scaling effective lagrangians in a dense medium”, *Phys. Rev. Lett.* **66**, 2720–2723 (1991) (cit. on p. 14).
- ¹⁹R. Rapp, J. Wambach, and H. van Hees, *The chiral restoration transition of qcd and low mass dileptons*, edited by R. Stock, Vol. 23 (Springer-Verlag Berlin Heidelberg, 2010) (cit. on p. 14).
- ²⁰C. Markert, “Strange hadron resonances: freeze-out probes in heavy-ion collisions”, *AIP Conf. Proc.* **631**, 533–552 (2002) (cit. on p. 16).
- ²¹K. Nakamura et al., (Particle Data Group), “Review of particle physics”, *J. Phys. G* **37**, 075021 (2010) (cit. on pp. 17, 120).
- ²²M. Harrison, T. Ludlam, and S. Ozaki, “RHIC project overview”, *Nucl. Instr. and Meth. A* **499**, 235–244 (2003) (cit. on pp. 20, 21).
- ²³T. Ludlam, “Overview of experiments and detectors at RHIC”, *Nucl. Instr. and Meth. A* **499**, 428–432 (2003) (cit. on p. 20).
- ²⁴K. H. Ackermann et al., (STAR Collaboration), “Star detector overview”, *Nucl. Instr. and Meth. A* **499**, 624–632 (2003) (cit. on p. 23).

- ²⁵M. Anderson et al., “The STAR time projection chamber”, *Nucl. Instr. and Meth. A* **499**, 659–678 (2003) (cit. on p. 24).
- ²⁶W. R. Leo, *Techniques for nuclear and particle physics experiments* (Springer-Verlag, 1994) (cit. on p. 26).
- ²⁷W.-M. Yao et al., (Particle Data Group), “Review of Particle Physics”, *J. Phys. G: Nucl. Part. Phys.* **33**, 1 (2006) (cit. on p. 27).
- ²⁸G. Van Buren et al., “Correcting for distortions due to ionization in the STAR TPC”, *Nucl. Instr. and Meth. A* **566**, 22–25 (2006) (cit. on p. 30).
- ²⁹J. Abele et al., (STAR Collaboration), “The laser system for the STAR time projection chamber”, *Nucl. Instr. and Meth. A* **499**, 692–702 (2003) (cit. on p. 30).
- ³⁰E. C. Zeballos et al., “A new type of resistive plate chamber: The multigap RPC”, *Nucl. Instr. and Meth. A* **374**, 132–135 (1996) (cit. on p. 30).
- ³¹W. Llope, “The large-area time-of-flight upgrade for STAR”, *Nucl. Instr. and Meth. B* **241**, 306–310 (2005) (cit. on p. 31).
- ³²K. Kajimoto, “A large area time of flight detector for the star experiment at rhic”, Ph.D. Dissertation (The Physics Department at the University of Texas at Austin, 2009) (cit. on p. 33).
- ³³P. Fachini et al., “Proposal for a large area time of flight system for star”, [Link](#), 2004 (cit. on p. 33).
- ³⁴E. Cerron Zeballos et al., “A comparison of the wide gap and narrow gap resistive plate chamber”, *Nucl. Instr. and Meth. A* **373**, 35–42 (1996) (cit. on p. 36).
- ³⁵E. C. Zeballos et al., “High rate resistive plate chambers”, *Nucl. Instr. and Meth. A* **367**, 388–393 (1995) (cit. on p. 36).
- ³⁶I. Crotty et al., “The wide gap resistive plate chamber”, *Nucl. Instr. and Meth. A* **360**, 512 (1995) (cit. on p. 36).

- ³⁷M. Shao et al., “Upgrade of the calibration procedure for a star time-of-flight detector with new electronics”, *Meas. Sci. Technol.* **20**, 025102 (2009) (cit. on p. 37).
- ³⁸C. Adler et al., “The RHIC zero-degree calorimeters”, *Nucl. Instr. and Meth. A* **499**, 433–436 (2003) (cit. on p. 40).
- ³⁹C. Lippmann, “Particle identification”, *Nucl. Instr. and Meth. A* **666**, 148–172 (2012) (cit. on p. 44).
- ⁴⁰H. Bichsel, “A method to improve tracking and particle identification in TPCs and silicon detectors”, *Nucl. Instr. and Meth. A* **562**, 154–197 (2006) (cit. on p. 53).
- ⁴¹M. Shao et al., “Extensive particle identification with TPC and TOF at the STAR experiment”, *Nucl. Instr. and Meth. A* **558**, 419–429 (2006) (cit. on p. 64).
- ⁴²M. L. Miller et al., “Glauber modeling in high-energy nuclear collisions”, *Ann. Rev. Nucl. Part. Sci.* **57**, 205–243 (2007) (cit. on p. 78).
- ⁴³J. Adams et al., (STAR Collaboration), “ ρ_0 Production and Possible Modification in Au+Au and p+p Collisions at $\sqrt{s_{NN}} = 200$ GeV”, *Phys. Rev. Lett.* **92**, 092301 (2004) (cit. on p. 96).
- ⁴⁴J. Adams et al., (STAR Collaboration), “K(892)* resonance production in Au+ Au and p+ p collisions at $\sqrt{s_{NN}} = 200$ GeV”, *Phys. Rev. C* **71**, 064902 (2005) (cit. on p. 96).
- ⁴⁵R. Snellings, “Elliptic flow: a brief review”, *New J. Phys.* **13**, 055008 (2011) (cit. on p. 97).
- ⁴⁶T. Ullrich and Z. Xu, “Treatment of Errors in Efficiency Calculations”, arXiv: physics/0701199, 2007 (cit. on p. 107).
- ⁴⁷B. I. Abelev et al., (STAR Collaboration), “Measurements of ϕ meson production in relativistic heavy-ion collisions at the BNL Relativistic Heavy Ion Collider (RHIC)”, *Phys. Rev. C* **79**, 22 (2009) (cit. on pp. 113, 123, 128).

- ⁴⁸R. Rapp, “Signatures of thermal dilepton radiation at ultrarelativistic energies”, Phys. Rev. C **63**, 054907 (2001) (cit. on p. 125).
- ⁴⁹H. van Hees and R. Rapp, “Dilepton radiation at the CERN super-proton synchrotron”, Nucl. Phys. A **806**, 339 (2008) (cit. on p. 125).
- ⁵⁰M. He, R. J. Fries, and R. Rapp, “Ideal hydrodynamics for bulk and multistrange hadrons in $\sqrt{s_{NN}} = 200$ GeV Au-Au collisions”, Phys. Rev. C **85**, 044911 (2012) (cit. on p. 125).
- ⁵¹E. Schnedermann, J. Sollfrank, and U. Heinz, “Thermal phenomenology of hadrons from 200A GeV S+S collisions”, Phys. Rev. C **48**, 2462 (1993) (cit. on p. 127).

Vita

Masayuki Wada was born in Neyagawashi, Osaka, Japan on 24 June 1982, the son of Osamu Yamaguchi and Michiko Yamaguchi. He began to take an interest in science when he was in an elementary school because a girl he liked at the time liked stars and the universe. He received the Bachelor of Science degree in Physics from the Tokyo University of Science in 2005. In September 2006, he entered the Graduate School at The University of Texas at Austin. From 2007-2013 he worked as a graduate research assistant in high-energy nuclear experimental physics. He was a member of the STAR collaboration from 2007-2013. He mainly contributed to the maintenance and operation of the TOF detector subsystem and the development of particle identification methods using the TOF detector.

Permanent address: 43-47-19 Fuchimachi
Fukuishi, Fukui Japan 918-8026

This dissertation was typeset with L^AT_EX by the author.